

**ASSESSING FRACTURE NETWORK CONNECTIVITY OF PREFEASIBILITY-LEVEL
HIGH TEMPERATURE GEOTHERMAL PROJECTS USING DISCRETE FRACTURE
NETWORK MODELLING**

by

Stephen W. Mak

B.A.Sc., The University of British Columbia, 2008

A THESIS SUBMITTED IN PARTIAL FULFILLMENT OF
THE REQUIREMENTS FOR THE DEGREE OF

MASTER OF APPLIED SCIENCE

in

THE FACULTY OF GRADUATE AND POSTDOCTORAL STUDIES
(Geological Engineering)

THE UNIVERSITY OF BRITISH COLUMBIA
(Vancouver)

October 2014

© Stephen W. Mak, 2014

Abstract

The Meager Creek geothermal anomaly has been identified as one of Canada's most promising high temperature geothermal sites. Results from exploratory drilling and the presence of natural hot springs indicate that a convective hydrothermal system exists within the crystalline basement rocks at the site. These positive results prompted several companies to engage in production drilling campaigns as early as 1981. To date, all attempts to establish sustainable levels of geothermal fluid production have been unsuccessful. Low permeability and poor hydraulic connectivity of the basement granodiorites are often cited as the key geological factors limiting the development of the Meager Creek site. These conclusions are inferred from qualitative assessments of core samples and the low production yields of completed test wells, and are not based on a detailed analysis of the geometric properties of the underlying fracture network.

Through the interpretation and analysis of geomechanical and hydrogeological data collected during historical field investigations at the site, stochastic discrete fracture network (DFN) models were constructed. An iterative process of simulation and analysis of individual DFN models led to a rigorous assessment of the existing connectivity of the natural fracture network. The connectivity of the existing fracture network at the Meager Creek site appears to be favourable in the area surrounding the Meager Creek Fault, which was not intersected by any of the test wells drilled.

It was found that the use of DFN models was useful in estimating fracture network connectivity and can serve as a tool for optimizing the location and orientation of

production wells. A high degree of uncertainty is associated with fracture network connectivity estimates due to the absence of downhole linear fracture intensity measurements and a rigorous surface mapping methodology. Fracture network connectivity estimates can be greatly improved by adjusting the design of prefeasibility-level field investigations. The additional cost and time required to incorporate these adjustments into standard prefeasibility-level geothermal field investigations is minimal.

Preface

This thesis is original, unpublished work by the author, Stephen Mak

Table of Contents

Abstract	ii
Preface	iv
Table of Contents	v
List of Tables	xi
List of Figures	xiii
List of Acronyms/Abbreviations	xvi
Acknowledgements	xvii
Dedication	xviii
Chapter 1: INTRODUCTION	1
1.1 Problem Statement	1
1.2 Research Objectives	4
1.3 Thesis Organization	6
1.4 Use and Limitations.....	7
Chapter 2: LITERATURE REVIEW	8
2.1 The Role of Fractures in High Temperature Geothermal Systems.....	10
2.1.1 Types of Geothermal Systems	10
2.1.1.1 Conventional/Hydrothermal systems.....	10
2.1.1.2 Enhanced Geothermal Systems (EGS).....	12
2.1.1.3 Cost of Conventional Versus EGS Wells	13
2.1.2 Temperature Ranges of Geothermal Resources	15
2.1.3 Heat Transfer in Geothermal Systems.....	16

2.1.4	Fractured Volume in Relation to Production Potential	17
2.2	Fracture Network Characterization.....	18
2.2.1	Geometric Characteristics of Individual Fractures	18
2.2.1.1	Shape.....	19
2.2.1.2	Trace Length and Fracture Size.....	20
2.2.1.3	Planarity	24
2.2.1.4	Aperture	25
2.2.1.5	Orientation	26
2.2.2	Fracture Network Properties.....	27
2.2.2.1	Location of Individual Fractures	27
2.2.2.2	Spacing.....	28
2.2.2.3	Intensity, P10 and P32.....	29
2.2.3	Influence of Connected Fracture Networks on Recoverable Heat.....	31
2.3	Discrete Fracture Network Modelling of Geothermal Systems.....	33
2.3.1	Conceptual Model of a Crystalline Rock Mass	33
2.3.2	The Discrete Fracture Network Modelling Software FracMan	35
2.3.2.1	Fracture Generation Using FracMan.....	35
2.3.2.2	Generation of DFN Models Using Monte Carlo Simulation	37
Chapter 3:	SITE DESCRIPTION	38
3.1	Regional Geology.....	38
3.2	Site Geology.....	39
3.3	Structural Geology	40
3.4	Regional Groundwater Flow.....	41

3.5	Observed Temperature Profiles	42
3.6	Overview of Historical Field Investigations.....	43
3.6.1	Detailed Summary of Bedrock Drilling between 1974 and 1982.....	46
3.6.2	Summary of Structural Mapping Programs.....	51
3.6.2.1	1980 Structural Mapping Program	52
3.6.2.2	1981 Structural Mapping Program	54
3.6.2.3	2013 Structural Mapping Program	55
Chapter 4: INTERPRETATION OF FRACTURE DATA.....		56
4.1	Data Collected from Bedrock Drilling	56
4.1.1	Lithology and Alteration Logs	57
4.1.2	Core Recovery.....	59
4.1.3	Rock Quality Designation	59
4.1.4	Fracture Frequency	61
4.1.5	Drilling Conditions Logs.....	66
4.1.6	Volcanic Dykes	68
4.2	Fracture Data Collected from Surface Mapping	68
4.2.1	Delineation of Structural Domains	69
4.2.2	Peak Orientation and Distribution Parameters for Major Fracture Sets	73
4.2.3	Analysis of Fracture Spacing	76
4.2.4	Fracture Trace Length	79
Chapter 5: DFN MODEL DEVELOPMENT AND ANALYSIS RESULTS.....		83
5.1	Methodology Used for DFN Model Simulation and Connectivity Analyses	83
5.1.1	Population of DFN Models Using Individual Fracture Sets	84

5.1.2	Number of Unique DFN Simulations.....	85
5.1.3	Exclusion of Randomly Oriented Fractures	87
5.1.4	Cluster Analysis.....	87
5.1.5	Well Connectivity Analysis.....	88
5.1.6	Transmissible Fracture Rating.....	91
5.2	Uniform Rock Mass Model	93
5.2.1	Model Boundaries and P32 Values for Individual Fracture Sets.....	94
5.2.2	Cluster Analysis Results	96
5.2.2.1	Effect of Global P32 Fracture Intensity on Cluster Size	98
5.2.2.2	Effect of TFR Filters on Cluster Size	99
5.2.3	Well Connectivity Analysis Results	102
5.2.3.1	P10 as a Function of Well Location.....	102
5.2.3.2	P10 of Connected Fractures in Vertical Wells	104
5.2.3.3	P10 of Connected Fractures in Inclined Wells	106
5.2.3.4	Comparison of Simulated and Observed P10 and RQD	109
5.3	Meager Creek Fault Model.....	111
5.3.1	Model Boundaries and P32 Values for Individual Fracture Sets.....	112
5.3.2	Cluster Analysis Results	114
5.3.2.1	Size and Distribution of Self-Connected Clusters	116
5.3.2.2	Lost Circulation Zones and Elevation of Meager Creek Fault	120
5.3.3	Well Connectivity Analysis Results	122
5.3.3.1	P10 of Connected Fractures in Vertical Wells.....	123
5.3.3.2	P10 of Connected Fractures in Inclined Well	126

5.4	Estimation of Recovery Factors	131
Chapter 6: CONCLUSION		135
6.1	Interpretation of Fracture Data	136
6.1.1	Key Findings from the Interpretation of Available Fracture Data	136
6.1.2	Limitation of the Data Collection Program	137
6.2	DFN Simulation Results - Uniform Rock Mass Model	138
6.2.1	Cluster Analysis.....	138
6.2.2	Well Connectivity Analysis.....	139
6.3	DFN Simulation Results - Meager Creek Fault Model.....	140
6.3.1	Cluster Analysis.....	140
6.3.2	Well Connectivity Analysis.....	141
6.4	Assumptions and Limitations of the DFN Simulation Results.....	143
6.5	Recommendations for Improving Fracture Network Connectivity Estimates..	143
6.5.1	Hydrogeological Field Data.....	144
6.5.2	Structural Mapping	145
6.5.3	Geotechnical Drilling.....	147
6.6	Recommendations for Future Work	149
REFERENCES.....		151
APPENDICES.....		157
Appendix A : Maps.....		158
Appendix B : Geomechanical Logs.....		161
Appendix C : Stereographic Plots of Surface Mapping Data		177
Appendix D : Coordinates of Mapping Stations		189

D.1	Mapping station coordinates, 1980 surface mapping campaign	190
D.2	Mapping station coordinates, 1981 surface mapping campaign	191
D.3	Mapping station coordinates, 1980 surface mapping campaign	194

List of Tables

Table 2.1	Definition of common fracture types	9
Table 2.2	Pxy fracture intensity notation and the relationship between the dimensionality of the rock mass sample and measurement dimension.	30
Table 3.1	Average orientations of large scale structures in the South Reservoir	41
Table 3.2	Summary of collar information for all slim holes and wells drilled between 1974 and 1982.....	49
Table 4.1	Rock types encountered during the 1974 - 1982 slim hole drilling program .	58
Table 4.2	Qualitative and quantitative descriptions of fracture frequency	62
Table 4.3	Summary of peak orientations for major fracture sets based on surface mapping data from the North Reservoir, South Reservoir, and East of Camp Fault structural domains.....	75
Table 4.4	Summary of distribution parameters for trace length data	80
Table 5.1	Collar survey of wells used in well connectivity analyses	89
Table 5.2	UTM coordinates of DFN model boundaries	94
Table 5.3	Weighted P32 values for fracture sets in the Uniform Rock Mass model	96
Table 5.4	Summary of cluster analysis statistics from DFN simulations of the South Reservoir based on the Uniform Rock Mass Model.....	97
Table 5.5	Comparison of connected cluster size assuming different fracture size distributions at the TFR cut-off limit	101

Table 5.6 Comparison of P10 values in slim holes M09-80D and M10-80D from DFN simulations using the Uniform Rock Model and P10 values derived from depth-averaged RQD.....	109
Table 5.7 Weighted P32 values for individual fracture sets in the Meager Creek Fault model.....	114
Table 5.8 Comparison of cluster analysis statistics from DFN simulations of the South Reservoir based on the Meager Creek Fault model	115
Table 5.9 Location and orientation of inclined wells used in well connectivity analyses for the Meager Creek Fault model	126
Table 5.10 Probability of intersecting connected fracture networks and average P10 for both vertical and inclined wells	130
Table 5.11 Assumed values for recovery factor calculations.....	132
Table 5.12 Recovery factors based on calculated fractured rock volumes.....	134

List of Figures

Figure 2.1	The role of the water cycle in sustaining geothermal systems	11
Figure 2.2	Schematic of a two-well EGS system.....	13
Figure 2.3	Cost comparison of conventional and EGS geothermal wells.....	14
Figure 2.4	Example of a non-planar fracture surface indicating the scales of roughness and waviness.....	24
Figure 2.5	A two-dimensional representation of a discontinuous rock mass	34
Figure 4.1	Depth-averaged RQD versus elevation at the Meager Creek site.....	60
Figure 4.2	Fracture frequency calculated from depth-averaged RQD versus elevation at the Meager Creek site	64
Figure 4.3	Sensitivity of $TRQD_t$ to a range of $TRQD_t$ threshold values	65
Figure 4.4	Structural domains identified within the South Reservoir	72
Figure 4.5	Combined lower hemisphere equal area stereonet plot of all fracture data collected from surface outcrops of Quartz Diorite in the North Reservoir, South Reservoir, and East of Camp Fault structural domains	76
Figure 4.6	Combined histogram of true fracture spacing measurements collected from surface mapping of Quartz Diorite outcrops located in the North and South Reservoir structural domains.....	78
Figure 4.7	Distribution of trace length measurements for all fractures	81
Figure 5.1	Cumulative standard deviation and cumulative average of simulated connected fracture network P32 versus the number of DFN model	

simulations for various combinations of fracture spacing and fracture size distributions.	86
Figure 5.2 Location of vertical sampling wells 1 - 16.....	90
Figure 5.3 Orientation and location of inclined sampling wells	91
Figure 5.4 Using the Transmissible Fracture Rating (TFR) to assess cluster network connectivity.....	93
Figure 5.5 Model boundaries of the Uniform Rock Mass model, facing northeast.	95
Figure 5.6 Effects of TFR filter criteria on the size and extent of connected fracture clusters	99
Figure 5.7 Contour lines based on the average number of fractures intersected by vertical wells for DFN simulations with a global $P32 = 0.5 \text{ m}^{-1}$. Slim holes M09-80D and M10-80D are plotted for reference only, and were not used to generate the contours.....	103
Figure 5.8 Average P10 values in vertical sampling wells as the TFR cut-off limit is approached	105
Figure 5.9 Average P10 values for inclined sampling wells as the TFR cut-off limit is approached	108
Figure 5.10 Conceptual model of the Meager Creek Fault permeable damage zone and impermeable core.....	112
Figure 5.11 Model space for the bottom region of the Meager Creek Fault model. The green plane is the projected location of the Meager Creek Fault. Simulated fractures are limited to the hanging wall and fault damage zone regions of the model.	113

Figure 5.12 Comparison of connected cluster size as a function of TFR filter criteria for DFN simulations following the Meager Creek Fault and Uniform Rock mass models for a global $P_{32} = 0.5 \text{ m}^{-1}$	117
Figure 5.13 Development of three concentrated fracture networks surrounding the fault damage zone as the percentage of transmissive fractures approaches the TFR cut-off limit.....	119
Figure 5.14 Cross-section of the South Reservoir, facing east.	121
Figure 5.15 Number of observed and connected fractures intersected by vertical sampling wells as a function of depth at various TFR filters.....	125
Figure 5.16 Location and relative spacing of inclined wells oriented parallel to the Meager Creek Fault plane.....	127
Figure 5.17 Average P10 of inclined wells as a function of distance from the hanging wall-damage zone contact margin and TFR filter	128

List of Acronyms/Abbreviations

DFN – Discrete Fracture Network

ISRM – International Society for Rock Mechanics

MMVC – Meager Mountain Volcanic Complex

NSBG – Nevin, Sadler-Brown, Goodbrand Ltd.

P10 – Linear Fracture Intensity (# fractures/m)

P32 – Volumetric Fracture Intensity (m^2/m^3)

TFR – Transmissive Fracture Rating

Acknowledgements

I would like to thank my supervisors Dr. Erik Eberhardt and Dr. John Meech for their patience, mentorship, and guidance. I would also like to thank my advisory committee members Dr. Mory Ghomshei and Dr. Kelly Russell. A special thanks is extended to Dr. Catherine Hickson and Dr. Nathalie Vigouroux, who were instrumental during the data collection process. Last but not least, I would like to thank my family, friends, and colleagues. Their unconditional support and encouragement throughout this process was very much appreciated and will never be forgotten.

Funding for this research was provided by the Natural Sciences and Engineering Research Council of Canada, the Pacific Institute for Climate Solutions, Geoscience BC, and the Department of Earth, Ocean and Atmospheric Sciences at UBC.

For Mika and Greysen,

The members of my family that make me smile when I come home at night

CHAPTER 1: INTRODUCTION

Geothermal energy represents a clean, renewable, base-load source of energy that is underutilized in Canada. Currently the status of geothermal energy usage in Canada is limited to heating/cooling systems for residential and commercial infrastructure through the use of low temperature heat exchangers. Despite having a wide distribution of potential high temperature geothermal sites, currently there is no commercial electricity production derived from geothermal energy in Canada. The amount of energy stored within Canada's in-place geothermal resources is estimated to be greater than one million times current electrical consumption, although only a fraction of this energy can be accessed. The location of high temperature geothermal sites that have the greatest potential of being developed are concentrated in the western provinces of British Columbia and Alberta, and the Yukon and Northwest Territories (Grasby et al. 2011).

1.1 Problem Statement

The area surrounding Meager Mountain, approximately 150 km north of Vancouver, British Columbia, has been characterized as the most promising high temperature geothermal site in Canada (Jessop, Ghomshei, and Drury 1991), with an estimated net electrical capacity of 250 MW (Ghomshei et al. 2004). In spite of this designation and the long history of private and government-sponsored geothermal exploration in the area, all attempts to generate electricity from the site have been unsuccessful. As such, it is worthwhile to investigate the factors that have prevented the successful development of what was once considered one of Canada's most promising renewable energy resources.

Similar to other geothermal projects, the unsuccessful development of the Meager Creek site has been attributed to:

1. Questionable connectivity of fractures in low-permeability reservoir rocks;
2. Geological uncertainty associated with the characterization of the resource; and
3. The cost of exploration required for design-level reservoir characterization.

The most important geological factor affecting the viability of geothermal projects is the connectivity of the existing fracture network within the reservoir rocks. The amount of heat that can be extracted from a geothermal resource is dependent on the rate at which high temperature fluids (typically water and steam) can be produced from geothermal wells. The rate of fluid extraction is largely controlled by the geological properties of the reservoir rocks that host the geothermal resource. If a geothermal resource is hosted in low-permeability rocks, the circulation of fluids throughout the reservoir rocks will be largely confined to networks of interconnected fractures. It follows that the volume and rate at which fluids can be circulated through a geothermal reservoir are a function of the properties of these fracture networks which include the geometry of individual fractures, the volume over which the connected fracture network extends, and the total connected surface area of the fracture network. Therefore, if fracture network connectivity can be accurately characterized, the likelihood that a geothermal resource can be successfully developed can be assessed.

Fracture network connectivity of a geothermal reservoir can be assessed through the development of representative fracture models. The development of fracture models

begins with the collection of individual fracture properties which can be directly measured in-situ or through laboratory testing. Through the interpretation and analysis of individual fracture properties, spatial and physical relationships can be established between individual fractures. Fracture models are the product of the extrapolation of these inter-fracture relationships over the reservoir volume. Because the geometric properties of fracture networks are inferred through the interpretation of individual fracture measurements and the development of fracture models, varying degrees of geological uncertainty are inherent in fracture network connectivity assessments. The amount of geological uncertainty associated with fracture connectivity assessments is proportional to the amount of geological data available to characterize fracture network properties. Furthermore, direct measurement of individual fractures can be subject to sampling biases and human error, which introduces further uncertainty into fracture network connectivity assessments.

The collection of geological data for the purpose of characterizing fracture networks can be costly, and at times impossible, due to the extreme depths of geothermal reservoirs and the effects of high temperature on borehole instrumentation performance (Armstead and Tester 1987). Moreover, these costs are incurred early in the project life when there is minimal geological data available for the fracture network characterization. It follows that geothermal projects at the prefeasibility-level suffer from high developmental risks due to high exploration costs, coupled with high geological uncertainty associated with fracture network connectivity assessments. In order to minimize developmental risk, there is a need to maximize the efficiency in which geological information is collected at

the prefeasibility-stage of a geothermal project so that the connectivity of the existing fracture network can be quickly, objectively and accurately assessed.

The findings from previous feasibility studies of the Meager Mountain area show that a high temperature geothermal resource exists at the Meager Creek site; however sustainable yields of geothermal fluids could not be produced due to the fact that test wells did not intersect a connected, permeable fracture network. To date, no extensive fracture network analysis has been completed of the basement rocks underlying the Meager Creek site, and the connectivity of the existing fracture network is unknown. It is proposed that a detailed analysis of historical geomechanical and hydrological data collected from the Meager Mountain area can be used to interpret the fracture network connectivity of the Meager Creek site. This will provide a greater understanding into why past attempts to develop the site were unsuccessful, and if measures can be taken to increase the likelihood of successfully developing the site in the future. The analyses included in this thesis also provide a procedure for analysing fracture data for the purposes of interpreting fracture network connectivity for future geothermal projects.

1.2 Research Objectives

This thesis has three principle research objectives. The first objective is to conduct a comprehensive audit of the available geomechanical and hydrogeological data that has been collected from the Meager Creek site since the mid 1970's. Site investigations were carried out intermittently over three decades between the early 1970's to early 2000's by various contractors and energy companies. A single database consisting of

geological data relating to the structural characteristics of the existing fracture network at the Meager Creek site was achieved through the consolidation and digitization of numerous engineering reports and technical papers. The consolidation of this vast amount of geological information will serve future development projects of the Meager Creek geothermal site.

The second research objective is to identify the geometric fracture properties that can be collected during prefeasibility-level field investigations which have the greatest influence on fracture network connectivity assessments. The connectivity of fracture networks was assessed through the development of discrete fracture network (DFN) models of the site. Identification of the fracture properties that have the greatest influence on fracture network connectivity assessments serves future geothermal developers by prioritizing the type of fracture data that should be collected during prefeasibility-level field investigations.

A review of the available engineering reports and published literature indicate that no detailed analysis of the existing fracture connectivity at the Meager Creek site has been completed to date, and no attempt has been made to model the existing fracture network at the site. The third research objective is to develop a prefeasibility-level DFN model using historical geological information from the Meager Creek site so that the overall extent and connectivity of the existing fracture network within the crystalline basement rocks can be assessed. Through the assessment of overall fracture network

connectivity, the likelihood that the Meager Creek site can be successfully developed in the future can be inferred.

1.3 Thesis Organization

The thesis is organized into seven chapters and three appendices:

- Chapter 1 provides the problem statement and research objectives of the thesis;
- Chapter 2 reviews the basic mechanisms of high temperature geothermal systems and the terminology used to characterize individual fractures and connected fracture networks. The theory behind fracture network characterization and DFN modelling and how it can be applied to the design of geothermal projects at the prefeasibility-level is also discussed;
- Chapter 3 provides an overview of the Meager Creek site and summarizes the historical field investigations that have taken place from 1975 to the present;
- Chapter 4 summarizes the geological information obtained from historical slim hole drilling and surface mapping programs used to create DFN models of the Meager Creek site. The techniques used to interpret and convert fracture parameters into stochastically representative fracture sets are presented;
- Chapter 5 provides a description of the methodology used to create individual DFN models and how fracture network connectivity was assessed using DFN simulations. Connectivity assessments derived from DFN simulations based on two different geological models used to represent the Meager Creek site are presented;

- Chapter 6 summarizes the key findings from the analyses presented in chapter 5 and provides recommendations for future work; and
- Chapter 7 is a list of references cited throughout the thesis.

1.4 Use and Limitations

This thesis provides an extensive review and analysis of historical data collected from the Meager Mountain geothermal area. Due to limitations of the available data, many assumptions and idealizations were required during the development of the DFN models used to evaluate fracture network connectivity. Even though these assumptions and idealizations were made using the author's best judgement, the results of the subsequent analyses should not be considered definitive and are not intended to be used for prospective purposes.

CHAPTER 2: LITERATURE REVIEW

The multidisciplinary scope of this thesis led to a literature review of subjects that include high temperature geothermal systems, rock mass classification, characterization of individual fractures, and the representation of fracture networks using discrete fracture network (DFN) modelling. Section 2.1 reviews the role of fracture networks in geothermal systems and the importance of fracture network connectivity in relation to the production potential of a geothermal resource. Section 2.2 reviews the geometric parameters used to describe fracture systems. Section 2.3 develops the conceptual model used to describe fluid flow in fractured media and the benefits and limitations of DFN modelling as an analytical tool in the field of rock mechanics.

It is important to establish a consistent terminology prior to beginning the literature review. A *rock mass* is a volume of rock comprised of an assemblage of smaller volumes of intact rock (rock blocks) that are separated from one another by fractures or discontinuities. The terms *fracture* and *discontinuity* are often used interchangeably when describing “breaks” in an otherwise intact rock mass. According to a poll completed by the International Society for Rock Mechanics (ISRM) Commission on Standardization of Laboratory and Field Tests, the term *discontinuity* was preferred over *fracture* to be used as the collective term to describe all joints, faults, bedding planes, and contacts (ISRM 1978). In spite of this, the term *fracture* is still ubiquitous in the rock mechanics literature. In many instances, it would be inappropriate to use the term *discontinuity* in lieu of *fracture*, as is the case for the term discrete *fracture* network modelling. In the interest of maintaining consistent terminology throughout this thesis,

the term *fracture* is used to describe all types of natural and mechanical breaks within a rock mass.

There are many types of fractures that occur naturally in rock masses. Fractures can be classified based on a number of criteria that include fracture geometry, formation process, and mesoscopic cohesiveness during deformation (Van Der Pluijm and Marshak 1997). A brief explanation of common fracture types is provided in Table 2.1.

Table 2.1 Definition of common fracture types

FRACTURE TYPE	DESCRIPTION
Bedding	A primary fabric in sedimentary rocks that forms during deposition and manifests due to changes in texture, colour, and/or composition. Bedding planes can lead to the development of bedding-parallel fractures, referred to as bedding joints or bedding-parallel parting.
Vein	A fracture that has been filled in by minerals that precipitated from a hydrous solution that flowed through the fracture
Dike/sill	Sheet intrusions that are often oriented sub-vertically/sub-horizontally in unstratified sequences. In general, dikes and sills form perpendicular to the direction of least principal stress.
Fault/shear zone	A type of fracture where movement parallel to the fracture surface can be observed. A more restrictive definition of a fault further specifies that slip along a fault surface is primarily due to brittle deformation processes. This definition distinguishes faults from shear zones, which are the result of ductile deformation processes.
Joint	A natural fracture that is formed by tensile-loading. No noticeable shear displacement can be observed along a joint surface.

Modified from (Van Der Pluijm and Marshak 1997)

2.1 The Role of Fractures in High Temperature Geothermal Systems

Geothermal energy refers to the energy stored as heat within the interior of the earth. The heat stored within the earth is a product of the natural decay of radioactive elements (primarily Uranium, Thorium, and Potassium), and the primordial heat generated from the original formation of the planet (Grasby et al. 2011). Heat is constantly flowing from the centre of the earth and dissipating at the surface, giving rise to a natural thermal gradient which is equal to 30°/km on average (Barbier 2002). The relatively low thermal gradient of the earth means that crustal rocks that have temperatures high enough for power generation are typically located at depths that are either inaccessible or not economical using modern drilling techniques.

2.1.1 Types of Geothermal Systems

A geothermal resource is the product of geological processes that concentrate a large amount of heat so that the local thermal gradient is much higher than the global average. For instance, in areas of active volcanism local thermal gradients can be greater than 100°/km (Barbier 2002). In order to develop a geothermal resource, the depth of the resource must be shallow enough so that it is accessible by modern drilling technology.

2.1.1.1 Conventional/Hydrothermal systems

One of the most common geological processes that lead to the development of a geothermal resource is the emplacement of a magmatic intrusion near the surface of the earth. The magmatic intrusion heats the surrounding rocks and fluid, leading to

convective circulation of fluids within permeable reservoir rocks. These fluids may migrate to the surface via connected fractures pathways or faults, which leads to the creation of hot springs or steam vents at surface. At the same time, the fluid that is lost to the surface is recharged at depth by the percolation of surface water through fractures and faults. Once the surface water reaches the depth of the magmatic intrusion, it is heated and the cycle continues. Geothermal systems that naturally develop convective circulation of high temperature fluids at depth and are recharged by the downward migration of surface water are referred to as hydrothermal systems. A schematic of a typical hydrothermal system is shown in Figure 2.1.

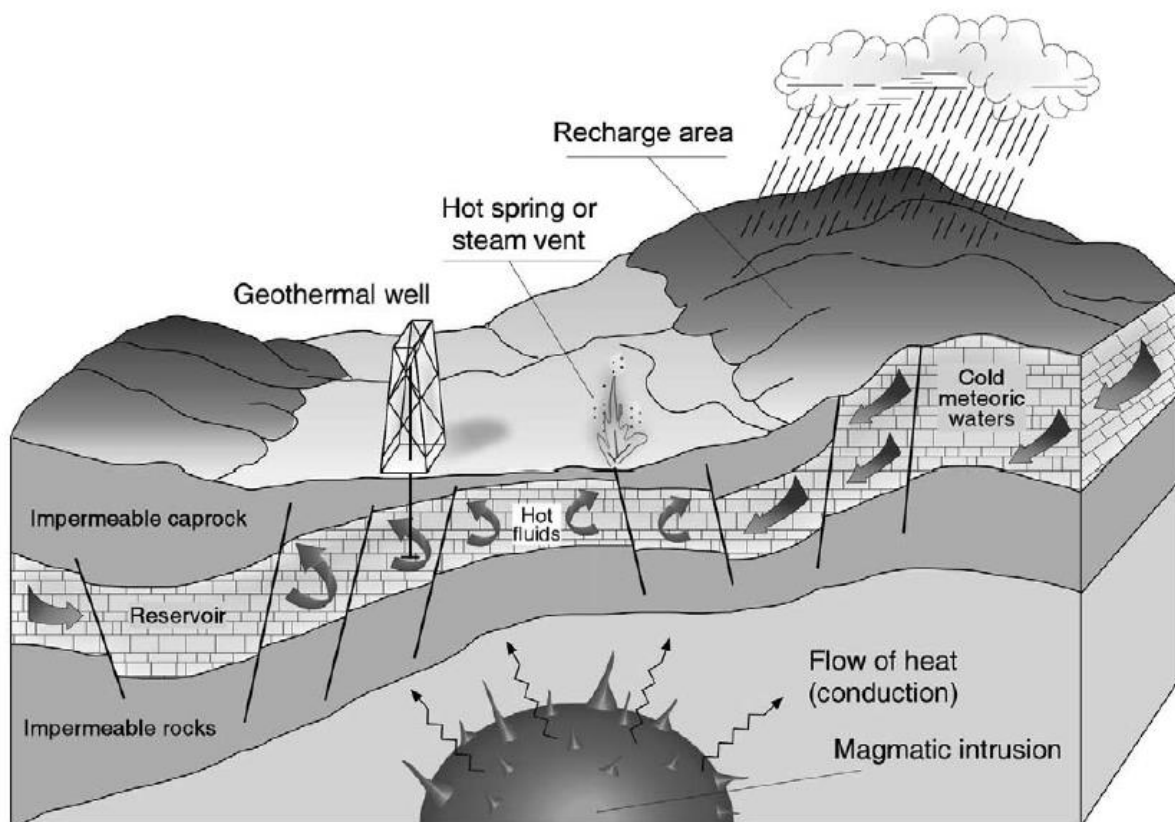


Figure 2.1 The role of the water cycle in sustaining geothermal systems. From (Barbier 2002)

2.1.1.2 Enhanced Geothermal Systems (EGS)

Enhanced geothermal systems (EGS) differ from hydrothermal systems in that insufficient permeability exists in the reservoir rocks to permit convective fluid flow. Without the natural circulation of fluids at depth, geothermal wells cannot effectively recover the thermal energy that is contained within the reservoir rocks. To facilitate the flow of fluids at depth, high-pressured fluids are injected into the reservoir in order to stimulate the reservoir rocks and create new connections between existing fractures. Once sufficient fracture connectivity exists within the reservoir rocks, high temperature geothermal fluids are extracted through production wells and are replaced by pumping cooler fluids back into the reservoir via injection wells. A schematic of a simple two-well EGS system is shown in Figure 2.2.

The main advantage of EGS technology is that the thermal energy of the earth can be recovered and used to generate electricity from any location where high temperature rocks can be accessed by modern drilling technology, whereas conventional hydrothermal systems are mostly limited to tectonic plate boundaries where these systems occur naturally.

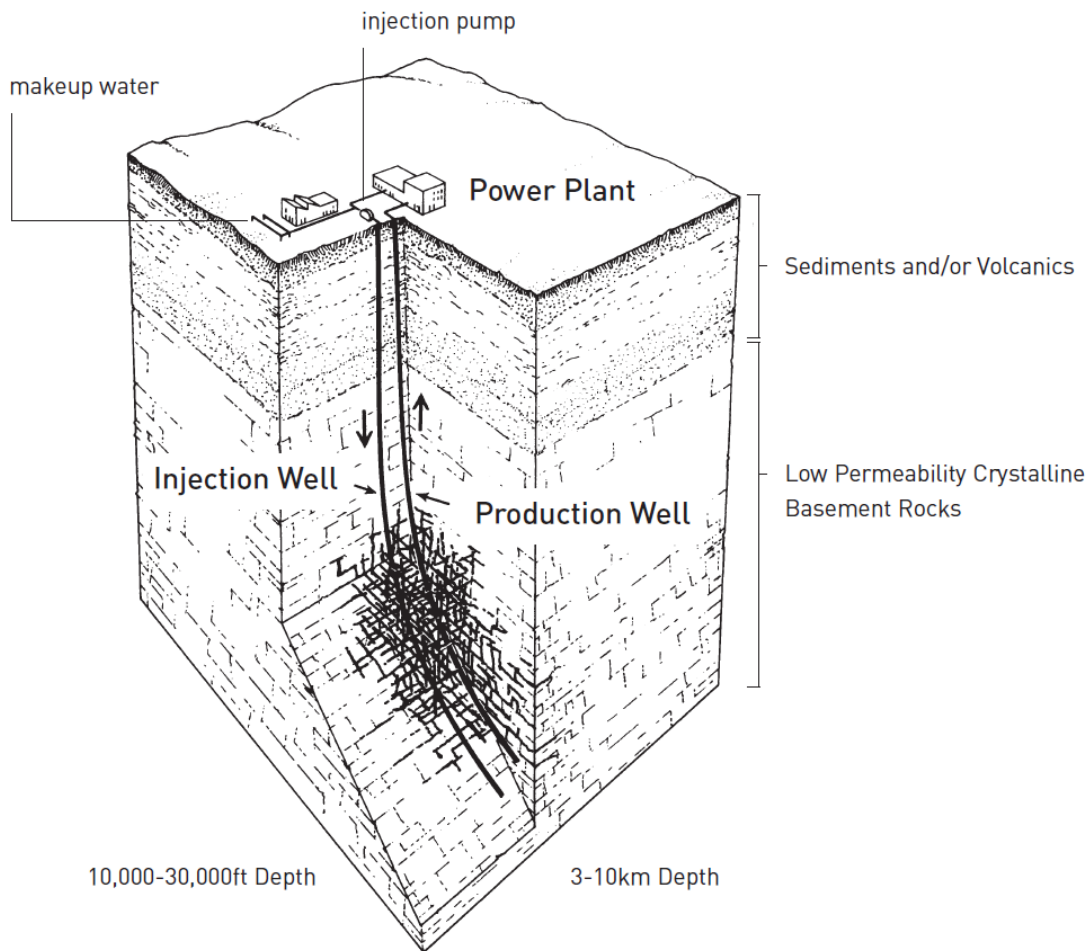


Figure 2.2 Schematic of a two-well EGS system. From Tester et al. (2006)

2.1.1.3 Cost of Conventional Versus EGS Wells

The drilling of exploration, testing, and production wells constitute a significant percentage of the total capital costs of a geothermal project. Drilling-related costs have been reported to range from 30% to 60% of total capital costs for high and low grade geothermal resources respectively (Tester, Anderson, and Batchelor 2006). For conventional geothermal wells, the average cost is approximately \$800 – 1200 USD per metre, with average total well costs ranging between \$1.5 – 3.0 Million USD per well (Barbier 2002).

Drilling cost per well are typically greater for EGS systems compared to conventional geothermal systems. This is because there are additional costs associated with the hydraulic stimulation of the relatively impermeable reservoir rocks. The average cost per stimulation for an EGS well ranges from \$200,000 - \$450,000 USD per zone (Grasby et al. 2011). A comparison of cost versus depth for historical conventional and EGS wells is presented in Figure 2.3. It can be seen that at a depth of 3 km, the average cost of an EGS well may be up to \$5 – 7 Million USD more than a conventional well, and that conventional wells have an average total cost comparable to average oil and gas wells. It can also be seen that well cost tends to increase non-linearly with depth.

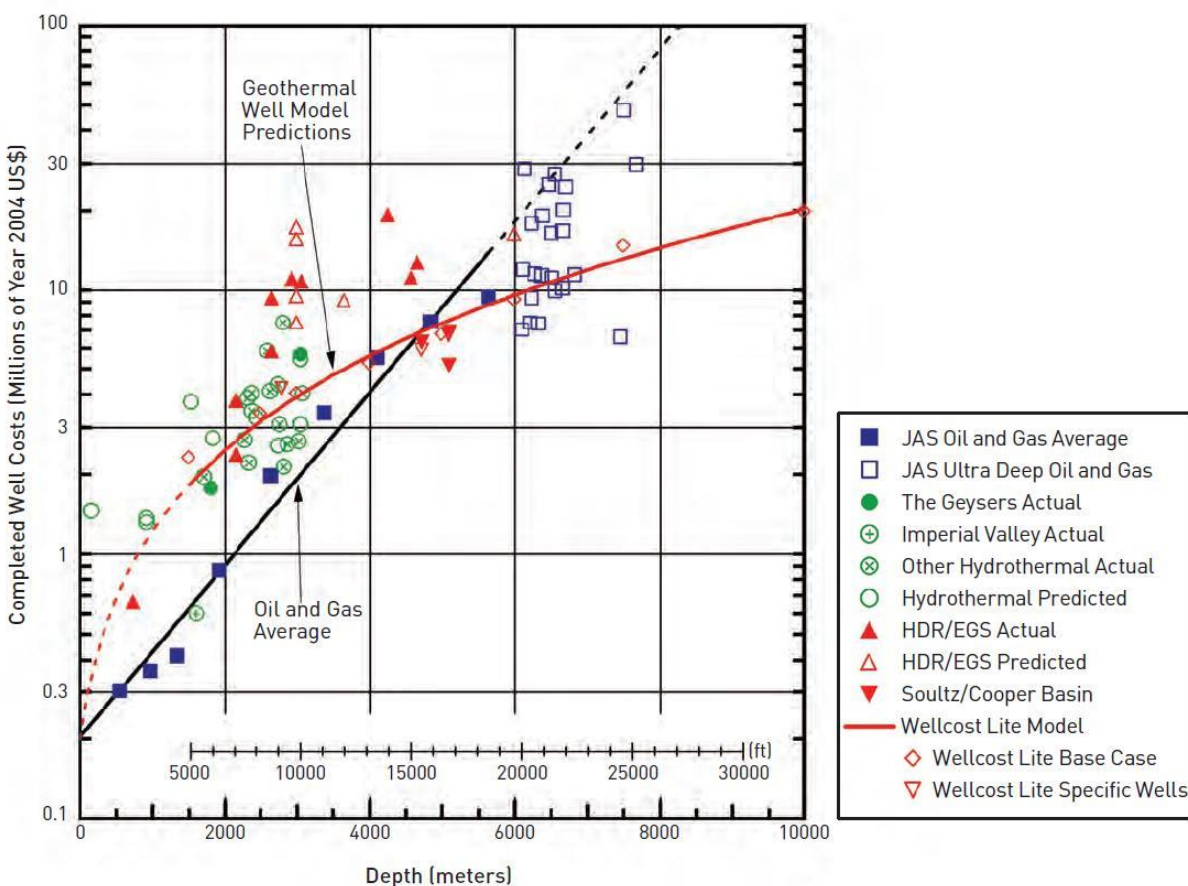


Figure 2.3 Cost comparison of conventional and EGS geothermal wells. Prices are in 2004 \$USD.
From Tester et al. (2006)

The cost implications are significant if hydraulic stimulation is required for production and injections wells, which is largely dependent on the overall connectivity of the existing fracture network. Therefore, it is important to maximize the amount of geological information collected during exploratory and prefeasibility field investigations so that fracture network connectivity can be accurately assessed early in the project life.

2.1.2 Temperature Ranges of Geothermal Resources

Geothermal resources are often classified based on the average reservoir temperature. Low temperature systems typically have reservoir temperatures less than 80°C, and are only suitable for direct heating applications. Medium and high temperature systems have reservoir temperatures of 80 – 150°C and >150°C respectively, and both have the potential to generate electricity at the commercial scale (Grasby et al. 2011).

The main distinction between medium and high temperature geothermal systems is the type of technology required to convert thermal energy to electrical energy. In the case of medium temperature systems, a binary-cycle plant is often required. Binary-cycle plants circulate the extracted geothermal fluids past a secondary fluid that has a lower boiling point than water. Heating of the secondary fluid causes it to boil, and the vapour produced is used to power an electrical turbine. High temperature systems utilize either flash steam or dry steam power plants. Flash and dry steam power plants do not require a secondary working fluid because the geothermal fluid will be converted to steam once it is brought to surface due to the drop in confining pressure, coupled with the high temperature of the fluid. The steam produced is used to power an electrical turbine.

2.1.3 Heat Transfer in Geothermal Systems

The amount of energy that can be extracted from any type of geothermal system is largely dependent on the characteristics of the natural fracture network. The critical role of fractures in geothermal systems is better understood by an examination of the physical processes that govern heat flow in a fractured rock mass.

With respect to geothermal systems, heat is primarily transferred by either conduction or convection. Conductive heat transfer is defined as the transfer of kinetic energy between molecules without the overall transfer of material, and is the primary method of heat transfer through intact rock (Barbier 2002). Conduction is also the mechanism in which hot crustal rocks transfer heat to fluids when they are in direct contact with one another. The rate at which heat is transferred by conduction in the earth's crust is a function of the existing thermal gradient and the thermal conductivity of the crustal rocks. Thermal conductivity is an intrinsic property of rocks, and is defined as the amount of heat conducted per second through a cross-sectional area of 1 m^2 under a temperature gradient of 1°K/m , acting perpendicular to the cross-sectional area. Studies have shown that the majority of heat transfer within the earth's crust is primarily due to conduction (Beardsmore and Cull 2001).

In convective heat transfer, heat energy is distributed due to the movement of gases and liquids. In geothermal systems, convective heat transfer is primarily due to the movement of water in the subsurface. Given the relatively high specific heat capacity of water, large amounts of heat energy can be transported large distances relatively

quickly via convection, assuming that water is allowed to flow freely. Therefore, the rate at which heat energy can be transported via convection, and more importantly the rate at which heat can be extracted from a geothermal system via production wells, is largely dependent on the permeability of the host rocks.

In a fractured crystalline rock mass the permeability of fractures may be several orders of magnitude greater than that of the intact rock matrix, which means that fluid flow is largely constrained to the connected portion of the fracture system. As a result, the amount of heat that is transferred via convection is dependent on the extent and permeability of the connected fracture network. Therefore, characterization of the fracture network is required to properly estimate the production potential of a geothermal resource.

2.1.4 Fractured Volume in Relation to Production Potential

The fractured volume refers to the three-dimensional space over which a connected fracture network extends. In a study by Sanyal and Butler (2005), sensitivity analyses were completed to assess the impacts of fractured volume, fracture spacing, permeability, porosity and injection/production well configuration on net electrical production of a geothermal system. It was found that the fractured volume of a geothermal reservoir is the most sensitive parameter affecting the amount of recoverable heat, and that a factor of 26 MW_e/km³ of net electrical power output per fractured volume can be expected for a wide range of reservoir properties. The study

shows that the extent of the connected fracture network has a strong impact on the amount of heat that can be recovered from a geothermal resource.

2.2 Fracture Network Characterization

A complete description of a fractured rock system can be described by three classes of fracture information: geometric characteristics, distributional parameters, and fracture properties (Dershowitz 1984). Geometric characteristics provide information about the shape, size, planarity, spacing, intensity, and orientation of individual fractures. Distributional parameters provide information relating to the statistical distribution of geometric characteristics. Fracture properties include fracture stiffness, strength, roughness, and effective hydraulic aperture. The following subsections are limited to discussions of the geometric characteristics of fractured rock systems given that the scope of this thesis is the estimation of the overall extent and connectivity of discrete fracture networks using geological data typically collected during prefeasibility-level field investigations.

2.2.1 Geometric Characteristics of Individual Fractures

The characteristics of fracture networks are derived from those of the individual fractures. Therefore, it is important that geothermal projects include the collection and measurement of individual fractures properties in prefeasibility-level field investigations. These individual fracture properties include fracture shape, size, planarity, aperture, and orientation.

2.2.1.1 Shape

The shape of a fracture within a rock mass is dependent on a number of geological factors that include rock type, stress history, location relative to other existing fractures, and the magnitude and orientation of the local stress field. Consequently, it is reasonable to assume that a variety of fracture shapes will exist within a single rock mass. However, fractures are commonly represented in fracture models using basic shapes because they lead to more tractable analysis and simulation of fracture systems (Dershowitz 1984). It is often impossible to directly observe the complete three-dimensional shape of a fracture within a rock mass, so simplifying assumptions with respect to the shape must be made. Shapes commonly used to represent individual fractures include polygons, circles, or ellipses.

Polygonal fractures are likely to form when the growth of the fracture is limited by the existence of an adjacent fracture or geologic feature. Warburton (1980) developed a statistical joint model that assumes parallelogram-shaped joints. It was found that this model was capable of simulating joint trace patterns that are commonly observed in rock outcrops.

The representation of fractures as circles can be found in the literature Baecher et al. (1977), and their existence in nature has been inferred in a study of nearly 9,000 fracture traces from a mine location in South Africa (Robertson 1970). However, Zhang and Einstein (2009) completed a literature review of studies that inferred fracture shapes based on measured joint trace lengths in rock exposures. Their conclusion is

that fractures may occur as circular discs, however they are rare in nature and should be considered a special case of elliptical fractures.

Elliptical fractures are most likely to form in unbounded or weakly bounded rock masses where individual fractures are unlikely to have intersected pre-existing fractures or geological features during fracture growth. The assumption of an elliptical shape provides reasonable representation of many real fractures, and it has been shown to correlate well between observed fracture trace lengths and fracture size (Zhang et al. 2002).

2.2.1.2 Trace Length and Fracture Size

The fracture size distribution has a strong influence on the overall connectivity and extent of fracture networks. Fractures can range in size from several microns to hundreds of kilometers; therefore a detailed assessment of the true fracture size distribution is paramount to developing representative fracture network models. The true size of a fracture is rarely known with a high degree of certainty, and is typically inferred from the length of the line of intersection between the fracture and a two-dimensional plane, referred to as the trace length. Fracture sizes must be inferred because direct observation and measurement of entire fracture planes is often impossible or impractical. In practice, trace length measurements can be obtained from the mapping of natural rock outcrops, excavated faces, or the walls of tunnels and mine drifts. Once a large number of measurements have been compiled, the trace length population can be represented using common probability distribution functions, which in turn is used to

infer the fracture size distribution. Several studies have presented methodologies on how to derive fracture size distributions from trace length distributions that differ depending on factors such as the assumed fracture shape, observed trace length distributions, and the treatment of biases associated with trace length sampling methodology.

Deriving fracture size distributions from trace length distributions requires that several simplifying assumptions are made with respect to the nature of the fracture properties.

Common assumptions that are made include:

- The shape of fractures are planar, circular discs;
- The location of fracture centres are randomly and independently distributed in space; and
- The size distribution of fractures is independent of spatial location.

Studies that infer fracture size distributions from trace length populations often assume that fractures are circular and planar. Although there is some evidence that fractures may be circular in shape (see section 2.2.1.1), this assumption is made largely due to mathematical convenience (Zhang and Einstein 2000). Both Dienes (1979) and Kulatilake and Wu (1986) have presented mathematical solutions that can be used to infer the diameter distribution of circular fractures by fitting common probability distributions to a sample of observed trace lengths. In a study by Decker and Mauldon (2006), a differential evolution algorithm was used to estimate the size of rectangular fractures given trace length distributions collected from two or more non-parallel planes.

Studies have shown that several distribution forms may be fitted to trace length populations; however the relationship between the distribution parameters (population mean and standard deviation) for the trace length and fracture size populations can be complex. In a study by Barton (1978), it was found that the standard deviation of the trace length population is greater than that of the fracture diameter population, and that the ratio of mean trace length to mean diameter is likely to increase as the standard deviation of the latter population increases. Consequently, applying constant conversion factors to the trace length distribution parameters in order to derive the fracture size distribution parameters can lead to erroneous results. Kulatilake et al. (1993) investigated the suitability of exponential, gamma, lognormal, and normal distributions on four joint sets identified in a ventilation drift at the Stripa Mine in Sweden. The study found that both exponential and gamma distributions provided reasonable fits to the sampled trace lengths. Studies completed by Barton (1977) and Baecher et al. (1977) show that lognormal distributions also provide reasonable fits for trace length data. Zhang and Einstein (2000) presented a methodology where the mean and standard deviation of the trace length population obtained from circular area mapping is used to derive lognormal, negative exponential, and gamma distributions for the fracture diameter distribution. Priest (2004) identified a new distribution, called the Wicksell distribution, which is characterized by having identical distribution forms for both the fracture diameters and complete traces on a cutting plane.

Prior to fitting statistical distributions to a population of trace length measurements, the data must be corrected for sampling biases. Uncorrected populations of measured trace

lengths will be inherently biased depending on the sampling methodology (i.e. window vs. line sampling). The type of biases inherent in trace length sampling include size, truncation, and censoring biases (Baecher and Lanney 1978). A size bias exists because large trace lengths are more likely to intersect sampling lines and windows, therefore they will tend to be oversampled in a given population. Truncation bias refers to the under-sampling of trace lengths that fall below a minimum threshold. Truncation bias occurs because there is a practical limitation to the minimum trace length that can be measured in the field. Censoring bias occurs when trace lengths extend beyond the limits of the mapped exposure so that only a lower-bound estimate of the actual extent of the trace length can be measured. A summary of the biases that arise from line sampling are presented in Priest and Hudson (1981) and Kulatilake (1993), and summaries of the biases that arise from rectangular and circular mapping can be found in Kulatilake et al. (1993) and Zhang and Einstein (2000) respectively.

The relationship between trace length and fracture size is difficult to derive with a high degree of certainty. In the context of assessing fracture network connectivity, studies have shown that fracture length is the most critical fracture parameter in assessing connectivity in two-dimensional fracture networks (Long and Witherspoon 1985). It is important to acknowledge the assumptions made when inferring fracture size distributions from a population of trace length data, and to correct these populations for biases that are inherent in all sampling methods.

2.2.1.3 Planarity

Planarity and roughness are measures of the inherent surface waviness and unevenness of a fracture relative to its mean plane (Brady and Brown 2004; ISRM 1978). Fractures are often idealized as perfectly planar features, whereas in reality fracture surfaces often deviate from that of an ideal plane. Dershowitz and Einstein (1988) use the terms roughness and waviness to describe deviations from planarity at a small scale (<1 mm) and large scale (>1 mm) respectively. Figure 2.4 illustrates the scale of roughness and waviness of a hypothetical fracture surface, as defined by Dershowitz and Einstein (1988).

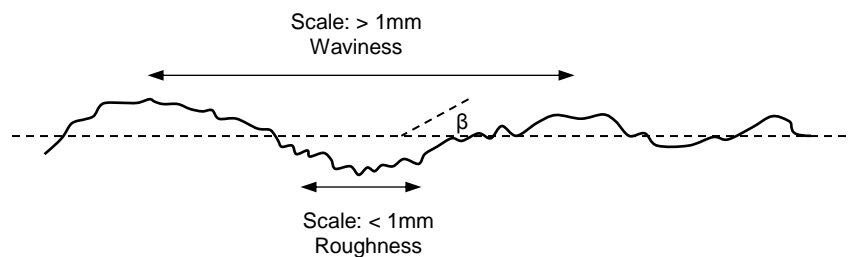


Figure 2.4 Non-planar fracture surface indicating the scales of roughness and waviness, in accordance with Dershowitz and Einstein (1988). Waviness can be expressed in terms of the angle, β .

Stepped, undulating, or planar are three general terms used to characterize waviness. Characterization of fracture waviness is important, as it can influence the flow behaviour of the fracture system such as tortuosity. The influence of waviness on the hydro-mechanical behaviour of a fracture network is greater when fracture aperture is low, which is likely the case for rock located at several kilometres depth.

2.2.1.4 Aperture

Aperture is defined as the perpendicular distance between the adjacent walls of an open fracture in which the intervening space is filled with either air or water (Brady and Brown 2004). The aperture of a fracture is commonly represented using a constant or average value, which allows for the calculation of fracture transmissivity using the cubic equation of fracture flow proposed by (Snow 1965):

$$T = \rho g \frac{e^3}{12\mu} \quad \text{Equation 2.1}$$

where

T = Transmissivity

ρ = Fluid density

g = Gravitational acceleration

e = Aperture

μ = Fluid viscosity

Based on the cubic law, a strong relationship exists between fracture aperture and fracture network connectivity. Minor increases in fracture aperture result in relatively large increases in transmissivity, which explains the heterogeneous behaviour of fluid flow observed in fractured rock masses (Doe 2010). Conversely, a minor decrease in fracture aperture can cause a fracture to no longer act as a pathway for fluid flow, which explains the commonly observed behaviour that fluid flow in fractured media is often dominated by a small percentage of the observed fractures (Long et al. 1991; Cohen 1995; Billaux et al. 1989).

Fracture aperture has a strong effect on fracture network connectivity because the low-transmissivity of tight fractures may be insufficient to permit fluid circulation. Fracture apertures measured in borehole walls or surface outcrops may be much larger than the true aperture of a fracture at depth, which will lead to an over-estimation of the bulk permeability of the fractured rock mass. The relatively small apertures of fractures located at depth infer that only a small percentage of fractures belonging to connected fracture networks have sufficient transmissivity to permit fluid flow. This must be accounted for when developing fracture network models for the purpose of modelling fracture network connectivity.

2.2.1.5 Orientation

The orientation of a fracture plane in three-dimensional space can be described using two measurements. The first is the dip of a fracture, which is the angle between the line of maximum declination on the fracture surface and the horizontal plane. The second is the dip direction, which is equal to the azimuth of the line of maximum declination, measured clockwise from true north. The strike of a fracture is sometimes reported instead of the dip direction, which is equal to the azimuth of a line perpendicular to the line of maximum declination (Brady and Brown 2004).

Geological processes that naturally produce fractures in rock tend to generate clusters of fractures that have sub-parallel orientations (Priest 1993). These clusters are often referred to as fracture sets, and the properties of fractures belonging to a fracture set can be described using statistical distributions. The delineation of fracture sets is useful

when constructing fracture models of geothermal systems. Given the depths at which geothermal resources are located, it is impossible to directly measure all of the existing fractures within the host rock. However, the distribution of fractures and the expected fracture properties within the host rock can be inferred if distinct fracture sets can be identified and characterized from outcrop mapping, or the mapping of fractures in the wall of boreholes.

2.2.2 Fracture Network Properties

In addition to the geometric properties of individual fractures, the spatial relationship between individual fractures must be characterized in order to construct representative DFN models of geothermal systems. The spatial relationship of individual fractures in fracture networks are defined by the location of individual fractures, the spacing of fractures belonging to distinct fracture sets, and fracture intensity.

2.2.2.1 Location of Individual Fractures

The location of a fracture in three-dimensional space can be referenced by the centre of the fracture plane, or by the location of the plane boundaries. The delineation of the exact location and extent of regional fractures (e.g. faults) is important because it can be shown that they have a significant impact on the overall connectivity of fracture networks (see section 5.3). If there are relatively few extensive fractures that intersect an area of interest, they can be represented explicitly in a DFN model.

The location of individual fractures belonging to a fracture set that exhibits regular spacing can be modelled using deterministic processes. In the case of even spacing, the location of fractures can be specified along an evenly spaced grid (Snow 1965). If fracture spacing is observed to increase at a predictable rate away from specific boundaries, geometric or arithmetic series can be used to specify the location of individual joints.

If the location of fractures cannot be determined using explicit or deterministic processes, stochastic processes can be used. The most common stochastic process used to define joint location is the Poisson process, where the location of individual fractures is independent of the location of adjacent fractures. According to Poisson process, the location of fractures in the x, y, z direction are distributed following a uniform distribution, which leads to an exponential distribution of fracture spacing along a sampling line in any direction (Dershowitz 1984; Priest and Hudson 1976). It follows that if the observed distribution of fracture spacing measured in boreholes or exposed outcrops follow an exponential distribution, the location of fractures in space can be modelled stochastically using a Poisson process.

2.2.2.2 Spacing

The definition of fracture spacing is not consistent throughout the rock mechanics literature. Some sources define spacing as the mean distance between adjacent fractures that belong to a single fracture set, measured perpendicular to the average orientation of the fracture plane. Spacing may also refer to the distance between

adjacent fractures along a particular scan line, regardless of the orientation of the adjacent fractures. For the purposes of this report, the term 'true spacing' will be used to refer to the former definition, and 'spacing' will be used to refer to the latter definition.

The International Society for Rock Mechanics (ISRM) provides suggested methods for measuring true spacing (ISRM 1978). It is important to recognize that exposed fractures in a rock face belonging to the same fracture set are likely to have sub-parallel orientations, and are also unlikely to be perfectly planar. Therefore, true spacing is dependent on the measurement location taken along the fracture plane. This presents a practical limitation on the degree of accuracy inherent in all spacing measurements.

It was found that clustered, randomly spaced, or a combination of clustered and randomly spaced fractures located along a scan line typically follow a negative exponential distribution (Priest and Hudson 1976). Other distributional forms that have been used to model fracture spacing include lognormal (Bridges 1975) and negative exponential distributions (Priest and Hudson 1976; Call et al. 1976; Baecher 1983). The majority of studies reviewed indicated a negative exponential distribution is the most likely distribution to describe fracture spacing along a scanline.

2.2.2.3 Intensity, P10 and P32

In general terms, fracture intensity is a measure of the density of fractures within a rock mass. The units of measurement for fracture intensity are non-unique, and depend on the dimensionality of the fracture measurement and sampling region. For example,

measures of fracture intensity include the number of fractures that are intersected by a scanline (#/m), the total surface area of fractures within a unit volume of rock (m^2/m^3), and the total fracture volume per unit volume of rock (m^3/m^3). The Pxy notation system provides a more universal definition of fracture intensity by incorporating the dimensionality of the sampling region, x, as well as the dimensionality of the fracture measurement, y, and has been used throughout the DFN modelling literature (Dershowitz 1984; Lefranc et al. 2011). A summary of the Pxy fracture intensity notation system is provided in Table 2.2.

Table 2.2 Pxy fracture intensity notation and the relationship between the dimensionality of the rock mass sample and measurement dimension. Modified from Golder Associates Inc. (2011)

		MEASUREMENT DIMENSION			
		0	1	2	3
SAMPLE DIMENSION	1	P10: Number of fractures per unit length of borehole	P11: Length of fractures per unit length of borehole		
	2	P20: Number of fractures per unit area	P21: Length of fractures per unit area	P22: Area of fractures per unit area	
	3	P30: Number of fractures per unit volume		P32: Area of fractures per unit volume	P33: Volume of fractures per unit volume

The most common measurements of fracture intensity in DFN modelling are P10 and P32. P10 is the average number of fractures per unit length, and can be determined from borehole surveys and line mapping of surface outcrops or mine drifts. With the aid of DFN modelling software, some studies have used P10 measurements obtained from

well logs to infer volumetric fracture intensities (Rogers et al. 2010). The limitation of this method is that P10 is a linear measurement of fracture intensity and is subject to sampling biases. More importantly, the extrapolation of 3D fracture network intensities from 1D fracture measurements lead to non-unique solutions (Billaux et al. 1989; Long et al. 1991). Regardless, P10 values can be used to verify if the distribution of fractures simulated in a DFN model can reproduce the linear fracture intensity observed in actual well logs.

P32 is the total fracture surface area per unit volume. With respect to geothermal reservoir modelling, the P32 of an existing connected fracture network is useful in gauging the amount of heat that can be extracted from a potential reservoir. If a working fluid is circulated through a fracture network with a high P32 value, heat will be transferred from the host rock to the working fluid via conduction more efficiently due to the higher density of fracture surface area per volume. In practice, P32 cannot be directly measured but can be inferred through DFN model simulation.

2.2.3 Influence of Connected Fracture Networks on Recoverable Heat

In order to assess the potential of a geothermal resource, the total and recoverable thermal energy must be estimated. The recoverable thermal energy is the actual amount of thermal energy that can be extracted from a volume of rock, and is expressed in terms of a recovery factor. The recovery factor of a geothermal resource is defined as the actual amount of thermal energy that can be extracted divided by the total in-place thermal energy.

$$F_r = \frac{Q_{rec}}{Q_{Tot}} \quad \text{Equation 2.2}$$

$$F_r = \frac{\rho V_{frac} C_r (T_{r,i} - T_{r,a})}{\rho V_{tot} C_r (T_{r,i} - T_o)} \quad \text{Equation 2.3}$$

where

F_r = Recovery Factor

Q_{rec} = Recoverable thermal energy from the reservoir

Q_{tot} = Total thermal energy from the reservoir

ρ = Rock density (kg/m³)

V_{frac} = Fractured reservoir volume (m³)

V_{tot} = Total reservoir volume (m³)

C_r = Rock specific heat (J /kg · °C)

$T_{r,i}$ = Mean initial reservoir rock temperature (°C)

$T_{r,a}$ = Mean rock temperature at abandonment (°C)

T_o = Mean ambient surface temperature (°C)

Modified from (Tester et al. (2006)).

From Equation 2.3, it can be seen that the amount of recoverable thermal energy from a geothermal reservoir is directly proportional to the volume of fractured rock, V_{frac} . This is because geothermal wells can only extract heat that is transferred via convection, and convective heat transfer is limited to the network of connected fractures in the reservoir rocks. It follows that geothermal reservoirs that have connected fracture networks that extend over a large percentage of the reservoir volume have large recovery factors. The volume of fractured rock in a geothermal reservoir cannot be measured directly, but it

can be estimated using DFN modelling methods. By estimating the volume of fractured rock, the amount of thermal energy that can be extracted from a geothermal resource can be estimated.

2.3 Discrete Fracture Network Modelling of Geothermal Systems

Discrete fracture network (DFN) modelling is a method that can be used to model fluid flow and transport processes in fractured rock masses. Unlike equivalent continuum rock mass models, DFN models can represent the geometric characteristics of connected fracture networks in rock masses through the stochastic simulation of discrete fractures over a model area/volume (Jing and Hudson 2002).

2.3.1 Conceptual Model of a Crystalline Rock Mass

The appropriateness of using a DFN modelling approach to assess the connectivity of fracture networks in geothermal systems is best explained through the development of a conceptual model for fluid flow and heat transport in a fractured rock mass. A rock mass is typically comprised of large sections or blocks of intact rock that are bounded by fractures of various orientations and sizes. Depending on the size of the fractures relative to the scale of the problem area, it may be sufficient to model a discontinuous rock mass as a continuum. Figure 2.5 illustrates the idea that the type of model used to represent a discontinuous rock mass is scale dependent.

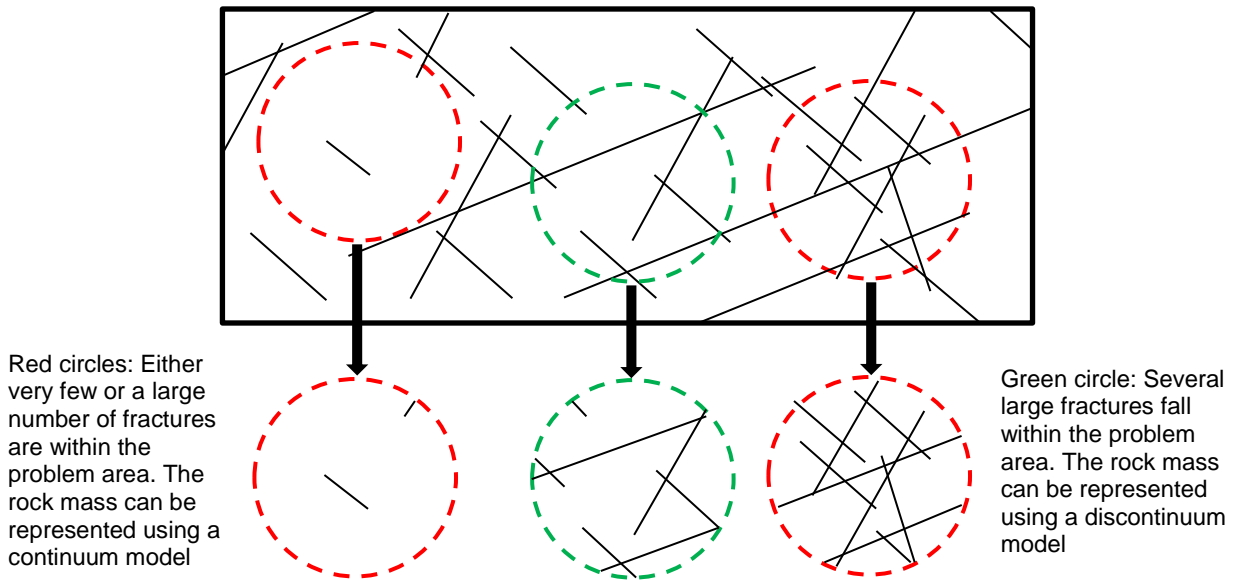


Figure 2.5 A two-dimensional representation of a discontinuous rock mass. The size of the fractures (thin black lines) relative to the problem area (dashed circles) dictates the appropriateness of a continuum vs. discontinuum approach to representing the fractured rock mass

The use of an equivalent continuum modelling approach to represent a geothermal reservoir involves a homogenization process where individual fractures are not explicitly represented. Consequently, the underlying physical processes of localized fluid flow and deformation resulting from or within individual fractures are not represented. If very few fractures exist within the problem area, a continuum modelling approach may be appropriate because fluid flow and heat transfer behaviour will not be influenced by the presence of fractures. A continuum modelling approach may also be appropriate for the representation of heavily fractured geothermal reservoirs. This is because heavily fractured rock masses often behave like an equivalent porous medium.

A discontinuum modelling approach allows for the explicit representation of individual fractures and can be used to simulate fluid flow and transport processes through an interconnected fracture network. Although a discontinuum based model may provide a more intuitive conceptualization of fractured rock masses, its ability to simulate the actual physical nature of a fractured rock system is highly dependent upon accurate characterization of the physical properties and spatial relationship of individual fractures.

2.3.2 The Discrete Fracture Network Modelling Software FracMan

The DFN modelling software FracMan was developed by Golder Associates Inc., and is capable of generating stochastic simulations of fracture networks based on user-defined inputs that are determined through the interpretation and statistical analysis of fracture data. FracMan contains built-in fracture network analysis algorithms, including the determination of overall fracture network connectivity and the number of intersections encountered by simulated well trajectories. Using FracMan, DFN models and fracture connectivity assessments were made of the Meager Creek geothermal site.

2.3.2.1 Fracture Generation Using FracMan

In order to generate DFN models using FracMan, individual fracture sets within the problem area must be identified and characterized. This includes an interpretation of average fracture set orientations, size distributions, and relative fracture intensities. The methodology used to interpret and assign statistical distributions to fracture set properties is described in Chapter 4. All fractures generated using FracMan are represented as planar discs, however the shape of individual fractures can be specified.

Once individual fracture sets have been defined, the method in which the location of individual fractures belonging to each fracture set must be specified. FracMan includes three built-in fracture location algorithms named the Enhanced Baecher, Nearest Neighbour, and Levy Lee models. The Enhanced Baecher model determines the location of individual fractures by distributing fracture centres uniformly in space following a Poisson process. The development of complicated polygonal-shaped fractures is enabled in the Enhanced Baecher model by allowing the user to specify the number of sides belonging to individual fractures, as well as the probability that an individual fracture will terminate when it intersects another fracture.

The Nearest Neighbor model requires that a major structural feature, such as a fault, is explicitly defined in the model. The intensity of fracturing is then set to decrease exponentially with increasing distance away from the major feature. This behaviour can also be simulated using the Enhanced Baecher model by defining regions parallel to major features and manually adjusting the fracture intensity associated within each region. This method provides the user more control over the distribution of fracture locations.

The Levy-Lee Fractal model is used to replicate “self-similar” or “self-affine” fractal patterns. The location of fracture centers are distributed according to a Levy Flight process. According to a Levy Flight process, the distance of adjacent fractures is equal to a certain length which is given by the probability function $P_{L_s}(L' > L_s) = L_s^{-D}$. The

three location algorithms used in FracMan are reviewed in greater detail in Golder Associates Inc. (2011).

2.3.2.2 Generation of DFN Models Using Monte Carlo Simulation

DFN models are stochastic representations of actual fracture networks, and connectivity assessments of multiple DFN simulations will result in non-unique solutions. As such, fracture network connectivity assessments should be made by examining the range of fracture connectivity estimates that result from a sufficiently large number of DFN simulations of a single reservoir. Using FracMan, a probabilistic analysis of fracture network connectivity is facilitated by the inclusion of a built-in pseudo-random Monte Carlo fracture generating algorithm and command-based analysis automation using a native programming language referred to as a macro. Using these tools, programs can be written and read into FracMan, facilitating the generation and analysis of numerous unique DFN simulations.

CHAPTER 3: SITE DESCRIPTION

The Meager Creek geothermal site is located at the base of Meager Mountain, located approximately 65 km northwest of Pemberton, B.C. and 150 km north of Vancouver, B.C., Canada. The following sections provide a description of the geological and structural nature of the Meager Mountain area, as well as a review of historical geothermal exploration activities. The information contained in this chapter is largely taken from past engineering reports completed by Nevin, Sadlier-Brown, Goodbrand Ltd. (NSBG), and a report completed by Lewis and Souther (1978) regarding the geothermal potential of the Meager Mountain area. Information regarding the regional groundwater flow of the Meager Mountain area was taken from Jamieson (1981).

3.1 Regional Geology

The Meager Creek geothermal site is located in rugged terrain, marked by deeply incised valleys and steep relief due to the presence of numerous volcanic peaks. Meager Mountain is part of the Coast mountain range in the Canadian province of Canada, with a total relief greater than 2,300 m (Jamieson and Freeze 1982). The Meager Creek site is located within the Coast Plutonic Complex, near the intersection of the late Tertiary and Quaternary northwesterly-trending Pemberton Belt and the north-south-trending Quaternary volcanoes that are part of the Garibaldi belt. Both the Pemberton and Garibaldi belts are believed to be related to the subduction of the Juan de Fuca Plate (Lewis and Souther 1978).

The portion of the Coast Plutonic Complex surrounding the Meager Creek area consists of discontinuous strips of meta-volcanics and metasediments that trend in a northwest direction, surrounded by granodiorites, diorites, quartz diorites, and associated gneisses (Jamieson 1981). Northwest of Meager Mountain, the quartz monzonite Salal Creek Pluton constitutes the majority of the basement complex.

3.2 Site Geology

The Meager Mountain Volcanic Complex (MMVC) is composed of several dacite and andesite lava domes and associated pyroclastic deposits, located in an area of relatively high relief. The geology of the Meager Creek site is a product of four million years of intermittent volcanic activity, the most recent occurring in 2440 BCE. The initial eruptions of Meager Mountain were likely an explosive discharge of gas-rich magma which led to fracturing of the basement rocks. This led to the deposition of a basal breccia unit followed by dacite flows and up to 500 m of acid tuff. The main mass of the MMVC is composed of porphyritic andesite which consists of flows associated with minor breccia and is cut by comagmatic dykes and plugs. Hypabyssal intrusives and porphyritic dacites comprise the Meager Mountain and Capricorn Mountain, and are limited to the northeast portion of the MMVC.

Unconsolidated glacial deposits fill the bottom of the Meager Creek and Lillooet River valleys. Surficial deposits are comprised of outwash sands and gravels, boulders, and interbedded glaciolacustrine clays, and can reach thicknesses over 100 m in some areas.

3.3 Structural Geology

Small and large scale fractures have been identified and mapped within the MMVC. In general, the type of fractures present within the MMVC are due to one of the following geologic processes (NSBG 1981):

- Tectonic structures related to regional crustal stresses;
- Fractures that develop parallel to foliation in metamorphic rocks or shock fractures related to the intrusion of Tertiary rocks ; and
- Structures related to fracturing and faulting due to volcanism and magmatic body emplacement.

In general, the small scale fractures found within the Meager Creek area are typically the product of tectonic or volcanic processes, whereas fractures are more likely to be oriented parallel to foliation in the areas north of Meager Mountain. Extensive faults and lineaments that fall within the Meager Creek area were identified and measured during a mapping campaign conducted in 1980. Average orientations of these structures are summarized in Table 3.1.

Table 3.1 Average orientations of large scale structures in the South Reservoir

STRIKE (°)	DIP (°)	DDR (°)	STRUCTURE NAME	ASSOCIATED FRACTURE SET
135	60	225	Carbonate Fault Ryan Creek Lineament	Set A
022	87	112	Camp Fault	Set C
152	90	242	Spidery Peak Contact	-
090	50	000	Meager Creek Fault	Set D
007	90	097	No Good Fault	Set C

Modified from NSBG (1981)

The presence of the Meager Creek Fault was found to have a significant impact on fracture connectivity assessments (see section 5.3). The Meager Creek Fault is predominantly comprised of a series of fracture-slip surfaces that dip between 20 – 50° to the north, interspersed with other slippage planes of random orientation (NSBG 1981). Many slip surfaces associated with the Meager Creek fault contain slickensides, and evidence of both compressional and extensional movement has been observed.

3.4 Regional Groundwater Flow

A preliminary regional groundwater study of Meager Mountain and the surrounding area indicate that the regional groundwater flow system is governed by an intermediate water-table position within the mountain mass. The direction of groundwater flow is strongly influenced by the steep topography in that the groundwater system is recharged at higher elevations and discharges in the valley bottoms.

The main source of recharge is from glacial melt water and precipitation during the summer months. The area experiences an average annual precipitation of 1,024 mm,

and it is estimated that approximately 14.5 – 17% of total annual precipitation will enter the groundwater system. However, it was found that the average annual run-off over the drainage basin is greater than 1,880 mm. This indicates that the average annual precipitation at higher elevations may be in excess of 3,000 mm (Jamieson 1981).

Although a few springs are present at higher elevations, the majority of discharge flows through the unconsolidated deposits located in the base of the valleys that confine the Lillooet River and Meager Creek. More than 30 thermal springs with a cumulative discharge of 40 l/s were identified within a 1,200 m² area within 6 km of the confluence of the Lillooet River and Meager Creek. Cold springs found at higher elevations were interpreted to be stratigraphically-controlled by geological contacts between volcanic layers, volcanic-basement rocks, and volcanic-unconsolidated deposit boundaries.

Assuming steady-state conditions, bulk hydraulic conductivity values were estimated to range between 10^{-7} – 10^{-18} m/s for the basement granodiorites. It is expected that hydraulic conductivity values of the permeable fractures within the basement granodiorites are several orders of magnitude greater than the intact matrix.

3.5 Observed Temperature Profiles

All slim holes completed between 1974 and 1982 recorded bottom-hole temperatures at 24-hour intervals for the purpose of delineating the extent and maximum temperature of the geothermal resource at the Meager Creek site. Drillholes M3-75D, M4-75D, M6-79D, and M10-80D intercepted a near-surface thermal anomaly that have inferred

temperature gradients ranging from 225 to $>1000^{\circ}\text{C}/\text{km}$. Due to the observed temperature inversions in the overburden materials, drillholes M1-74D and M8-79D are interpreted to lie on the east and west periphery of the anomaly respectively. The northern boundary is interpreted to lie north of slim hole M6-79D, below Pylon Peak and Devastator Peak. The southern boundary remains unknown (NSBG, 1981), however the observed temperature inversion below the Meager Creek Fault zone intersected in slim hole M09-80D infers that the geothermal reservoir may be confined to the areas north of the Meager Creek Fault.

The maximum temperatures measured by the two deepest slim holes M09-80D and M10-80D were 98.3°C and 162.5°C respectively. Extrapolation of bottom-hole temperature measurements infers that the maximum temperature of the reservoir rocks within 800 m of the surface may be as high as 200°C (NSBG 1980). At greater depths, geothermal fluids encountered in the three deep exploratory wells ranged from 200°C - 210°C in well MC-1 to 270° in well MC-3 (Ghomshei et al. 2004). Detailed geomechanical and temperature profiles for these holes were not available for review. The location of all slim holes and test wells can be seen in appendix A.

3.6 Overview of Historical Field Investigations

In response to the international energy crisis of the 1970's, field investigations were initiated by the British Columbia Hydro and Power Authority (now BC Hydro) and the Canadian Department of Energy, Mines and Petroleum Resources in 1973 to assess the geothermal potential of the Lillooet River region. NSGB was initially contracted by

BC Hydro to complete geologic studies of approximately 3000 square miles extending from the south end of Harrison Lake, northwest to the vicinity of Meager Creek, northeast across Anderson Lake, and southwest towards Alta Lake (NSBG, 1974). Resistivity surveys conducted within the MMVC identified two regions as potential high-temperature geothermal reservoirs. The first region is bounded by three creeks (No Good, Angel, and Meager Creek), on the southern slope of Pylon Peak. The second region is located along the Lillooet River in the area surrounding the Pebble Creek hot springs, northeast of Meager Mountain. The former and latter regions are referred to as the South and North Reservoirs respectively, and are shown in appendix A.

NSBG began field investigations in 1974 in the areas south of Meager Mountain. By 1977, field investigations had extended to the North Reservoir and east of the Lillooet River, which was eventually designated as the Lillooet Valley Resistivity Anomaly (LVRA). The early field investigations included surface mapping, percussion drilling along the banks of Meager Creek, bedrock diamond drilling, geophysical (resistivity, magneto-telluric) and airborne infrared surveys, and geochemistry studies (NSBG, 1978).

Field investigations continued in the North and South Reservoirs until 1982, at which point all field activity was limited to temperature monitoring, chemical analysis of production fluids, and flow testing of the three exploratory wells (B.C. Hydro 1985). All drilling activity was put on hold in 1983 due to financial cut-backs, lack of energy

demand, and declining energy prices (Allen et al. 2000). By the end of 1985, all field investigations at the site were suspended.

A new geothermal lease was granted in 1989 to the Meager Creek Development Corporation, a subsidiary of the Western GeoPower Corporation (Ghomshei et al. 2004). Field investigations recommenced in the early 1990's, and led to the completion of a fourth deep exploratory well (MC-5) in 1995, which was incapable of sustaining steam production (Ghomshei et al. 2004).

In 2002, Western GeoPower Corporation drilled three slim holes (M-17, M-18, and M-19) in the South Reservoir to investigate a high temperature anomaly along the southern slopes of Pylon Peak, immediately north of wells M7-79D and M10-80D. Temperatures as high as 224°C were encountered at depths of 600 m. Significant fracture permeability was reportedly encountered as well (Ghomshei et al. 2004; Ghomshei et al. 2006). These findings led to the completion of three deep production wells (MC-6, MC-7, and MC-8) that were drilled from a common collar location between 2004 and 2005. According to reports, wells MC-6 and MC-8 repeatedly encountered zones that resulted in circulation loss during drilling, and injection test results inferred that the wells intersected highly permeable fractures. MC-7, which was drilled in a northwesterly direction, did not report any circulation loss during drilling (Ghomshei et al. 2006). A deep confirmatory drilling program was scheduled to commence in 2009, but was never initiated. As such, well MC-8 signifies the last geothermal drilling completed in the MMVC (Ghomshei 2010).

Based on the findings of these exploratory field programs, it has been interpreted that two distinct geothermal systems exist in the MMVC, located on the north and south sides of Plinth Peak. It is inferred that both reservoirs exist in the fractured crystalline basement rocks, and that the flow of geothermal fluids is likely controlled by the orientation and connectivity of the existing fracture network. The basement rocks are characterized by low porosity and permeability, although several zones of high permeability have been observed in the drilling logs.

Geomechanical and hydrogeological data collected after 1982 was not publicly available. The extent and detail of the data collected after 1982 is unknown, and could not be incorporated into the DFN model simulations. If the data collected during the drilling program completed by Western GeoPower Corporation between the years 2002 and 2005 becomes publicly available, it would provide much greater insight into the characteristics of the natural fracture network in the South Reservoir. Additional reviews of historical field investigations of the Meager Mountain area can be found in numerous reports completed by NSBG between 1974 and 1982, and by (Jamieson 1981; Ghomshei and Stauder 1989; Ghomshei et al. 2004).

3.6.1 Detailed Summary of Bedrock Drilling between 1974 and 1982

The initial exploratory drilling program was initiated by B.C. Hydro in 1974 and continued until 1982. Prior to 1977, the North and South Reservoirs were only accessible by helicopter. Drilling was typically carried out between late summer and early fall using skid-mounted diamond drill rigs. Several drilling contractors were used

over the course of the program, and coring bit sizes ranged from 27 mm (AQ) to 61 mm (HQ-3). A total of 28 slim holes wells were drilled with depths ranging between 45 to 1,279 m, resulting in approximately 12,573 m of core. Three deep test wells were also completed in the South Reservoir between 1980 and 1982. The final depths of these wells ranged between 3,000 m and 3,500 m. Collar locations for all slim holes and wells drilled between 1974 and 1982 are summarized in Table 3.2, and shown in appendix A.

The first four slim holes (M1-74D, M1-75D, M2-75D, and M3-75D) were completed in the South Reservoir between November 1974 and October 1975, and targeted areas suspected of overlying the greatest thermal anomalies. B.C. Hydro suspended drilling between October 1975 and October 1978 while further geophysical testing was being completed in the South Reservoir and the area surrounding Pebble creek. In 1977, two exploratory holes were drilled by the department of Energy, Mines and Resources of Canada (EMR) as part of the ongoing national geothermal research program. The first (EMR 303-1) was located east of the MMVC, and the second (EMR 301-2) was located half way between Meager Creek and Pemberton, B.C. No down-hole geomechanical or hydrogeological data was available for these two holes.

In 1978, EMR drilled twelve shallow percussion holes (PDH 78-1 through 12) throughout the Lillooet Valley in order to collect near surface temperature gradients and delineate the eastern boundary of the South Reservoir. Only three of these holes reached bedrock, and no fracture information was collected during the program.

B.C. Hydro resumed diamond drilling in the fall of 1978 with the completion of two holes, L1-78D and M5-78D, located in the North and South Reservoirs respectively. L1-78D was drilled on the south side of the Lillooet River, north of Plinth peak. The down-hole temperatures recorded in L1-78D inferred the presence of a geothermal anomaly in the North Reservoir area, and indicated that a tabular heat channel or a fractured hot water aquifer likely exists between 300 and 380 metres depth (NSBG Ltd., 1979). M5-78D was drilled on the bench of Meager Creek valley, west of M3-75D in order to assess the western limit of the South Reservoir. Due to slow penetration rates in the overburden materials, drilling was suspended before reaching bedrock.

Table 3.2 Collar information for all slim holes and wells drilled between 1974 and 1982

	HOLE ID	EASTING (m)	NORTHING (m)	ELEVATION (m)	DEPTH (m)	PLUNGE (°)	TREND (°)	BIT SIZE	YEAR	AREA
SOUTH RESERVOIR	EMR 301-1	467 160	5 602 540	587	45	-70	000	BQ	1974	Meager Creek hot springs
	EMR 301-2	467 200	5 602 640	583	118	-90	000	BQ	1974	Meager Creek hot springs
	M1-74D	466 351	5 601 659	635	347	-90	000	AQ	1974	S. Reservoir Outflow Plume
	M2-75D	465 351	5 601 829	774	91	-90	000	AQ	1975	South Reservoir
	M3-75D	464 016	5 601 399	770	87	-90	000	AQ	1975	South Reservoir
	M4-75D	463 601	5 601 989	808	60	-70	356	AQ	1975	South Reservoir
	M5-78D	463 161	5 601 529	822	250	-90	000	-	1978	South Reservoir, SW area
	M6-79D	464 281	5 602 499	884	321	-90	000	HQ	1979	South Reservoir, east of Angel Creek
	M7-79D	463 061	5 602 069	899	367	-90	000	HQ	1979	South Reservoir, east of No Good Creek
	M8-79D	461 631	5 602 089	875	497	-90	000	HQ	1979	South Reservoir, West of No Good Creek
	M9-80D	463 981	5 601 324	765	1142	-90 to -65	051	HQ/NQ	1980	South Reservoir, 100m south of M3-75D
	M10-80D	463 701	5 601 994	807.5	1070	-90 to -60	055	HQ/NQ	1980	South Reservoir, at the break-in slope on the north side of Meager Creek
	M11-80D	465 621	5 601 909	791	559	-90	000	HQ/NQ	1980	South Reservoir, approx. 450m east of M2-75D
	M12-80D	465 901	5 599 204	792.5	605	-90	000	HQ/NQ	1980	South Fork Drainage
	M13-81D	462 476	5 602 014	899	600	-90	000	HQ/NQ	1981	South Reservoir, west of No Good Creek
	M14-81D	467 061	5 600 771	861	579	-78	000	HQ/NQ	1981	South Fork
MC-1	463 671	5 601 949	817	3040	-90	000	-	1981	South Reservoir	
MC-2	463 701	5 601 949	817	3503	-90	000	-	1982	South Reservoir	
MC-3	463 748	5 601 949	817	3503	-90	000	-	1982	South Reservoir	
NORTH RESERVOIR	EMR 303-1	471 970	5 608 510	580	213	-90	000	-	1977	Lillooet Valley
	L1-78D	463 091	5 614 849	760	603	-90	000	HQ/NQ	1978	North Lillooet Valley
	L2-80D	461 241	5 613 602	896	595	-90	000	NQ	1980	North Reservoir, Job Creek
	L3-80D	462 393	5 613 854	972	1010	-86	033	HQ/NQ/BQ	1980	North Reservoir, North flank of Plinth Peak, 1.3 km east of Job Creek
	L4-81D	461 646	5 612 249	1097	1279	-80	340	HQ/NQ	1981	North Reservoir, east bank of Job Creek
	L5-81D	465 661	5 613 874	774	660	-80	340	HQ/NQ	1981	North Reservoir, immediately west of the recent Fall Creek volcanic flows
	L6-81D	470 496	5 608 439	535	579	-90	000	HQ/NQ	1981	Lillooet Valley, 2km upstream from the confluence of Meager Creek and the Lillooet River
	L7-82D	460 326	5 610 699	1808	421	-90	000	NQ	1982	North Reservoir, headwaters of the eastern tributary of Affliction Creek
L8-82D	459 746	5 613 454	960	476	-90	000	NQ	1982	North Reservoir, west bank of lower Affliction Creek	

In 1979, three more slim holes were drilled in the South Reservoir (M6, M7, and M8-79D). These holes were drilled using standard HQ-3 diamond drill bits. Retrieved core samples were logged for lithology, core recovery, rock competency (RQD), alteration, and fracture infill material. The structural information collected from these holes marks the first attempt to characterize the fracture characteristics of the basement rocks. Due to the high bottom-hole temperatures measured in hole M7-79D (>200° C), flow testing was completed in an attempt to induce continuous steam production. Two methods used to induce steam production included air-lifting of the upper water column and overpressuring of the hole followed by rapid depressurization. Both methods were capable of stimulating steam production at surface. However, production could not be sustained. It was suggested that the lack of continuous steam production may be due to insufficient recharge of superheated water at depth, or quenching by cooler near-surface water flowing down the well bore (NSBG, 1981). Packer testing of the bottom portion of the hole was not attempted, thus neither of these proposed mechanisms were verified. Nevertheless, the short-term production of steam marked the first geothermal steam produced in Canada (NSBG, 1981).

Between 1980 and 1982, thirteen more slim holes were drilled (six in each of the North and South Reservoirs, and one in the LVRA) before the initial drilling program was ended. Hole depths ranged from 535 m to 1,808 m and were drilled using both HQ-3 and NQ diamond drill bits. The structural information obtained from core samples was identical to that collected during the 1979 drilling program. A series of pilot geophysical surveys were completed on a 300 m section of well M9-80D to assess the applicability

of exploration techniques used in the oil and gas industry, and to correlate the results of the surveys to geological features observed in the core. The surveys were capable of identifying the location of highly fractured zones that were also identified in the drilling logs; however they did not provide any information regarding the geometry, orientation, or flow characteristics of these fracture zones.

The completion of three deep test wells (MC-1, MC-2, and MC-3) between 1980 and 1982 marked the end of the initial drilling program. The purpose of these test wells was to further assess the production potential of the South Reservoir. The holes were primarily drilled using a diamond rotary drill bit, and no acoustic or optical televiewer surveys were conducted. Consequently, no quantitative fracture information was collected from these wells. MC-1 was capable of sustaining two-phase fluid production (Stauder and Hunt 1987), whereas MC-2 and MC-3 were incapable of producing any geothermal fluid at surface. It was interpreted that well MC-3 intersected the No-Good Fault zone at a depth of 3,025 metres, which resulted in a loss of drilling fluid circulation. Unfortunately, this fracture zone was plugged with drilling mud prior to well testing. It was later determined that none of the three wells were suitable for commercial production, however there may exist a well-connected, permeable fracture network associated with the No-Good Fault zone (Ghomshei et al. 2004; Nevin 1992).

3.6.2 Summary of Structural Mapping Programs

Three structural mapping programs were completed in the MMVC in 1980, 1981, and 2013, and extended to the South and North Reservoir areas. All mapping station

locations are shown in appendix A. These mapping programs are summarized in the following sub-sections.

3.6.2.1 1980 Structural Mapping Program

In 1980, NSBG Ltd. completed extensive geological and structural mapping throughout the Meager Valley. The three main objectives of the mapping program were to:

- 1) extend the surficial geology map completed by (Read 1979) to higher elevations, north of Meager Creek;
- 2) determine predominant fracture orientations by mapping surface exposures of the basement granodiorites; and
- 3) identify and characterize regional structures (e.g. faults and lineaments) within the South reservoir that may influence the connectivity and permeability of the existing fracture network.

A total of twenty five bedrock outcrops along the north and south sides of Meager Creek were mapped. All of the bedrock outcrops were composed of quartz diorite with the exception of mapping station 12, which was composed of andesite. A total of 4,033 individual fractures were mapped, all of which were identified as joints. The location and number of fractures mapped at each station are summarized in appendix D.1. For each mapping station, peak orientations (dip/dip direction) of predominant joint sets were determined using contoured lower hemisphere equal area stereonet. These stereonet were initially published in Jamieson (1981), and copies are included in appendix C, and could not be re-created because the original mapping sheets were unavailable.

Jamieson (1981) identified four reoccurring joint set orientations that were observed across several mapping stations. A range of values for dip and dip direction for the four major joint sets were reported for each mapping station. Descriptions of these joint sets are summarized as follows:

Joint Set 1: Joint set 1 is observed in almost all of the 25 mapping stations, and dips steeply towards the northwest/southeast. Joint set 1 shares a similar orientation to the Camp Fault.

Joint Set 2: Joint set 2 is present in most of the 25 mapping stations, and dips moderately/steeply towards the southwest. Regional structures that have similar orientations to joint set 2 are the Carbonate Fault and Ryan Creek Lineament.

Joint Set 3: Joint set 3 is only observed in the area bounded by No Good, Angel, and Meager Creek. Joint set 3 dips steeply towards the south, and does not appear to be related to any of the regional structures mapped in the South Reservoir.

Joint Set 4: Joint set 4 is primarily confined to the same area as joint set 3, and has a shallow to moderate dip towards the north. Joint set 4 appears to be related to the Meager Creek Fault.

It was noted that Jamieson (1981) determined peak joint set orientations by averaging maximum and minimum dip and dip direction values observed within a cluster of poles. Peak orientations were adjusted by plotting poles on the original stereonet based on the location of the highest observed pole concentrations. A total of 101 peaks were identified over the 25 mapping stations compared to 50 peaks that were originally selected by Jamieson. Weightings were assigned to each peak based on the total number of fractures plotted on the stereonet, and the percent-concentration of each peak.

The 1980 mapping program also collected measurements of true spacing and aperture for 23 separate joint sets. Estimates of spacing and aperture ranged from 0.05 to 5.0 m and from tight to 20 mm respectively. It was noted that true spacing and aperture were not directly measured, rather they were estimated based on visual inspection (Jamieson 1981).

3.6.2.2 1981 Structural Mapping Program

During the summer of 1981, BC Hydro completed extensive structural mapping throughout the MMVC in order to augment the structural database in the South Reservoir and to begin characterizing the orientation of fractures in the major rock units located north and northeast of Meager Mountain. The structural information collected during the 1981 mapping program was more comprehensive than the 1980 program. The type of fracture information recorded included rock type, orientation, fracture type, trace length, aperture, true spacing, regularity, waviness, roughness, alteration type,

and alteration intensity (B.C. Hydro 1982). A total of 98 locations were mapped, resulting in 1645 individual fracture measurements. After applying validity criteria to all of the fracture measurements, only 96 locations provided valid fracture data, with a total of 1615 fracture measurements. The location and number of validated fractures mapped at each station are summarized in appendix D.2.

3.6.2.3 2013 Structural Mapping Program

In the summer of 2013, the author completed structural mapping of four bedrock outcrops within the North Reservoir, northeast of the Lillooet River. The purpose of the mapping was to increase the number of reliable measurements of true spacing, trace length, and aperture in the fracture database. Geotechnical line mapping was completed on four bedrock outcrops, resulting in 57 individual fracture measurements. The location and number of fractures mapped at each mapping station are summarized in appendix D.3.

CHAPTER 4: INTERPRETATION OF FRACTURE DATA

This chapter begins with a summary of the geological information that was used to characterize the physical properties of the natural fracture network in the basement granodiorites within the South Reservoir. All geological information that was used for the development of DFN models was compiled, digitized, and reviewed in order to exclude erroneous or low-confidence data from subsequent analyses. The primary source of structural and hydrogeological data is from annual engineering reports that documented the findings from exploratory slim hole drilling and structural mapping programs conducted between 1974 and 1982 in the areas surrounding Meager Mountain. A summary of the bedrock drilling and structural mapping programs are provided in sections 3.6.1 and 3.6.2 respectively. The methods used to derive stochastically representative fracture properties for individual fracture sets and the uncertainty associated with the derived fracture properties are presented and discussed.

4.1 Data Collected from Bedrock Drilling

Between 1974 and 1982, a substantial amount of geological data was collected from the analysis of core samples and records of drilling conditions. The geological data that was available for the analysis of the fracture characteristics of the basement granodiorites included:

- Descriptive lithology and alteration logs;
- Core recovery;
- Rock quality designation (RQD);
- Fracture frequency;

- Depths at which fluid circulation was lost during drilling; and
- Depths of dykes, shears, and fault zones;

The quality, quantity, and type of geological data collected from each drill hole varied over the duration of the exploratory drilling program. Until 1979, only qualitative descriptions and assessments of drilling conditions, temperature gradient measurements, fracture characteristics, and water table elevations were recorded. After 1979, estimates of fracture frequency and rock competency (RQD) were also recorded. The following sections describe the data collected and how the data was incorporated into subsequent DFN model simulations.

4.1.1 Lithology and Alteration Logs

Detailed lithology was logged for all slim holes. To facilitate the structural and statistical analyses, simplified rock types were established so that structurally similar rock types could be grouped together (e.g. fine grained and medium grained quartz diorites were grouped together as quartz diorites). Table 4.1 lists all of the rock types encountered in the South Reservoir during the 1974 – 1982 slim hole drilling program. The basement rocks consist primarily of quartz diorite and gneiss, and to a lesser degree metavolcanics and amphibolites. The rock types encountered at depths below 400 m elevation were almost entirely quartz diorite.

Table 4.1 Rock types encountered during the 1974 - 1982 slim hole drilling program

ALL RECORDED ROCK TYPES		SIMPLIFIED ROCK TYPES	
Code	Description	Code	Description
AM	Amphibolite	AM	Amphibolite
AN	Andesite	AN	Andesite
DA	Dacite	DA	Dacite
DI, DIO	Diorite		Rhyodacite
FP	Feldspar Porphyry	FP	Feldspar Porphyry
GN	Gneiss	GN	Gneiss
GRN	Greenstone	GRN	Greenstone
HNFS	Hornfels	HNFS	Hornfels
MV	Metavolcanics	MV	Metavolcanics
QM	Quartz Monzonite	QZDI	Quartz Diorite
QZDI	Quartz Diorite		Quartz Monzonite
QZTE	Quartzite		Quartzite
RYDA	Rhyodacite		Diorite

Observed alteration minerals and qualitative assessments of the degree of alteration were recorded. Occasionally the depths of altered fault zones, shear zones, veins and dykes were also recorded. Alteration zones identified as possible conduits for fluid flow were recorded in the graphical logs located in appendix B.

The alteration logs may be used to assess the continuity of altered fractures across holes. Mineralization and alteration can be indicative of the geological processes that lead to the development of fractures, and could be used to define fracture sets (Cohen 1995). This type of analysis is beyond the scope of this study given that the amount of subsurface fracture data available for the analysis was limited. No core photos or core samples were available.

4.1.2 Core Recovery

Core recovery is a measure of the total length of core retrieved from a single drill run. Core recovery is often reported as a percentage, calculated as the total length of core retrieved divided by the actual length of the core run. Core recovery is typically lower in soft or heavily fractured rock, and greater in competent rock. Plots of core recovery versus depth are included in the graphical logs found in appendix B, which provide rough indications of the overall quality of the basement rocks at depth.

4.1.3 Rock Quality Designation

The Rock Quality Designation (RQD) is a measure of rock competency, and is defined as the sum of intact pieces of core with a length greater than 0.1 m, divided by the total length of core. The cut-off length of 0.1 m is referred to as the RQD threshold value (Priest 1993). In the case of rock cores obtained from drilling, RQD for the entire drill run can be calculated using the following equation defined by Deere (1964):

$$RQD = 100\% \frac{\sum x_i}{L} \quad \text{Equation 4.1}$$

where

X_i = Lengths of individual pieces of core > 0.1 m

L = Total length of the drill run

At the Meager Creek site, RQD was recorded for all slim holes completed in bedrock after 1978, totalling approximately 6,049 m worth of core. Figure 4.1 is a plot of depth-averaged RQD versus elevation for all slim holes completed in the South Reservoir.

Depth-averaged RQD values were calculated at 50 m intervals by averaging RQD values for drill runs located within ± 50 m elevation, weighted by run length.

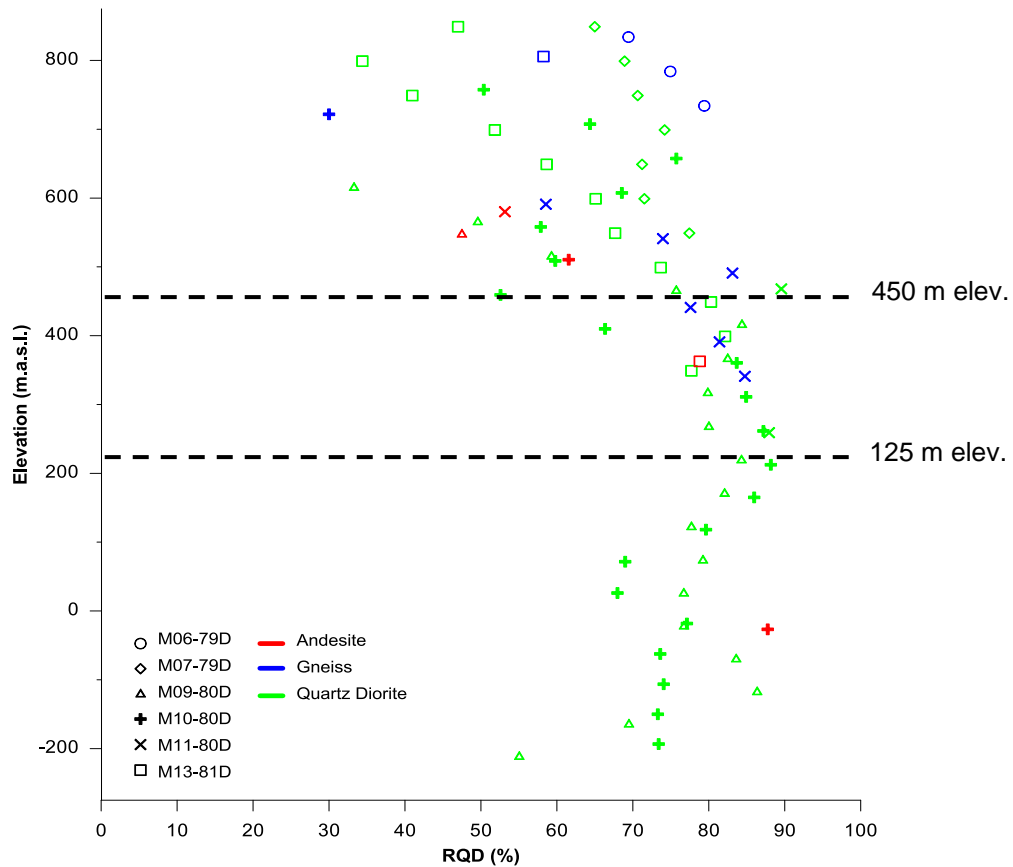


Figure 4.1 Depth-averaged RQD versus elevation at the Meager Creek site

From Figure 4.1, it can be seen that rock competency increases with depth up until approximately 125 m elevation, where it reaches a maximum depth-averaged RQD of 88.2%. Below 125 m elevation, depth-averaged RQD values decrease slightly indicating a decrease in rock competency at greater depth. It was noted that only slim holes M09-80D and M10-80D extend below 125 m elevation. From the drilling reports for these two slim holes, the following description of rock competency was recorded (NSBG 1982):

“Below 600 metres [depth]... the core becomes considerably more uniform in terms of both hydrothermal alteration and structure with the exception of several distinctive intervals of closely-spaced clean fractures at right angles to the core axis. This phenomenon, known as discing, is a result of stress relief upon coring.”

The definition of RQD ignores the presence of mechanical fractures in the summation of intact pieces of core greater than the RQD threshold value. This is to ensure that rock competency is only assessed based on the pre-existing fractures within the rock mass. Upon review of the drilling logs where intervals of “discing” was recorded, it is apparent that these mechanical fractures were included in the calculation of RQD, thus providing a false indication of decreasing rock competency with depth. Consequently, a low degree of confidence is attributed to the accuracy of RQD measurements.

The methodology used to calculate RQD from the core samples will tend to underestimate the competency of the rock mass. The consequence of this error is that it leads to a non-conservative assessment of the number of existing natural fractures.

4.1.4 Fracture Frequency

Fracture frequency is the average number of natural fractures that are encountered per metre of core/scanline (see linear fracture intensity measurement P10, described in section 2.2.2.3). Upon review of the drilling logs available for the South Reservoir, it was

found that fracture frequency was recorded inconsistently and included both quantitative and qualitative estimates. Qualitative assessments of fracture frequency consisted of ratings of low, moderate or highly fractured intervals. In an annual report by NSBG, it was specified that a fracture frequency rating of “low” indicates that there are less than five fractures per metre, “moderate” is between five and fifteen fractures per metre, and “high” is greater than 15 fractures per metre (NSBG 1982). Table 4.2 summarizes the assumed fracture frequencies based on these definitions. Plots of fracture frequency as a function of depth can be seen in the geomechanical logs included in appendix B.

Table 4.2 Qualitative and quantitative descriptions of fracture frequency

FRACTURE FREQUENCY (#/m)	QUALITATIVE DESCRIPTION USED IN DRILLING LOGS
2.5	Low fracture density
10	Moderate fracture density
15	High fracture density
5	Low to Moderate fracture density
12.5	Moderate to High fracture density

An estimate of fracture intensity at depth is required to generate stochastically representative DFN models. Given the inconsistent nature of the available fracture frequency measurements, logged RQD was used to derive fracture frequency estimates. Priest and Hudson (1976) demonstrated that a theoretical RQD value, $TRQD_t$, can be calculated through integration of the spacing probability density distribution function that is statistically representative of a sample of fracture spacing measurements. If it is assumed that the distribution of fractures within a rock mass follows a Poisson process, it has been shown that the probability density distribution of

fracture spacing along a scanline will have a negative exponential form. Priest (1993) showed that if spacing along a scanline follows a negative exponential distribution, the mean fracture frequency, λ , is related to $TRQD_t$ by the following equation:

$$TRQD_t = 100[e^{-\lambda t}(1 + \lambda t) - e^{-\lambda t}(1 + \lambda t)] \quad \text{Equation 4.2}$$

where

$TRQD_t$ = Theoretical RQD for a general threshold value, t (%)

t = TRQD threshold value (m)

λ = Mean fracture frequency (#/m)

In section 4.2.3 it is shown that spacing measurements collected from surface mapping within the MMVC follow a negative exponential distribution. Using the depth-averaged RQD values shown in Figure 4.1, estimates of mean fracture frequency with depth were calculated by iteratively solving equation 4.2. It can be seen from Figure 4.2 that fracture frequency decreases with depth as rock competency increases, and ranged between 6 and 11 fractures per metre below 450 m elevation.

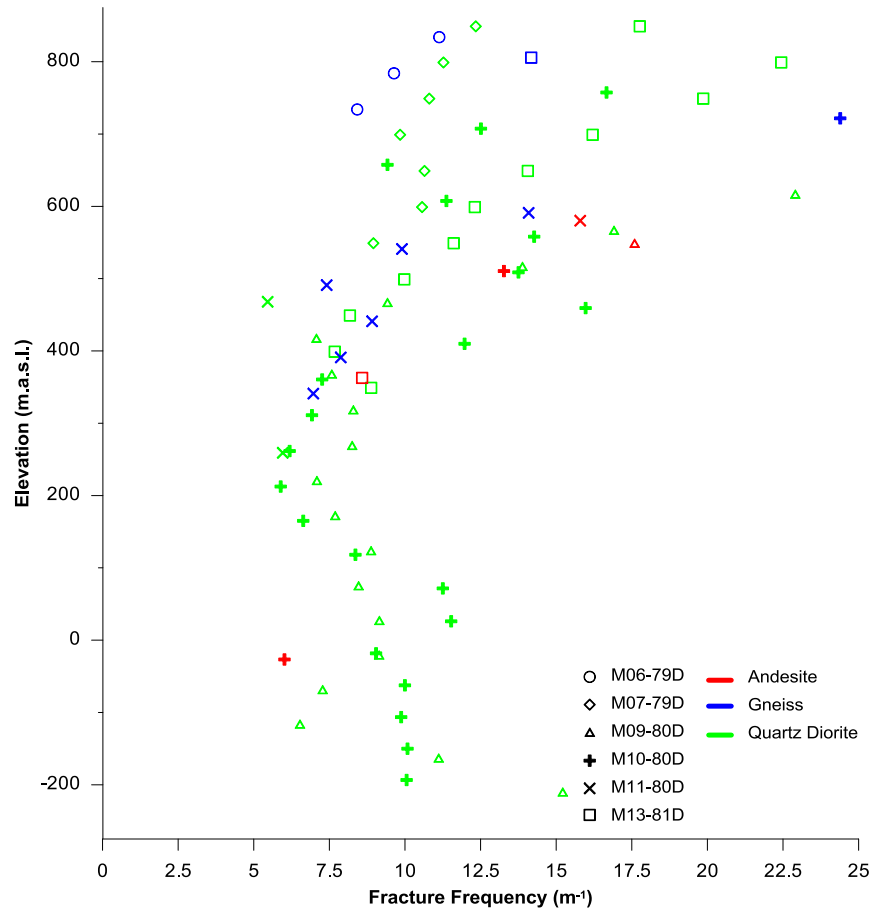


Figure 4.2 Fracture frequency calculated from depth-averaged RQD versus elevation at the Meager Creek site

It is important to note that the values of fracture frequency derived from equation 4.2 are sensitive to the TRQD threshold value, which is equal to 0.1 m for all the RQD measurements taken within the South Reservoir. At lower threshold values, TRQD becomes insensitive to large mean fracture spacings. Figure 4.3 shows that for a TRQD threshold level of 0.1 m, TRQD is insensitive to mean spacings greater than 0.3 m, which is equal to a mean fracture frequency of approximately 3.3 m^{-1} (Priest and Hudson 1976). Consequently, the values of fracture frequency plotted in Figure 4.2 will

likely be overestimated at lower elevations where depth-averaged values of RQD tend to be higher and the rock mass is more competent.

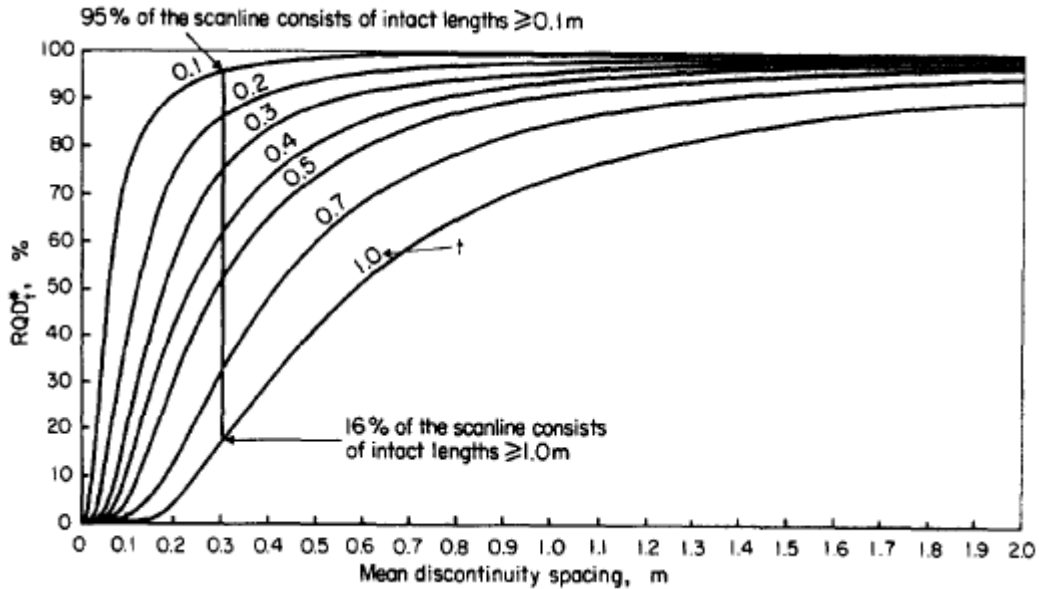


Figure 4.3 Sensitivity of TRQD_t to a range of TRQD_t threshold values, from Priest and Hudson (1976)

After review of the NSBG reports, it is unclear if any attempt was made to discern natural fractures from mechanical fractures that were induced due to drilling-related stresses. If both natural and mechanical fractures were included in the determination of fracture frequency and RQD, this will lead to an overestimation of the true fracture frequency. Several slim holes were drilled using small diameter drill bits (NQ and AQ), and there is no indication that coring was completed using a triple-tube wire line system. Consequently, RQD and fracture frequency measurements obtained from holes drilled using an AQ coring bit were not included in the analyses.

4.1.5 Drilling Conditions Logs

Drill operators maintained logs of difficult ground conditions that were encountered during the slim hole drilling program. The information recorded in these logs included the depths of soft/blocky zones and areas where drilling fluid circulation was substantially reduced or lost. It was observed that reported depths of blocky zones often coincided with highly fractured/shear zones, lithological contacts, or intrusive dykes.

Zones of lost fluid circulation were typically encountered within the first 300 m of a hole and were rarely encountered below 450 m elevation. Within the first 300 m of most slim holes, the basement granodiorites were typically less competent. Of the slim holes completed within the South Reservoir, both M09-80D and M10-80D encountered zones of lost circulation that are of particular interest. M09-80D encountered multiple zones of lost circulation between 175 – 250 m depth (roughly between 525 – 600 m elevation). This zone coincides with the point of intersection between the M09-80D and the projected depth of the Meager Creek Fault. No other zones of lost circulation were recorded above or below this zone. This implies that portions of the Meager Creek Fault zone likely have significantly higher permeability relative to the basement rocks that constitute the hanging wall and footwall of the fault. M10-80D encountered zones of lost circulation between 350 – 400 m depth (roughly between 400 – 450 m elevation). Within this interval, several andesite dykes were also intersected, and are suspected to be responsible for the loss of drilling fluid circulation (NSBG 1982). The role of andesite dykes and their potential effect on the flow properties of the South Reservoir are discussed in section 4.1.6. Another possible explanation for these lost circulation zones

is the presence of a fault damage zone related to the Meager Creek Fault. This theory is discussed in detail in section 5.3.2.2.

There were many instances where fracture zones and dykes intersected during drilling were not accompanied by the loss of drilling fluids. The relatively poor correlation between fracture frequency and loss of drilling circulation shows that the presence of highly fractured zones does not infer that the zone is highly permeable. This observation has been confirmed by other investigations of fluid flow in fractured rock masses. Testing at the Raymond field site in California demonstrated that the location of permeable fractures were not correlated to the location of heavily fractured zones, and that fluid flow was confined to a very small percentage of fractures observed in test wells (Cohen 1995).

During prefeasibility-level exploration, monitoring of fluid circulation during drilling should be a priority for all geothermal projects because they provide insight into the distribution of permeable fractures with depth at no additional cost. Identification of permeable fractures is essential to modelling the flow of a geothermal reservoir, and provides greater insight into the hydraulic properties of connected fracture networks. Although many fractures and fracture zones may be encountered during drilling, fluid flow is typically dominated by a few permeable fractures. Methods for identifying highly conductive zones in boreholes are described in section 6.5.1.

4.1.6 Volcanic Dykes

Slim holes completed in the South Reservoir sporadically intersected andesite dykes over a wide range of elevations. Many of these dykes are characterized by highly fractured/brecciated contact margins with the basement granodiorites. Given that the basement granodiorites are typically competent and are relatively impermeable, these volcanic dykes may act as extensive preferential pathways for fluid flow. In a study by Cohen (1995), it was found that the flow and transport behaviour of a fractured rock mass at the Raymond test site was heavily influenced by fractured pegmatite dykes.

No information was available to assess the orientation or extent of the andesite dykes within the South Reservoir. Consequently, these features could not be incorporated into the DFN model. It is possible that the andesite dykes act as preferential pathways for fluid circulation, and future subsurface investigations should focus on determining if these features have a preferred orientation and if the extent of these features can be measured.

4.2 Fracture Data Collected from Surface Mapping

Surface mapping campaigns completed in 1980, 1981, and 2013 were the primary sources of fracture data that facilitated the characterization of individual fractures and major fracture sets. The type and quality of fracture data collected during each mapping campaign was inconsistent. Information that was consistently recorded included orientation (dip and dip direction) measurements for individual fractures, mapping station coordinates, and fracture type. Fractures that did not show any signs of

movement were labelled as joints. Small and large fractures that showed signs of past movement were labelled as shears and faults respectively. Spacing and aperture measurements recorded during the 1980 mapping campaign were estimated instead of directly measured (Jamieson 1981). All individual fracture measurements were reviewed and compiled into a single fracture database, and data that appeared suspicious or erroneous were excluded.

Fracture orientation measurements were used to delineate structural domain boundaries and determine the distribution of major fracture sets and peak orientations. The distribution of fracture spacing and trace length measurements were analysed in order to interpret the fracture intensity and fracture size distribution within the South Reservoir. Distributions of fracture aperture were not determined for individual fractures due to the fact that the majority of available aperture measurements were estimated and not measured directly, and the overall number of aperture estimates was extremely limited. The true shape of fractures within the South Reservoir is unknown, and it was assumed that individual fractures can be represented as planar polygons.

4.2.1 Delineation of Structural Domains

Structural domains are three-dimensional zones within a rock mass over which distinct fracture sets can be observed, and the distribution of geologic properties is statistically homogenous. The delineation of structural domains and identification of representative fracture sets within these structural domains was achieved through iterative spatial and structural analyses of fracture data collected from surface mapping, and required the

interpretation of geological factors including prevalent rock types, regional faults, and the orientation and type of individual fractures.

Fracture data was analysed separately based on one of three major rock types: quartz diorite, gneiss, and metavolcanics. Fracture measurements from all other rock types were not included in the structural analysis as they are not expected to comprise a significant portion of the geothermal reservoir. A comparison of peak orientations indicated that the structural behaviour of fractures is inconsistent across the three major rock types comprising the basement rocks that host the geothermal anomaly. Therefore, fracture properties such as spacing and trace length are also assumed to vary based on rock type.

The majority of surface mapping within the South Reservoir falls between the area east of No Good Creek, west of Canyon Creek, and north of Meager Creek (see appendix A). Within this area, the following topographical features and regional faults were analyzed to see if they serve as structural domain boundaries:

- Meager Creek Fault (southern boundary);
- No Good Discontinuity (western boundary);
- Camp Fault (eastern boundary); and
- The transition between the south and south eastern slope of Pylon Peak.

The extent and location of these faults on surface were originally interpreted by Read (1979), and were updated using mapping data collected during the 1980 structural

mapping campaign (NSBG 1982). The suitability of surface features and regional faults as structural domain boundaries was assessed by plotting poles of individual fractures on contoured lower hemisphere equal area stereonet for individual mapping stations, and comparing peak orientations of observed fracture sets. Stereonet plots were created using the graphical software program Dips V6.0 by Rocscience. Regional faults were interpreted as structural domain boundaries if peak orientations of fracture sets were observed to change on either side of the fault. Five structural domains were identified at the Meager Creek site, and are shown in Figure 4.4. Stereonets for each of the structural domains are located in appendix C.

A comparison of observed fracture set orientations for each of the structural domains indicate that the No Good Creek and Meager Creek Faults act as structural domain boundaries, and represent the western and southern extent of the South Reservoir respectively. Conversely, a comparison of stereonet from mapping stations located on the east and west sides of the Camp Fault did not show significant changes in fracture set orientations, implying that the Camp Fault does not act as a structural domain boundary. Consequently, fracture data collected within the South Reservoir and East of Camp Fault domains were used to delineate the fracture characteristics of the South Reservoir.

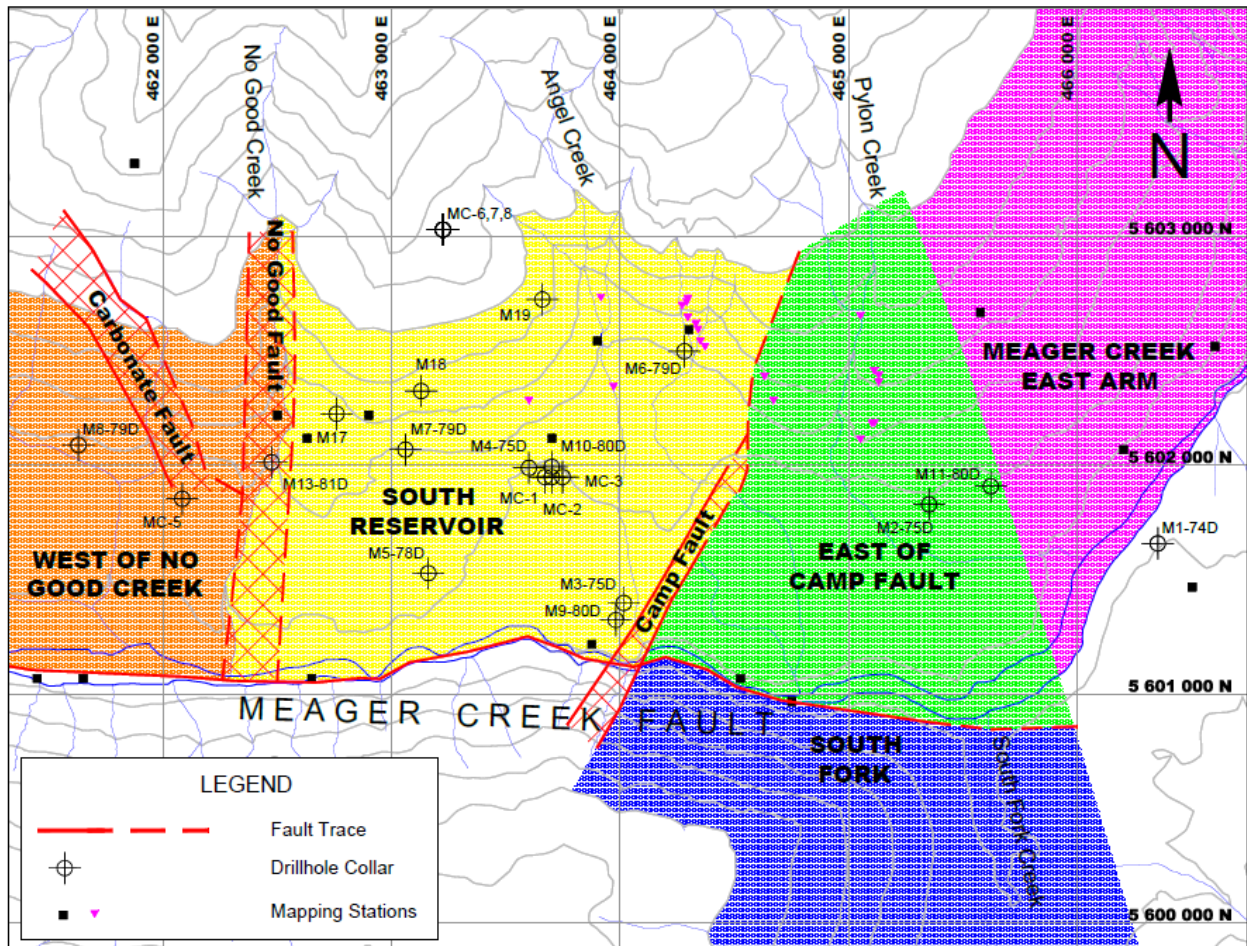


Figure 4.4 Structural domains identified within the South Reservoir

The structural domain boundary which separates the East of Camp Fault and Meager Creek East Arm structural domains coincides with a change in orientation of the base of the slope of Pylon Peak. Within the Meager Creek East Arm structural domain, there are relatively few mapping stations, the location of mapping stations is distributed over a large area, and consistent peak orientations were not observed. As such, fracture data collected within the structural domain was not used to delineate the fracture characteristics of the South Reservoir.

The North Reservoir structural domain encompasses all of the mapping stations that were mapped during the 2013 structural mapping campaign, and is not shown in Figure 4.4. It was observed that the fracture set orientations within North Reservoir, South Reservoir, and East of Camp Fault structural domains are similar. As such, fracture data from the North Reservoir, South Reservoir and East of Camp Fault structural domains were combined in order to augment the amount of fracture data available for the creation of the South Reservoir DFN model. This was necessary due to the limited amount of fracture spacing and trace length measurements collected within the South Reservoir and East of Camp Fault structural domains during the 1980 and 1981 mapping campaigns.

4.2.2 Peak Orientation and Distribution Parameters for Major Fracture Sets

The orientation and range of dip and dip direction of major fracture sets within the South Reservoir were determined by assessing the peak orientations of major fracture sets using stereonet plots of individual mapping stations located in the North Reservoir, South Reservoir, and East of Camp Fault structural domains. All fractures mapped from quartz diorite outcrops within these three structural domains are collectively plotted on a single stereonet in Figure 4.5. Seven major fracture sets were identified, labelled Fracture Sets A – G. Table 4.3 lists all of the major fracture sets within the South Reservoir and summarizes the average peak orientations for each set.

The distribution of fracture orientations for each fracture set listed in Table 4.3 was assessed using a Fisher distribution analysis. A Fisher distribution assumes that all

observed fracture orientations within a fracture set are scattered around a single true orientation. According to a Fisher distribution, it is assumed that the probability of a randomly selected orientation taken from a sample of orientation measurements centered around a single true orientation makes an angle between θ and $\theta + d\theta$ with the true orientation. This can be expressed using the following equation (Priest 1993):

$$P(\theta) = \eta e^{k \cos \theta} d\theta \quad \text{Equation 4.3}$$

where

$$\eta = \frac{k * \sin \theta}{e^k - e^{-k}}$$

$k = \text{Fisher constant}$

The parameter k in equation 4.3 is often referred to as the Fisher constant, and is a measure of the degree of clustering for a given population of orientation measurements. The Fisher constant can be determined by iteratively solving the following equation (Priest 1993):

$$\frac{e^k + e^{-k}}{e^k - e^{-k}} - \frac{1}{k} = \frac{|r_n|}{M} \quad \text{Equation 4.4}$$

where

$k = \text{Fisher constant}$

$|r_n| = \text{magnitude of the resultant vector for a sample of orientation measurements}$

$M = \text{number of orientation measurements in a sample}$

Values of $|r_n|$ and M were calculated for fracture sets A – G using all of the poles located within the range of dip and dip direction values shown in Figure 4.5. Using a mathematical solver, equation 4.4 was solved iteratively in order to determine the Fisher

constants for each fracture set, and used as inputs in the DFN simulations. Fisher constants for each fracture set are summarized in Table 4.3.

Table 4.3 Summary of peak orientations for major fracture sets based on surface mapping data from the North Reservoir, South Reservoir, and East of Camp Fault structural domains

MAJOR SETS	AVERAGE				DIP RANGE		DDR RANGE		FISHER CONSTANT (k)
	PEAK AVERAGE ¹		BOX AVERAGE ²		Min (°)	Max (°)	Min (°)	Max (°)	
	Dip (°)	DDR (°)	Dip (°)	DDR (°)					
SET A	60	223	60	228	40	80	200	260	29.6
SET B	30	257	28	271	15	40	240	315	47.7
SET C	89	118	87	111	80	90	090	130	48.7
					80	90	270	310	
SET D	77	172	83	174	75	90	330	020	41.5
					75	90	150	200	
SET E	31	350	33	358	25	50	330	020	111.0
SET F	66	109	69	099	60	80	075	120	40
SET G	44	124	43	130	30	50	115	180	42.2

1. The peak average orientation for each major set is equal to the dip/dip direction of the centre of the highest observed contour level.
2. The box average orientation for each major set is calculated by averaging the dip/dip direction for all poles within the range of dip/dip direction ranges.

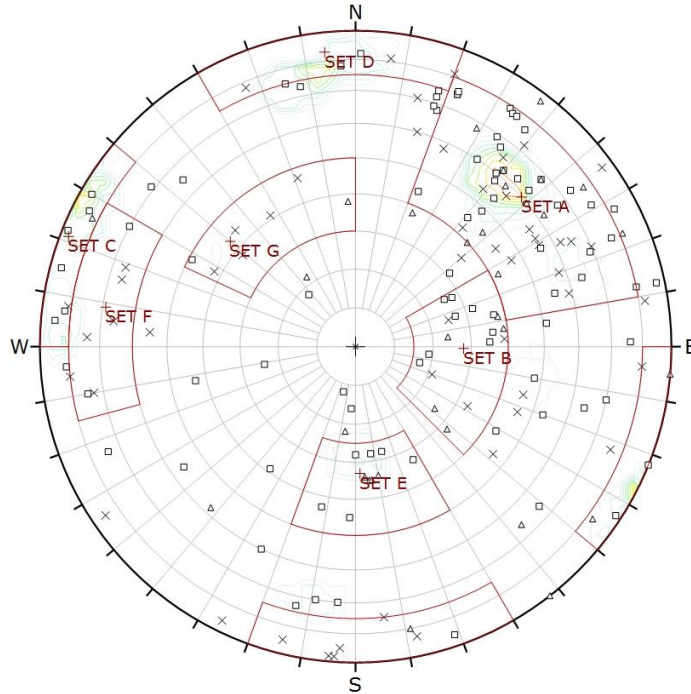


Figure 4.5 Combined lower hemisphere equal area stereonet plot of all fracture data collected from surface outcrops of quartz diorite in the North Reservoir, South Reservoir, and East of Camp Fault structural domains

4.2.3 Analysis of Fracture Spacing

The 1980 and 2013 surface mapping campaigns are the only source of fracture spacing data. No subsurface information regarding the distribution of spacing measurements was available as the orientation and location of individual fractures were not recorded during the slim hole drilling program. Measurements of true spacing were collected from three mapping stations located in the North Reservoir and four mapping stations located in the South Reservoir. True spacing measurements collected from mapping stations located in the South Reservoir were not directly measured, but estimated (see section 3.6.2.1).

A total of 48 individual true spacing measurements were recorded, 11 of which were for fracture sets other than sets A – G. Estimates of spacing along a traverse lines at two separate mapping stations in the North Reservoir were also completed in 2013. Figure 4.6a is a plot of relative frequency versus true fracture spacing measurements collected from mapping stations in the North and South Reservoirs. Figure 4.6b and c are plots of relative frequency versus fracture spacing along traverse lines at mapping stations MAP_2013-03 and MAP_2013-04 respectively. It can be seen that in all three cases, the distribution of spacing measurements can be approximated using a negative exponential distribution. Therefore, it can be inferred that the location of fracture centers in space can be statistically represented using a Poisson process, which supports the use of the Enhanced Baecher fracture generation model to generate the DFN simulations of the South Reservoir (see sections 2.2.2.1).

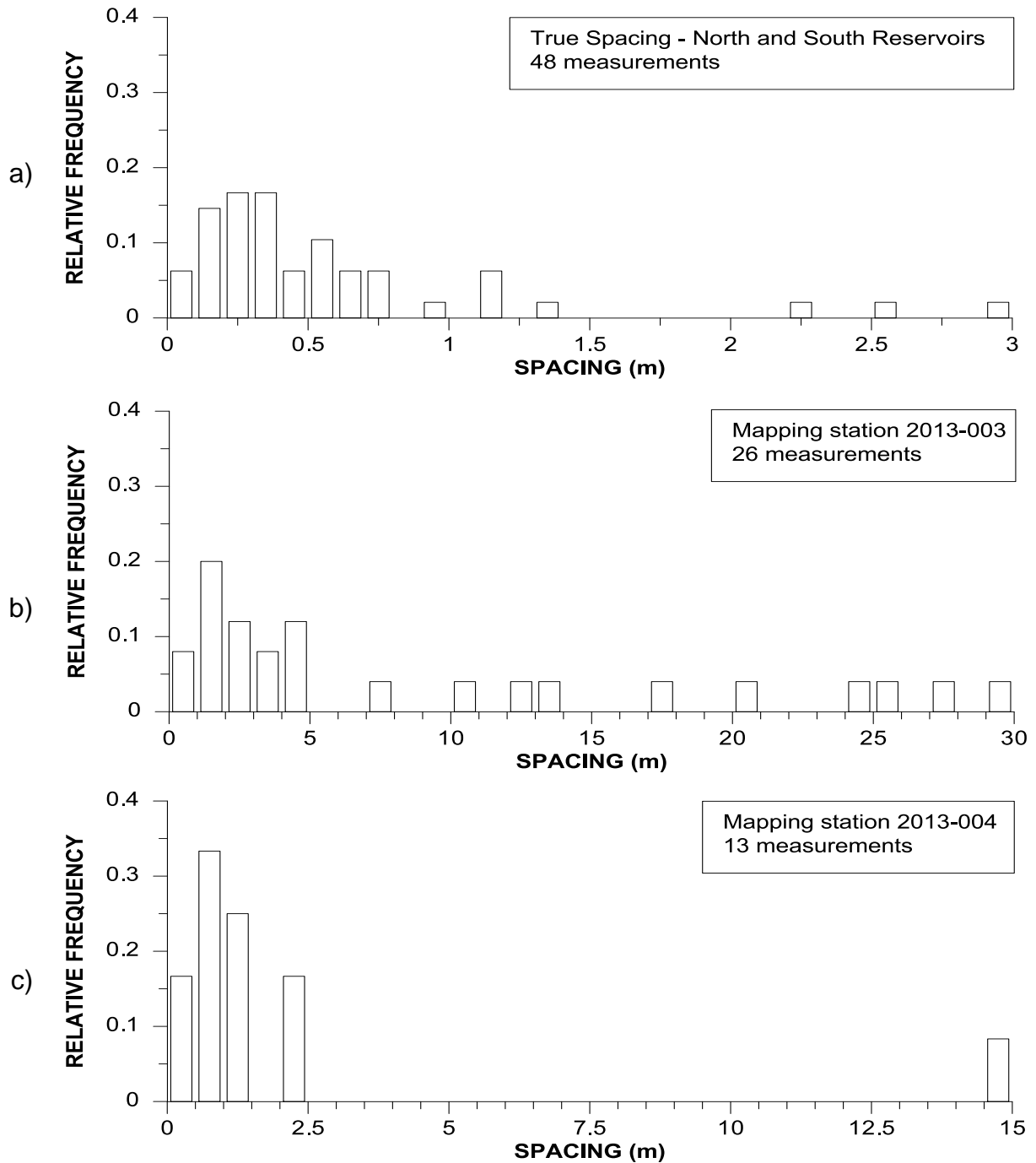


Figure 4.6 a) Combined histogram of true fracture spacing measurements collected from surface mapping of quartz diorite outcrops located in the North and South Reservoir structural domains.
b) and c) Spacing between adjacent fractures along two traverse lines at mapping stations 2 and 3 in the North Reservoir Structural Domain.

Ideally, if a large population of spacing measurements exist for each identified fracture set, the average linear fracture intensity, P_{10} , can be calculated and used to develop stochastically representative DFN models. This is achieved by fitting distribution curves to fracture spacing frequency plots for each individual fracture set, then populating a three-dimensional model volume using the derived statistical parameters such as mean and standard deviation. Due to the limited amount of spacing measurements available, distribution curves for individual fracture sets could not be derived. Future field investigations should prioritize the sampling of true fracture spacing measurements from outcrops within the South Reservoir for all of the fracture sets identified in Table 4.3. Variations in fracture spacing with depth is another important parameter that can be determined by logging the depth and true orientation of individual fractures intersected by exploratory boreholes. This is achieved by using oriented diamond drilling techniques or acoustic/optical televiewer surveys of uncased boreholes.

4.2.4 Fracture Trace Length

Fracture size distributions were calculated by estimating an equivalent radius distribution from a sample of trace length measurements. A total of 82 trace length measurements were recorded from mapping stations in the North Reservoir. Using statistical functions embedded in the software Matlab, negative exponential, lognormal and gamma distribution curves were fitted to the entire population of trace length measurements, as well as a censored population of trace length measurements that exclude all trace lengths under 0.5 m. The process of censoring trace length populations to exclude measurements below a minimum value is common in studies

that infer fracture radius distributions from trace length distributions. This is due to the fact that small fractures have minimal impact on large-scale fracture network connectivity assessments, and that a practical cut-off length must be established because fractures exist down to the microscopic scale (Billaux et al. 1989; Priest 1993). The added benefit of removing small fractures from DFN models significantly reduces the model size and increases computational speed.

The distribution of trace length measurements and fitted probability distribution functions are plotted in Figure 4.7, and the distribution parameters are summarized in Table 4.4. It was found that a negative exponential distribution function provides the best statistical fit to the censored trace length population.

Table 4.4 Summary of distribution parameters for trace length data

DISTRIBUTION	ALL DATA		TRACE LENGTHS > 0.5 m	
	Mean	Standard Deviation	Mean	Standard Deviation
Exponential	3.63	-	5.47	-
Lognormal	0.45	1.29	1.21	0.99
	Alpha	Beta	Alpha	Beta
Gamma	0.72	5.07	1.15	4.75

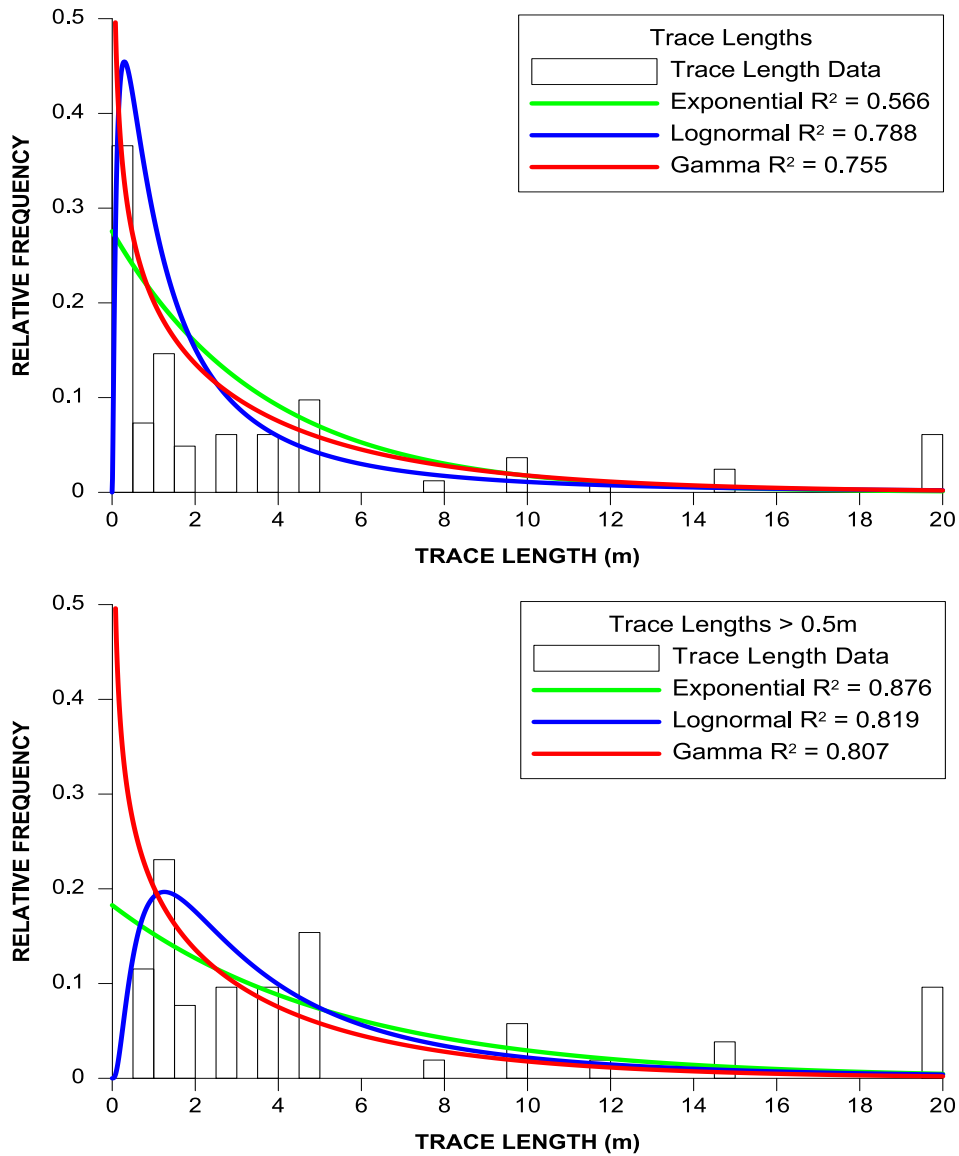


Figure 4.7 Distribution of trace length measurements for all fractures

It was assumed that the size of all fractures within the South Reservoir can be represented using the negative exponential distribution that was fitted to the censored trace length population, and therefore the mean equivalent radius of the fracture size distribution is equal to 5.5 m. This derivation of the fracture size distribution is quite simplistic and does not account for sampling biases. As discussed in section 2.2.1.2,

derivation of an equivalent fracture radius distribution from a sample of trace length measurements requires that biases in the data that arise from the sampling methodology (line versus area mapping) are corrected. Also, the orientation of the sampling plane has a significant impact on the mean and standard deviation of observed trace lengths, which in turn affects the fracture size distribution (Zhang et al. 2002). Given that mapping stations were not surveyed and the sampling method used to collect trace length measurements was not reported, sampling biases could not be corrected. Consequently, a significant amount of uncertainty exists in the assumed fracture size distribution.

CHAPTER 5: DFN MODEL DEVELOPMENT AND ANALYSIS RESULTS

DFN models for the South Reservoir were created based on two geologic models. The first model assumes the entire basement complex of the South Reservoir can be represented by a uniform rock mass with equivalent fracture distribution properties. The second model is referred to as the Meager Creek Fault model, and incorporates a 100 m wide fault zone representing the north-dipping Meager Creek Fault. This chapter reviews the methodology used to generate DFN simulations based on these two geologic models and the results derived from fracture cluster and well connectivity analyses.

5.1 Methodology Used for DFN Model Simulation and Connectivity Analyses

The creation of DFN models using FracMan for the purpose of assessing fracture network connectivity is summarized by the following procedure:

1. Define model boundaries and individual fracture sets;
2. Populate model volumes with individual fracture sets for a range of global volumetric fracture intensities (P32) between 0.05 – 0.5 m²/m³;
3. Verify the peak orientation and relative fracture intensity for each fracture set generated;
4. Run cluster and well connectivity analyses on each DFN simulation; and
5. Extract and compile the statistics derived from the cluster and well connectivity analyses.

5.1.1 Population of DFN Models Using Individual Fracture Sets

Three-dimensional DFN models were created using the fracture modelling software FracMan. DFN models were created through the generation of seven individual fracture sets over a model volume representative of the South Reservoir structural domain. A wide range of model inputs were tested, leading to the simulation of over a thousand unique DFN models. The wide range of model inputs is reflective of the high degree of geological uncertainty associated with the characterization of individual fracture sets. This high degree of geological uncertainty is a direct result of the absence of several key fracture parameters that were not collected during exploratory field investigations.

The model volume representing the South Reservoir was populated assuming a range of global P32 fracture intensities between 0.05 – 0.5 m²/m³. Weighted P32 values were derived for individual fracture sets and were calculated based on the relative occurrence of each fracture set over all mapping stations located in the North, South, and East of Camp Fault structural domains. The orientation of surface outcrops at each mapping station was unknown due to a lack of survey data. It follows that the relative occurrence of each fracture set could not be adjusted to account for sampling biases that arise from the orientation of outcrop surfaces relative to individual fracture orientations. If it is assumed that the orientation of outcrop surfaces is randomly distributed amongst all of the mapping stations in the North, South, and East of Camp Fault structural domains and that a similar number of fractures were recorded at each mapping station, the degree of error in the relative occurrence weighting factors will be minor.

Up to thirty unique fracture files were generated using a Monte Carlo fracture generation algorithm for each of the seven fracture sets. For each fracture set, the thirty fracture files generated are stochastically similar, however the size, shape, and orientation of individual fractures will vary according to the statistical distributions used to represent the range of expected fracture properties. A single DFN model simulation was created by randomly selecting a single fracture file from each of the seven fracture sets, and combining them into a single model space.

For each DFN model simulation, a stereonet of the simulated fracture network was generated and compared to the combined surface mapping stereonet shown in Figure 4.5 to ensure that peak orientations and the relative frequency of fracture sets in the simulated fracture network were representative of the observed fracture population. Individual fractures that plotted outside of the dip/dip direction ranges of the seven fracture sets were removed prior to completing the cluster and well connectivity analyses.

5.1.2 Number of Unique DFN Simulations

It was found that thirty simulations minimized the amount of computing time required to generate multiple DFN models while providing a sufficiently large sample size to derive meaningful fracture connectivity statistics. The minimum number of unique DFN simulations was determined by analysing the results of sensitivity analyses that tested the effects of various fracture size and fracture spacing combinations of two perpendicular fracture sets on the size and density of connected fracture networks. Up

to 100 unique DFN simulations were generated for several combinations of fracture spacings and sizes. The connected fracture network P32 was recorded for each DFN simulation. Cumulative standard deviation and cumulative average plots of connected fracture network P32 versus the number of simulations run are plotted in Figure 5.1. After approximately ten simulations, the cumulative standard deviation and cumulative average curves for all fracture spacing and fracture size combinations are relatively flat, indicating that subsequent DFN model simulations produce statistically similar connected fracture networks. Given that the DFN models of the South Reservoir involve a greater number of fracture sets, a minimum of thirty unique DFN simulations were completed for each global P32 value examined.

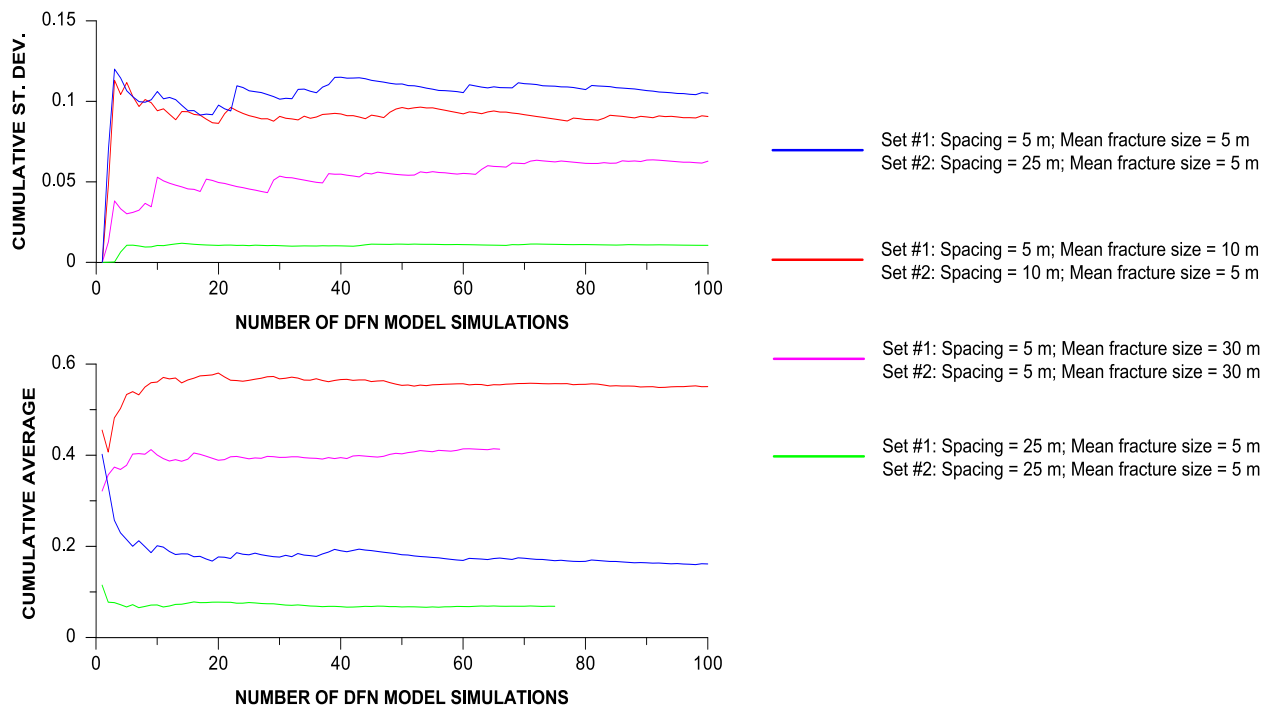


Figure 5.1 Cumulative standard deviation and cumulative average of simulated connected fracture network P32 versus the number of DFN model simulations for various combinations of fracture spacing and fracture size distributions.

5.1.3 Exclusion of Randomly Oriented Fractures

DFN model simulations did not include randomly oriented fractures that fell outside of the dip/dip direction ranges of fracture sets A – G. It was found that the inclusion of a set of randomly oriented fractures skewed the relative frequency of the other seven fracture sets. Therefore, the results of the connectivity and well analyses assume that randomly oriented fractures outside of fracture sets A – G do not contribute to overall fracture network connectivity. In the context of estimating the production potential of a geothermal reservoir, this is a conservative assumption given that the inclusion of randomly oriented fractures will increase overall fracture network connectivity values.

5.1.4 Cluster Analysis

The built-in cluster analysis function in FracMan allows users to assess the degree of compartmentalization of fracture networks by identifying all of the self-connected fracture clusters that exist within a DFN model (Golder Associates Inc. 2011). Users have the options to specify the minimum number of fractures that constitute a self-connected cluster, and to constrain the cluster analysis to a subset of fractures by applying fracture filters (see section 5.1.6). A minimum self-connected cluster size of 2000 fractures was assumed for all cluster analyses.

When a cluster analysis is run, the following statistics are provided for each identified self-connected cluster:

- The total number of fractures that comprise the cluster;
- The total connected surface area; and

- The P32 of the self-connected cluster, calculated by dividing the total connected surface area by the volume of the self-connected cluster. By default, the volume of the self-connected cluster in FracMan is determined through the integration of a three-dimensional region (referred to as a cluster hull) encompassing the maximum extents of the connected fracture cluster.

Using the statistics generated from the cluster analysis, the overall size and fracture intensity of self-connected clusters can be assessed.

5.1.5 Well Connectivity Analysis

The well connectivity analysis involved the insertion of up to 32 sampling wells of varying orientations and collar locations into each DFN model simulation. Fracture network metrics that are derived from the well connectivity analysis include:

- Number of connected and non-connected fractures intersected by a well;
- Observed and connected linear fracture frequency, P10, along the well trace;
- Spatial distribution and extent of self-connected clusters through a comparison of intersected clusters observed in adjacent wells; and
- Effects of well orientation on the probability of intersecting self-connected clusters.

In addition to the 32 sampling well locations, well connectivity analyses were run on slim holes M09-80D and M10-80D, which were inserted into each DFN. Collar locations and

well trajectories for all wells used in the well connectivity analyses are summarized in Table 5.1.

Table 5.1 Collar survey of wells used in well connectivity analyses

VERTICAL WELLS					INCLINED/DEVIATED WELLS				
Name	Easting	Northing	Trend	Plunge	Name	Easting	Northing	Trend	Plunge
WELL_01	463075	5601350	000	-90	WELL_20	463981	5601324	048	-80
WELL_02	463475	5601350	000	-90	WELL_21	463981	5601324	048	-55
WELL_03	463875	5601350	000	-90	WELL_22	463981	5601324	048	-30
WELL_04	464275	5601350	000	-90	WELL_29	463981	5601324	048	0
WELL_05	463075	5601750	000	-90	WELL_30	463981	5601324	298	-75
WELL_06	463475	5601750	000	-90	WELL_31	463981	5601324	298	-50
WELL_07	463875	5601750	000	-90	WELL_32	463981	5601324	298	-25
WELL_08	464275	5601750	000	-90	WELL_39	463981	5601324	298	0
WELL_09	463075	5602150	000	-90	WELL_40	463701	5601994	048	-80
WELL_10	463475	5602150	000	-90	WELL_41	463701	5601994	048	-55
WELL_11	463875	5602150	000	-90	WELL_42	463701	5601994	048	-30
WELL_12	464275	5602150	000	-90	WELL_49	463701	5601994	048	0
WELL_13	463075	5602550	000	-90	WELL_50	463701	5601994	298	-75
WELL_14	463475	5602550	000	-90	WELL_51	463701	5601994	298	-50
WELL_15	463875	5602550	000	-90	WELL_52	463701	5601994	298	-25
WELL_16	464275	5602550	000	-90	WELL_59	463701	5601994	298	0
					M09-80D	463981	5601324	051	-72
					M10-80D	463701	5601994	056	-64

Sixteen vertical sampling wells, labelled Wells 1 – 16, were distributed over the South Reservoir model region in 1,200 m x 1,200 m square grid aligned in a north-south/east-west orientation. Wells located on the perimeter of the grid were spaced 200 m from the boundary limits of the model and have a total length of 1,000 m. The location of Wells 1 – 16 are shown in Figure 5.2.

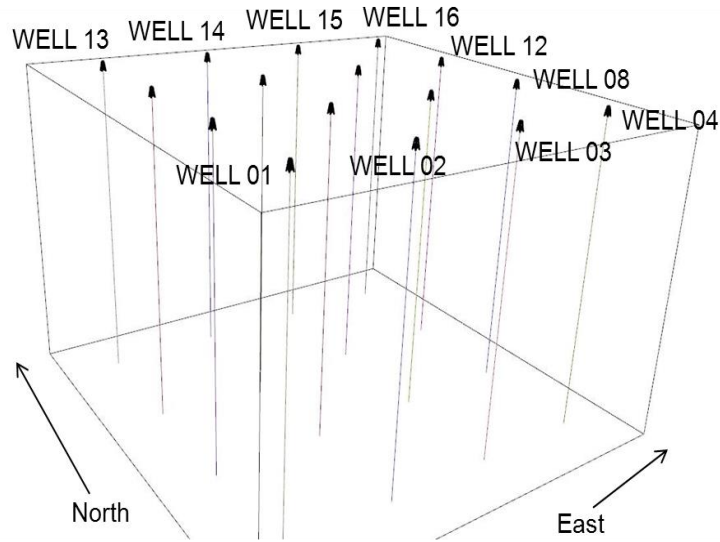


Figure 5.2 Location of vertical sampling wells 1 - 16

The effect of well orientation and location on the number of intersected fractures was assessed using sixteen inclined samplings wells. Eight wells (numbers 20 – 22, 29, 30 – 32, and 39) have the same length and collar location as slim hole M09-80D, and the remaining eight wells (numbers 40 – 42, 49, 50 – 52, and 59) have the same length and collar location as slim hole M10-80D. Wells 20 – 22, 29, 40 – 42, and 49 are drilled towards an azimuth of 048, perpendicular to fracture set A. Wells 30 – 32, 39, 50 – 52, and 59 are drilled towards an azimuth of 298, and are approximately perpendicular to fracture sets C and D. The location and orientation of the 16 oriented wells are shown in Figure 5.3.

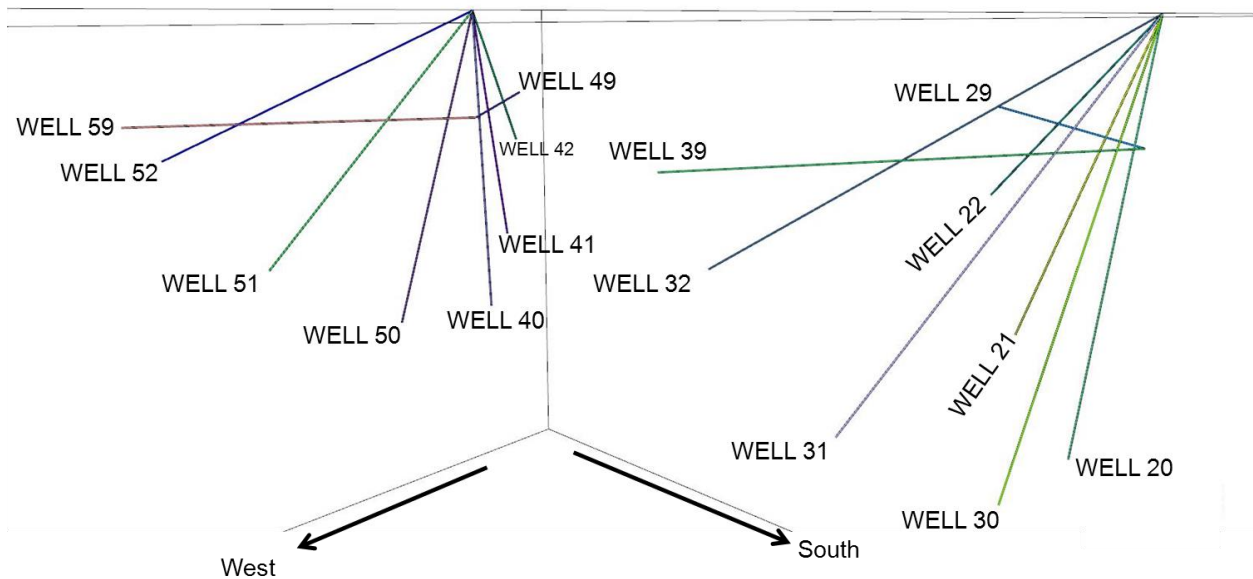


Figure 5.3 Orientation and location of inclined sampling wells. Wells 20 – 29 and 30 – 39 share the same collar location as slim hole M09-80D. Wells 40 – 49 and 50 – 59 share the same collar location as slim hole M10-80D

The well connectivity analysis allows users to compare subsurface P10 values predicted by DFN models to those observed in actual well logs, providing a means to assess the validity of the DFN model simulations. The well connectivity analysis is also used to assess the sensitivity of well orientation on the likelihood of intersecting connected fractures and the spatial distribution of self-connected clusters.

5.1.6 Transmissible Fracture Rating

Scalar properties (i.e. aperture, trace length, roughness) can be assigned to individual fractures belonging to a fracture set following a variety of distribution forms. These properties can then be used to constrain cluster and well connectivity analyses based on user-specified criteria, referred to as fracture filters.

To account for the effect of non-transmissive fractures on fracture network connectivity, individual fractures were assigned a Transmissible Fracture Rating (TFR) between 1 - 10. TFRs were assigned to individual fractures following a uniform distribution, and were used to evaluate the effect of non-transmissive fractures on cluster size. Figure 5.4 illustrates the effect of using a TFR filter to create a subset of fractures from a population of fractures assuming that only 35% of observed fractures have sufficient permeability to act as conduits for fluid flow. Figure 5.4a shows an initial population of discrete fractures and the corresponding distribution of TFRs between 1 - 10. Figure 5.4b shows the subset of fractures created from the initial population of discrete fractures by excluding fractures with TFR ratings less than 6.5.

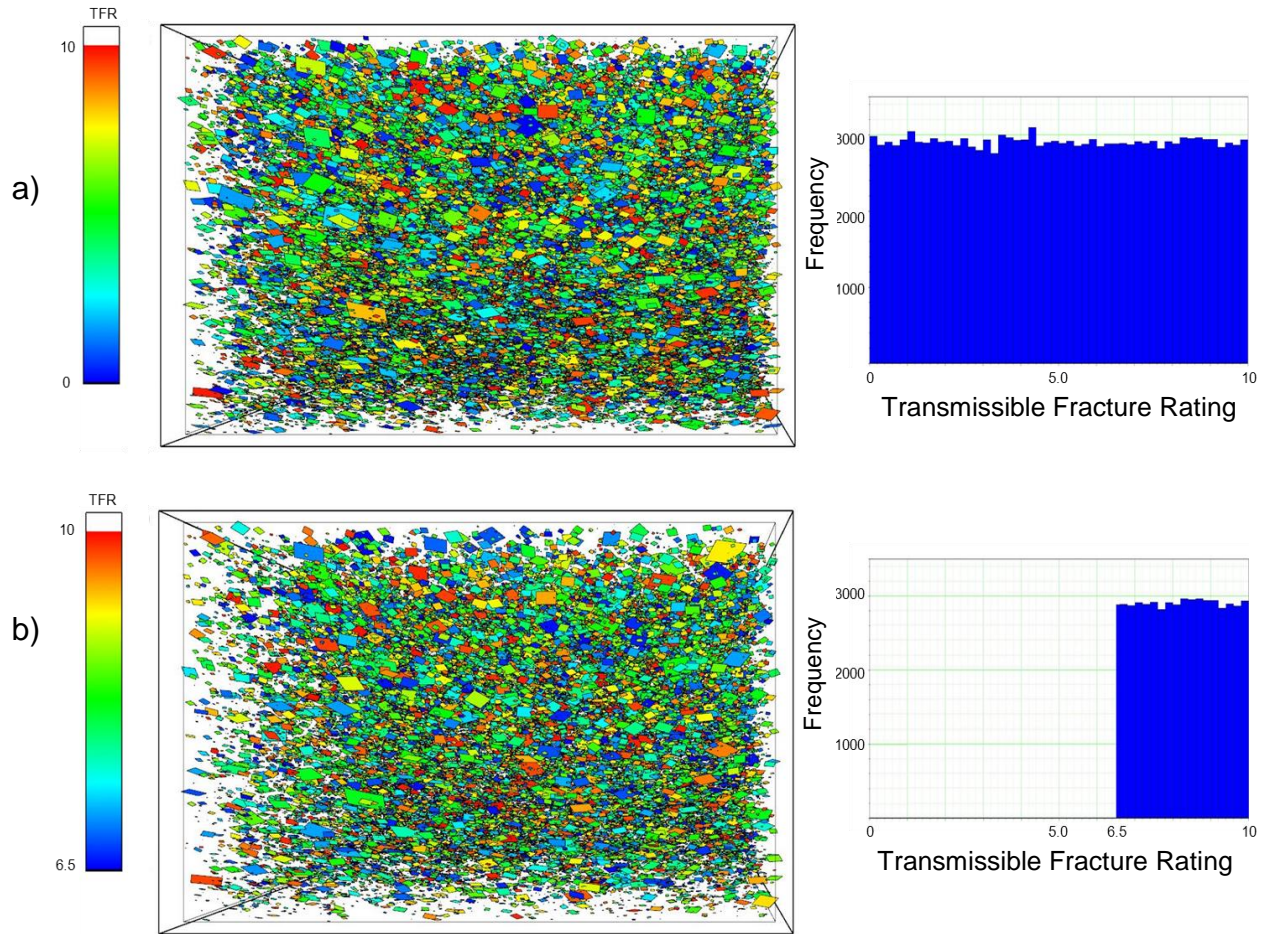


Figure 5.4 Using the Transmissible Fracture Rating (TFR) to assess cluster network connectivity, assuming only 35% of observed fractures have significant permeability. Figure 5.4a is the initial population of fractures with TFRs between 1 – 10. Figure 5.4b is the reduced population of fractures with TFRs between 6.5 – 10.

5.2 Uniform Rock Mass Model

The Uniform Rock Mass model assumes that the relative intensity of each fracture set is constant throughout the entire model volume. Results from the DFN simulations based on the Uniform Rock Mass model provide insight into the fracture network connectivity of the massive crystalline granodiorites that constitute the majority of the South Reservoir.

5.2.1 Model Boundaries and P32 Values for Individual Fracture Sets

The DFN model boundaries were determined based on the geometry of the South Reservoir structural domain, location of slim holes, depth of the geothermal anomaly, and the observed fracture frequency relative to elevation. In the east-west direction, the DFN model volume is confined to the areas between the No Good Creek and Camp Fault. The DFN model volume is bounded to the south by Meager Creek, which coincides with the surface expression of the Meager Creek Fault. The northern limit of the DFN model volume lies 1,600 m north of Meager Creek.

The model volume was divided into three sub-regions based on elevations at which fracture frequency was observed to change (see section 4.1.3). The three regions are referred to as the top, middle and bottom regions, and their UTM coordinates are summarized in Table 5.2, and illustrated in Figure 5.5.

Table 5.2 UTM coordinates of DFN model boundaries

REGION	EASTING		NORTHING		ELEVATION		VOLUME (m ³)
	Min	Max	Min	Max	Min	Max	
TOP	462 875	464 475	5 601 150	5 602 750	450	Surface	-
MID	462 875	464 475	5 601 150	5 602 750	125	450	832,000,000
BOT	462 875	464 475	5 601 150	5 602 750	-875	125	2,560,000,000

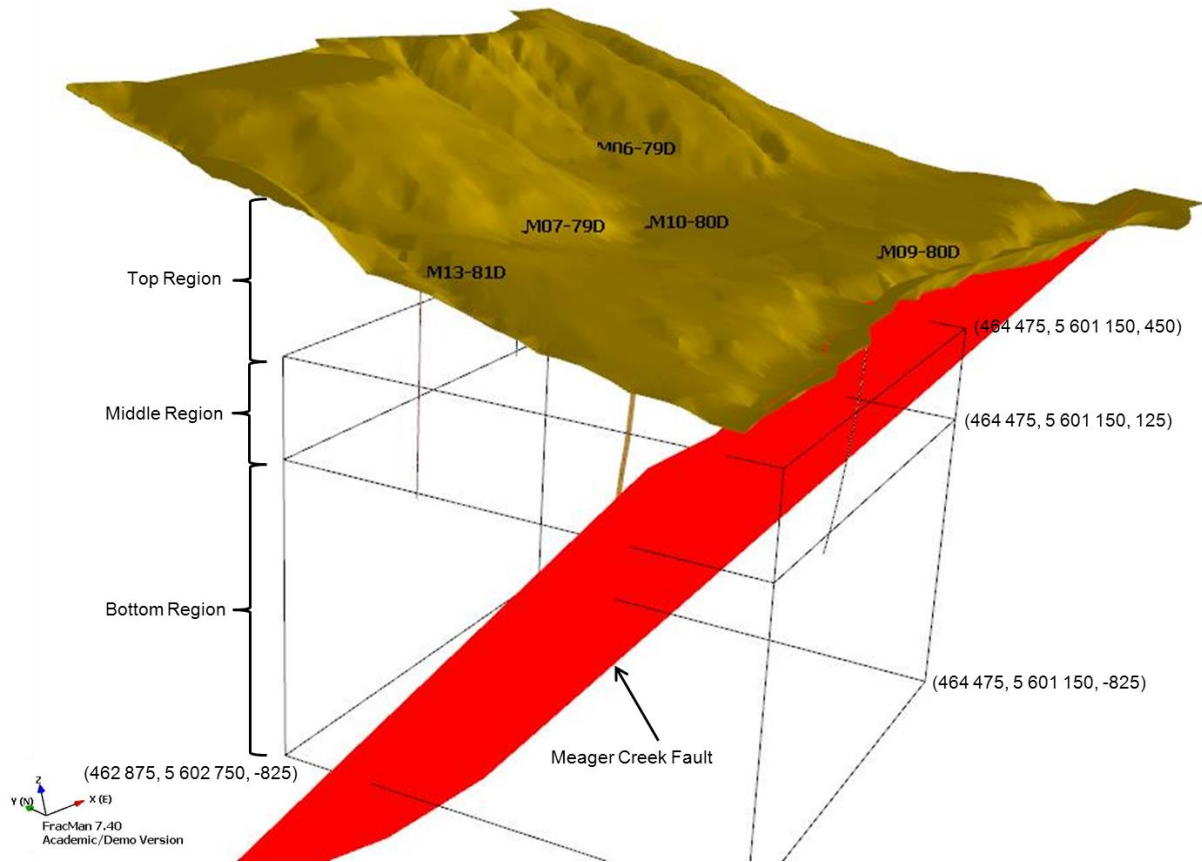


Figure 5.5 Model boundaries of the Uniform Rock Mass model, facing northeast.

DFN model simulations were limited to the Bottom Region of the Uniform Rock Mass model. Limiting the analysis to the bottom region significantly reduced the amount of computing time required to generate individual DFN models while fully encompassing the portions of the South Reservoir that exhibited the highest temperature gradients.

The Uniform Rock Mass model assumes that the presence of the Meager Creek Fault has no influence on global fracture intensities. As such, the results from the cluster and well connectivity analyses provide insight into the fracture network behaviour of the

massive, crystalline granodiorites that comprise a substantial portion of the hanging and footwalls of the Meager Creek fault.

The weighted P32 values for individual fracture sets are consistent over the entire bottom region in the Uniform Rock Mass model. The weighted P32 values for individual fracture sets are summarized in Table 5.3.

Table 5.3 Weighted P32 values for fracture sets in the Uniform Rock Mass model

SET NAME	RELATIVE OCCURRENCE	GLOBAL P32 VALUES (m^2/m^3)				
		0.05	0.1	0.3	0.5	0.7
SET A	23.7%	0.0119	0.0237	0.0712	0.1187	0.1661
SET B	4.9%	0.0025	0.0049	0.0147	0.0245	0.0344
SET C	15.5%	0.0077	0.0155	0.0464	0.0774	0.1083
SET D	12.1%	0.0060	0.0121	0.0363	0.0604	0.0846
SET E	6.8%	0.0034	0.0068	0.0205	0.0341	0.0478
SET F	2.3%	0.0012	0.0023	0.0070	0.0117	0.0164
SET G	4.1%	0.0021	0.0041	0.0123	0.0205	0.0288
MISC	30.5%	0.0153	0.0305	0.0916	0.1526	0.2136

5.2.2 Cluster Analysis Results

Cluster analyses were conducted on each DFN model simulation for a series of global P32 values between 0.05 – 0.5 m^2/m^3 . For each global P32 value tested, increasingly restrictive TFR filters were applied until no connected clusters could be established, thus identifying the minimum percentage of connected fractures that must exist in order for a connected cluster to develop. Summary statistics for all cluster analyses completed for the Uniform Rock Mass model are presented in Table 5.4.

Table 5.4 Summary of cluster analysis statistics from DFN simulations of the South Reservoir based on the Uniform Rock Mass Model

P32	MIN. FRACTURE AREA (m ²)	TFR FILTER	NUMBER OF ITERATIONS	TOTAL NUMBER OF CLUSTERS	NUMBER OF FRACTURES PER CLUSTER				CONNECTED FRACTURE AREA				CONNECTED FRACTURE P32			
					Average	StDev	Max	Min	Average (m ²)	StDev (m ²)	Max (m ²)	Min (m ²)	Average (m ² /m ³)	StDev (m ² /m ³)	Max (m ² /m ³)	Min (m ² /m ³)
0.05	5	100%	30	0	-	-	-	-	0	-	-	-	-	-	-	-
0.1	10	100%	30	64	95,698	413,425	2,606,174	2,001	42,721,082	181,015,885	1,119,212,700	1,023,594	0.0494	0.0782	0.4378	0.0085
0.1	10	95%	30	10	2,400	268	2,767	2,068	1,325,385	153,705	1,599,262	1,143,702	0.0136	0.0023	0.0175	0.0093
0.1	10	90%	30	0	0	-	-	-	0	-	-	-	-	-	-	-
0.2	10	100%	30	30	905,994	1,303,463	6,494,545	504,658	321,029,763	424,598,258	2,139,247,000	190,443,600	0.1254	0.1658	0.8354	0.0744
0.2	10	75%	30	30	288,208	1,237	290,350	285,813	122,785,669	534,297	123,965,170	121,791,620	0.0480	0.0002	0.0485	0.0476
0.2	10	60%	30	35	122,780	49,039	149,857	2,029	58,564,110	23,394,731	71,566,248	969,045	0.0260	0.0027	0.0281	0.0162
0.2	10	50%	30	121	3,652	1,717	10,841	2,031	1,940,571	914,154	5,757,753	1,061,142	0.0128	0.0024	0.0194	0.0075
0.2	10	43%	30	0	0	-	-	-	0	-	-	-	-	-	-	-
0.3	10	100%	30	30	1,264,877	1,249,934	7,297,201	946,207	409,941,460	387,854,618	2,273,455,900	311,560,290	0.1601	0.1515	0.8878	0.1217
0.3	10	75%	30	30	616,138	1,263	618,248	613,896	222,161,697	364,995	222,987,720	221,372,900	0.0868	0.0001	0.0871	0.0865
0.3	10	50%	30	30	287,500	1,192	289,978	285,504	122,548,837	505,808	123,449,640	121,506,860	0.0479	0.0002	0.0483	0.0475
0.3	10	45%	30	30	218,635	1,889	221,580	214,902	98,121,854	831,475	99,526,071	96,463,615	0.0385	0.0003	0.0390	0.0377
0.3	10	40%	30	33	130,639	40,133	151,025	2,470	62,360,389	19,164,979	72,184,161	1,178,336	0.0265	0.0021	0.0286	0.0173
0.3	10	35%	30	182	7,230	7,216	40,876	2,014	3,722,434	3,709,319	20,985,072	1,026,761	0.0133	0.0025	0.0191	0.0081
0.3	10	30%	30	2	2,499	234	2,732	2,265	1,403,765	120,393	1,524,158	1,283,372	0.0114	0.0002	0.0116	0.0112
0.3	10	25%	3	0	0	-	-	-	0	-	-	-	-	-	-	-
0.4	10	100%	30	30	1,403,342	2,023	1,407,021	1,399,057	427,509,020	391,718	428,337,990	426,846,540	0.1670	0.0002	0.1673	0.1667
0.4	10	75%	30	30	949,259	1,530	952,712	946,182	311,540,825	432,818	312,571,160	310,563,240	0.1217	0.0002	0.1221	0.1213
0.4	10	50%	30	30	505,807	1,399	508,085	502,797	190,369,593	476,557	191,416,520	189,209,190	0.0744	0.0002	0.0748	0.0739
0.4	10	35%	30	30	241,389	1,652	245,123	237,496	106,293,529	781,091	108,084,800	104,500,240	0.0416	0.0003	0.0423	0.0409
0.4	10	30%	30	37	115,035	54,377	148,872	2,058	54,917,121	25,966,479	71,309,490	958,881	0.0254	0.0033	0.0281	0.0140
0.4	10	25%	30	123	3,588	2,103	14,076	2,006	1,905,303	1,111,078	7,410,606	1,030,125	0.0130	0.0027	0.0205	0.0068
0.4	10	20%	30	0	0	-	-	-	0	-	-	-	-	-	-	-
0.5	10	100%	30	30	1,860,673	2,388	1,866,187	1,855,377	541,161,714	453,436	542,179,660	540,373,710	0.2113	0.0002	0.2117	0.2110
0.5	10	30%	29	29	286,903	2,031	290,223	283,291	122,253,021	884,636	123,850,900	120,632,480	0.0478	0.0003	0.0484	0.0472
0.5	10	25%	30	32	158,204	40,304	176,550	2,209	73,902,248	18,826,609	82,396,025	1,023,200	0.0306	0.0017	0.0323	0.0230
0.5	10	20%	29	124	3,596	1,802	12,123	2,000	1,906,407	950,170	6,366,908	1,047,927	0.0129	0.0024	0.0188	0.0070
0.5	10	15%	30	0	0	-	-	-	0	-	-	-	-	-	-	-

1. Clusters statistics are based on DFN simulations confined to the bottom region of the South Reservoir

2. Clusters are comprised of a minimum of 2000 connected fractures.

An analysis of the cluster statistics reveals the following trends:

- No fracture clusters will develop below a global P32 value of $0.1 \text{ m}^2/\text{m}^3$;
- At higher global P32 values, there is a cut-off limit determined by the TFR filter where the size of connected clusters rapidly decreases from extending across the entire model space to small, isolated areas;
- At the TFR cut-off limit, the average P32 of individual clusters approaches $0.013 \text{ m}^2/\text{m}^3$.

5.2.2.1 Effect of Global P32 Fracture Intensity on Cluster Size

Assuming a minimum connected cluster size of 2000 individual fractures, the basement granodiorites of the South Reservoir must have a minimum global P32 = $0.1 \text{ m}^2/\text{m}^3$ in order for connected clusters to develop. On average, a global P32 = $0.1 \text{ m}^2/\text{m}^3$ is equivalent to an observed fracture frequency of 0.031 m^{-1} and 0.024 m^{-1} for drillholes M09-80D and M10-80D respectively (approximately one fracture every 35 m of core drilled). This indicates that even at very low fracture frequencies, it is possible that small, connected fracture clusters may exist.

As the global P32 fracture intensity is increased, so does the average size, connected surface area, and the P32 of the connected clusters. If 100% of the fractures are assumed to be transmissive, connected clusters will span the entire model volume at a global P32 = $0.2 \text{ m}^2/\text{m}^3$. Further increases in global P32 values increases the fracture density of connected fracture clusters, indicated by the increasing average connected P32 values.

5.2.2.2 Effect of TFR Filters on Cluster Size

In a fractured rock mass, typically only a small percentage of the observed fractures have sufficient permeability to allow for fluid circulation (see section 4.1.5). Using DFN model simulations, the minimum percentage of permeable fractures required for connected clusters to develop was assessed by applying increasingly restrictive TFR filters. Figure 5.6 is a plot of the ratio of fracture cluster volume relative to model volume versus the percentage of permeable fractures in the DFN simulation. As the percentage of permeable fractures decreases, the ratio of cluster volume to model volume rapidly decreases once a certain minimum percentage of permeable fractures is reached, referred to as the TFR cut-off limit.

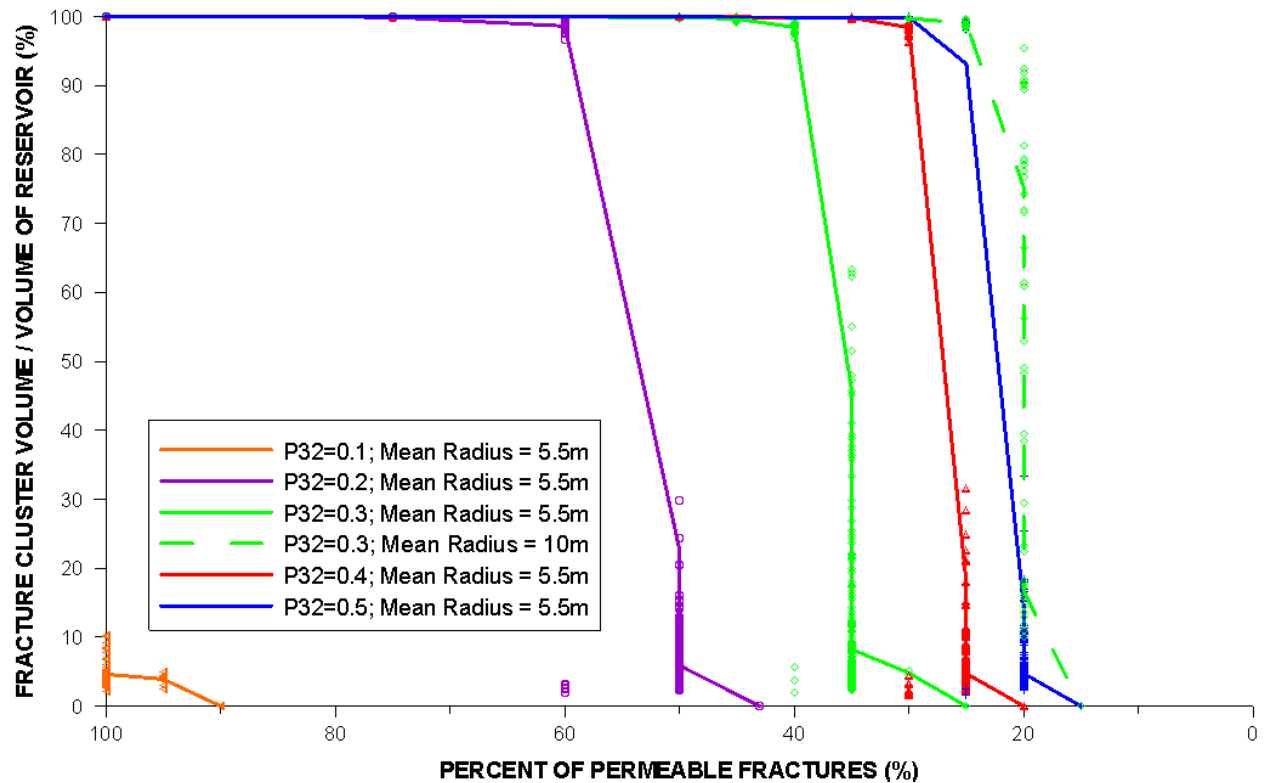


Figure 5.6 Effects of TFR filter criteria on the size and extent of connected fracture clusters

From Figure 5.6, it can be seen that fracture clusters will span the entire model volume up until the TFR cut-off limit is reached, at which point the size of the clusters rapidly decreases to zero. This behaviour has been observed in network connectivity studies in other disciplines such as biology and electrical engineering, and can be explained using percolation theory. Percolation theory establishes a relationship between the development of largely clustered networks of randomly distributed objects over a region and the concentration of objects within that region. A comprehensive description of percolation theory and its application to fracture connectivity is provided by Dershowitz (1984). In essence, the TFR cut-off limit is dependent on fracture network properties which include global fracture intensity and fracture size.

A large global P32 value means that there is a greater density of fracture surface area per unit volume, thus there is a greater likelihood that the existing fractures will form a connected fracture network. This explains why at increasingly larger global P32 values, large connected clusters develop at increasingly lower percentages of permeable fractures. For example, at a global $P32 = 0.2 \text{ m}^2/\text{m}^3$, at least 50% of fractures must be permeable before connected fracture clusters will develop. For a global $P32 = 0.5 \text{ m}^2/\text{m}^3$, connected fracture clusters will develop up until the percentage of permeable fractures falls to 20%. By analyzing the P32 values of the fracture clusters that develop near the TFR cut-off limit, it was found that the average P32 of individual clusters approaches $0.013 \text{ m}^2/\text{m}^3$ for the range of global P32 values tested.

The TFR cut-off limit is also controlled by the fracture size distribution. Fracture networks that have a greater concentration of large fractures are more likely to create extensive connected clusters at a lower TFR cut-off limit compared to fracture networks that are mostly comprised of small fractures. This point is illustrated in Figure 5.6 by comparing the curves of two different fracture size distributions for a constant global P32 of $0.3 \text{ m}^2/\text{m}^3$. The solid and dashed green lines represent the size of clusters that develop following a negative exponential fracture size distribution with mean equivalent radii of 5.5 m and 10 m respectively. The effect of increasing the mean equivalent radius from 5.5 m to 10 m is that the TFR cut-off limit falls from 35% to 20%, and that the self-connected clusters that develop at the TFR cut-off limit have a greater average number of fractures and connected surface area per cluster for a mean equivalent radius of 10 m. These results are summarized in Table 5.5.

Table 5.5 Comparison of connected cluster size assuming different fracture size distributions at the TFR cut-off limit

Mean Radius (m)	% of Connected Fractures at the TFR Cut-off Limit	Average Number of Fractures per Cluster	Average Connected Fracture Area (m^2)	Average P32 of Connected Fractures (m^2/m^3)
5.5	35%	7,230	3,722,434	0.0133
10	20%	10,189	16,013,083	0.0109

From a geothermal development standpoint, the significance of the TFR cut-off value is that it represents a threshold value at which the probability that a uniform rock mass will contain large connected clusters approaches zero. The TFR cut-off value is highly dependent on the global fracture intensity, the percentage of permeable fractures, and

the size of fractures. To a certain extent, all of these factors can be quantified during prefeasibility level field investigations.

5.2.3 Well Connectivity Analysis Results

Results from the well connectivity analysis indicate that the number of fractures intersected by a well is fairly insensitive to the location of individual well locations, but sensitive to well orientation. The insensitivity of P10 to well location is expected given that the Uniform Rock Mass model assumes an equal distribution of fracture properties over the entire South Reservoir. It follows that the orientation of production wells must be carefully planned in order to optimize the likelihood of intersecting highly connected fractures. It was also found that a poor correlation exists between P10 values calculated from downhole RQD measurements in slim holes M09-80D and M10-80D and those obtained from the DFN simulations.

5.2.3.1 P10 as a Function of Well Location

The sensitivity of different well locations on the number of intersected fractures was assessed using sixteen vertical sampling wells. Because all of the vertical sampling wells have the same length and orientation, the total number of fractures intersected by each well can be directly compared in order to identify regions of high and low fracture densities. Figure 5.7 is a contour plot of the average number of fractures intersected by vertical wells for a global P32 of $0.5 \text{ m}^2/\text{m}^3$. The maximum and minimum average number of fractures intersected by a single well was 115 and 92 fractures for Wells11 and 9 respectively. Considering that each well has a total length of 1000 m, this equates

to Well 11 intersecting one additional fracture every 43 m compared to Well 9. Considering the heterogeneous nature of rock masses, this difference is insignificant and infers that no spatial variation in fracture density exists in the Uniform Rock Mass model. This behaviour is expected given that the Uniform Rock Mass model assumes an equal distribution of fracture properties over the entire South Reservoir.

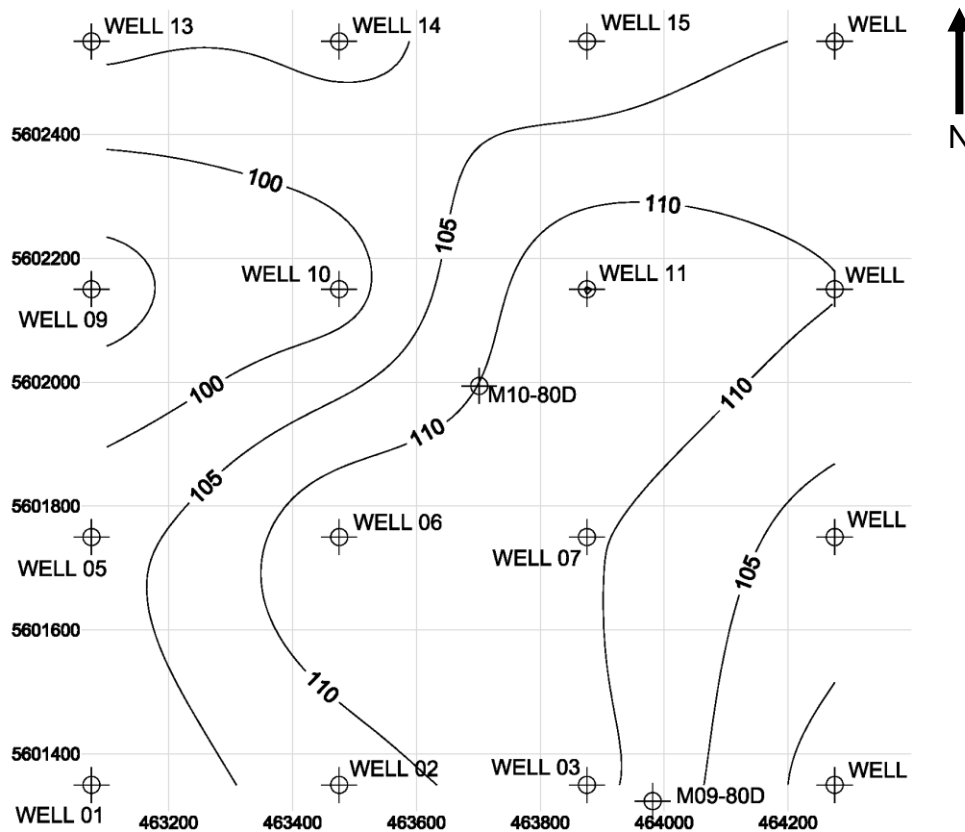


Figure 5.7 Contour lines based on the average number of fractures intersected by vertical wells for DFN simulations with a global $P32 = 0.5 \text{ m}^2/\text{m}^3$. Slim holes M09-80D and M10-80D are plotted for reference only, and were not used to generate the contours

5.2.3.2 P10 of Connected Fractures in Vertical Wells

The average number of connected fractures intersected by each vertical well was determined by using TFR filters to exclude non-transmissive fractures from the well connectivity analysis. As the TFR cut-off limit is approached, the likelihood that a well will intersect a connected cluster approaches zero. Figure 5.8 compares the number of intersected fractures observed in each well to the number of connected fractures as the TFR cut-off limit is approached.

Figure 5.8b shows the change in average P10 of connected fractures as the TFR cut-off limit is approached for a global $P32 = 0.3 \text{ m}^2/\text{m}^3$. When the percentage of transmissive fractures in the model is equal to 45%, 40%, and 35%, the average percentage of transmissive fractures intersected by a well is equal to 30%, 21%, and 1.3% respectively. Therefore, the ratio of transmissible fractures to the total number of fractures intersected by the vertical sampling wells is lower than the actual percentage of transmissible fractures that exist in the model.

At the TFR cut-off limit, it was found that the percentage of fractures belonging to connected clusters relative to the actual number of fracture that intersect a well is around 1% for all global P32 values tested. These results imply that if the number of conductive fractures intersected by an exploratory slim hole is known, the likelihood that significant connectivity exists can be assessed. Hydrogeological sampling methods that can be used to determine the percentage of conductive fractures in a borehole are discussed in section 6.5.1.

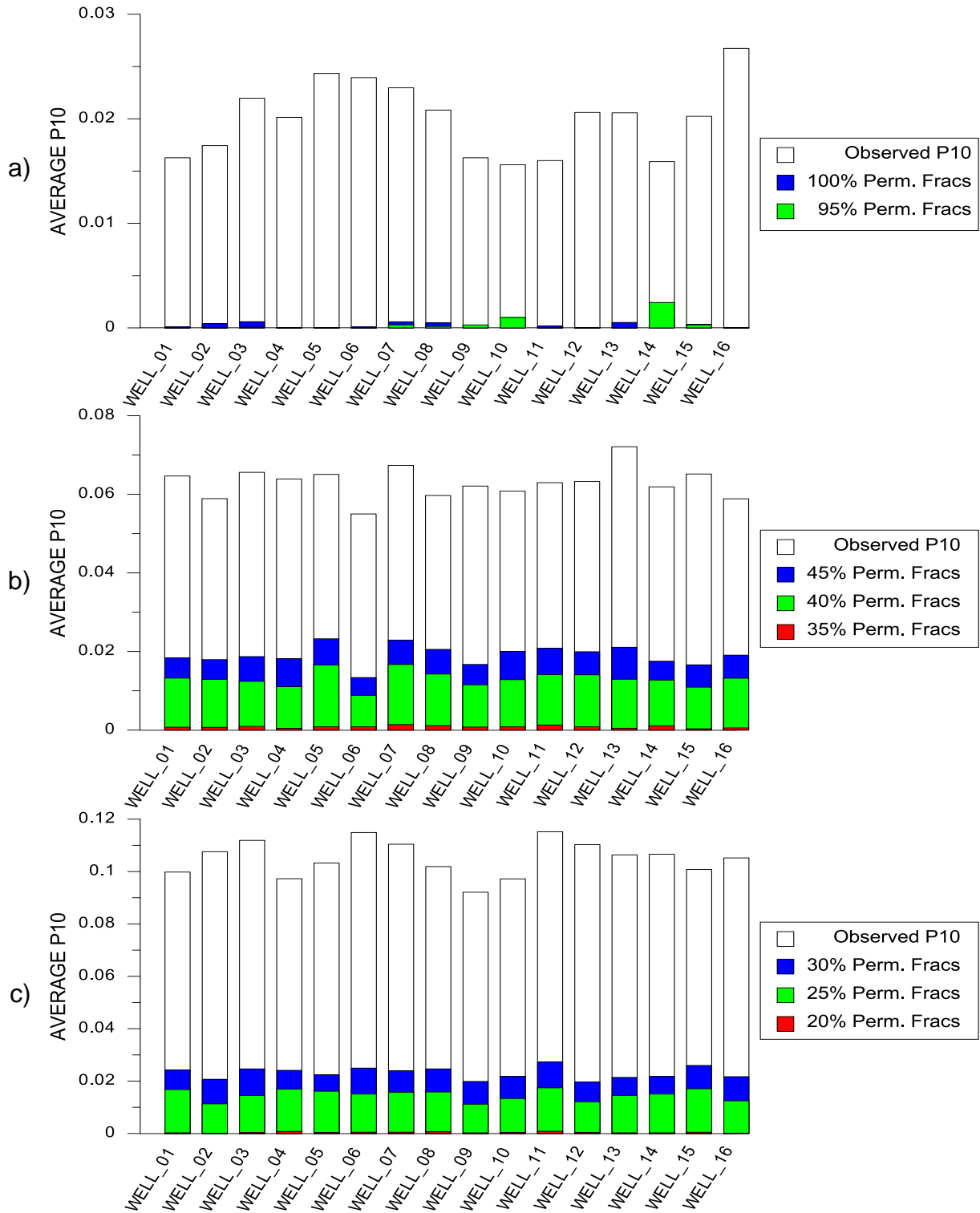


Figure 5.8 Average P10 values in vertical sampling wells as the TFR cut-off limit is approached for a) Global P32 = 0.1 m²/m³; b) Global P32 = 0.3 m²/m³; and c) Global P32 = 0.5 m²/m³

5.2.3.3 P10 of Connected Fractures in Inclined Wells

The effect of well orientation on the average number of fractures intersected was examined using 16 inclined sampling wells. The location and orientation of the inclined wells are summarized in Table 5.1. Figure 5.9 compares the number of intersected fractures observed in each well to the number of connected fractures as the TFR cut-off limit is approached for global P32 values of 0.1, 0.3, and 0.5 m²/m³. The following trends can be observed from the data:

- Wells 21, 22, and 40 – 49 have orientations that lead to the greatest average number of fractures intersected per metre;
- Wells 32 and 52 intersect significantly fewer fractures per metre compared to the vertical wells;
- At the TFR cut-off limit, well orientations can have a dramatic effect on the number of fractures intersected.

Inclined wells drilled perpendicular to the average strike of fracture set A (Wells 20 – 29 and 40 – 49) intersect more fractures per meter than wells drilled perpendicular to the average strike of fracture sets C/D (Wells 30 – 39 and 50 – 59), and the vertical sampling wells. Figure 5.9b compares the total number of fractures intersected by each well to the number of connected fractures as the TFR cut-off limit is approached. On average, Well 21 intersects the greatest number of fractures. Well 21 has an average P10 of 0.151 m⁻¹ in comparison to an average P10 of 0.105 m⁻¹ for the vertical wells, which equates to one extra fracture intersection approximately every 22 m drilled.

As the TFR cut-off limit is approached, the average connected P10 in Well 21 falls to 0.026 and 0.001 m⁻¹ for TFRs equal to 25% and 20% respectively. This is equivalent to Well 21 intersecting a fracture that is part of a connected fracture cluster approximately every 25 to 38 m. At similar TFRs, the average connected P10 for vertical wells is equal to 0.015 and 4.06 x 10⁻⁴ m⁻¹, which is equivalent to intersecting a fracture that is part of a connected cluster approximately every 68 to 2,400 m. These results show that the number of fractures intersected by a well is particularly sensitive to well orientation when the percentage of transmissive fractures approaches the TFR cut-off limit. In the case of a global P32 = 0.5 m²/m³, a well oriented perpendicular to fracture set A is expected to intersect a self-connected fracture every 38 m compared 2,400 m for a vertical sampling well.

Selection of an optimal well orientation must be conducted with care, as wellbore orientations that target a specific fracture set may lead to the under-sampling of a more important fracture set. Wells 32 and 52 intersected the fewest number of fractures of all of the wells tested. At a global P32 = 0.5 m²/m³, Wells 32 and 52 had average P10s equal to 0.071 and 0.081 m⁻¹ respectively. Compared to vertical sampling wells, this equates to one less fracture intersection approximately every 34 m drilled. The cause of the decreased number of fracture intersections becomes apparent upon examination of the stereonet plot in Figure 4.5. Although a well azimuth of 298° will tend to intersect a greater number of fractures in sets C and D, the well trajectory is now almost completely parallel to the strike of fracture set A. Consequently, fracture set A will be under-sampled by these wells. Given that fracture set A is the most prevalent of the seven

fracture sets, the total number of fractures intersected by the inclined wells with azimuths of 298° will typically be lower than the vertical wells.

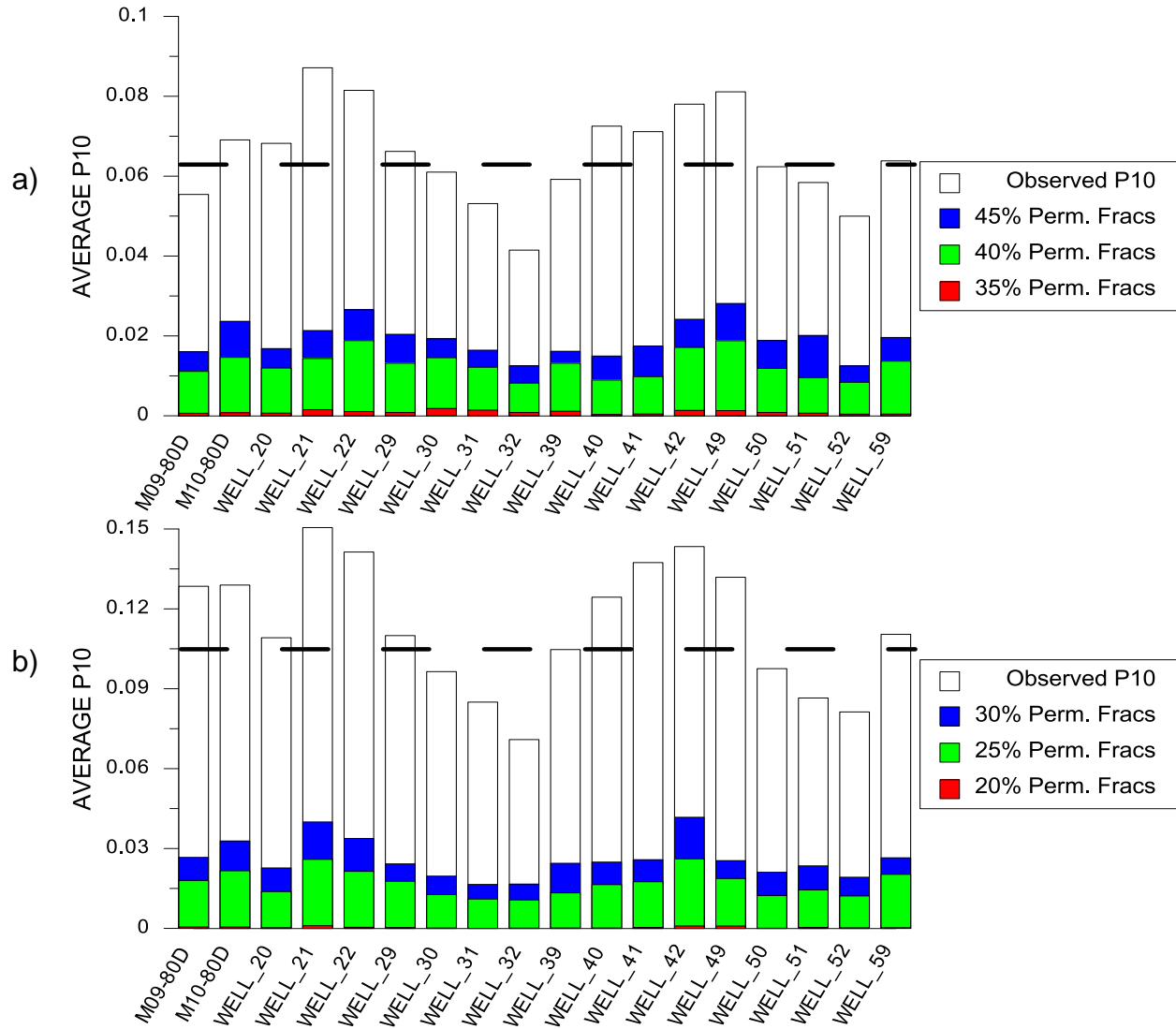


Figure 5.9 Average P10 values for inclined sampling wells as the TFR cut-off limit is approached for a) Global P32 = 0.3 m²/m³ and b) Global P32 = 0.5 m²/m³. The dashed line represents the average P10 calculated from the 16 vertical sampling wells

5.2.3.4 Comparison of Simulated and Observed P10 and RQD

A comparison of simulated P10 from slim holes M09-80D and M10-80D was completed in order to assess from DFN simulations assuming global P32 values of 0.1, 0.3, 0.5, and 0.7 m²/m³. Simulated P10 values for each slim hole were then compared to those calculated from the depth-averaged RQD measurements discussed in section 4.1.3. The results are summarized in Table 5.6.

Table 5.6 Comparison of P10 values in slim holes M09-80D and M10-80D from DFN simulations using the Uniform Rock Model and P10 values derived from depth-averaged RQD

GLOBAL P32	M09-80D		M010-80D	
	SIMULATED P10	P10 CALCULATED FROM RQD	SIMULATED P10	P10 CALCULATED FROM RQD
0.1	0.031	8.7	0.024	10.0
0.3	0.055		0.069	
0.5	0.128		0.129	
0.7	0.183		0.176	

Table 5.6 shows that there is a poor correlation between simulated and calculated P10 for the range of global P32 values tested. At an upper-bound global P32 = 0.7 m²/m³, simulated P10 values were 48 times lower than the P10 values derived from averaged RQD measurements. The poor correlation is due in part to the following factors:

- RQD reported in the drilling logs are likely much lower than the true RQD, due to the inclusion of mechanical fractures in the RQD calculation. It follows that the P10 derived from depth averaged-RQD is higher than the true P10;
- P10 calculated from depth-averaged RQD measurements will be overestimated in competent rock masses assuming a TRQD threshold value equal to 0.1 m;

- Simulated P10 will be lower than true P10 because fractures with an area less than 10 m^2 were eliminated from all DFN simulations prior to conducting well and conductivity analyses; and
- Fractures that did not fall within the dip/dip direction ranges of the seven major fracture sets were eliminated from all DFN simulations prior to conducting well and conductivity analyses, further lowering simulated P10 values.

Given the poor correlation between simulated and calculated P10, it is unclear if the results from cluster and well connectivity analyses for the range of global P32 values tested are representative of the existing fracture network in the South Reservoir. A global P32 greater than $0.7 \text{ m}^2/\text{m}^3$ for the basement rocks of the South Reservoir is unjustified given that the number of *natural* fractures intersected per meter is extremely low, and past engineering reports have characterized the basement granodiorites to be highly competent at depth. The exclusion of both small-sized and randomly oriented fractures from DFN simulations partially account for lower simulated P10 values. However, the primary cause of the discrepancy between simulated and calculated P10 is that the calculated P10 is based on inaccurate RQD measurements. This highlights the importance of recording the depth of each fracture intersected during drilling so that fracture frequency can be directly calculated from the drilling logs and RQD measurements can be verified. It is clear that a reliance on RQD measurements is inadequate for providing reliable estimates of fracture frequency in competent rock, and thus cannot be used to constrain the range of global P32 values that may exist in the competent portions of the basement rock within the South Reservoir.

5.3 Meager Creek Fault Model

The north-dipping Meager Creek Fault forms the southern surface boundary of the South Reservoir structural domain. Due to the presence of hot springs along the surface trace of the Meager Creek Fault, it is interpreted that the fault likely contains zones of higher permeability relative to the basement rock permitting upwelling of deep geothermal fluids to surface. Fault zones often develop two primary hydromechanical zones that run parallel to the fault plane, referred to as the core and the damage zone. The core typically consists of brecciated rock and gouge and is relatively impermeable, whereas the damage zone is characterized by highly fractured rock that is permeable relative to the host rock, providing conduits for fluid flow parallel to the fault plane (Gudmundsson 2011). Figure 5.10 is a conceptual model of fracture behaviour within the fault zone and surrounding host rock. It can be seen that the damage zone consists predominantly of fractures oriented parallel to the fault plane, and fracture intensity increases with increasing proximity to the fault core.

Slim hole M09-80D intersects the Meager Creek Fault between 500 – 575 m elevation, and is the only slim hole to penetrate the footwall of the Meager Creek Fault. Within the damage zone of the Meager Creek Fault, several shear and rubble zones were recorded in addition to reports of lost drilling fluid circulation (see appendix B). Based on the geomechanical log and temperature surveys of M09-80D, it is interpreted that the footwall of the Meager Creek Fault is comprised of competent quartz diorite, and heat transfer is dominated by conductive processes (NSBG 1982). Consequently, only the

hanging wall portion of the DFN model was populated with fractures as it is assumed that convective heat transfer does not occur across the Meager Creek Fault.

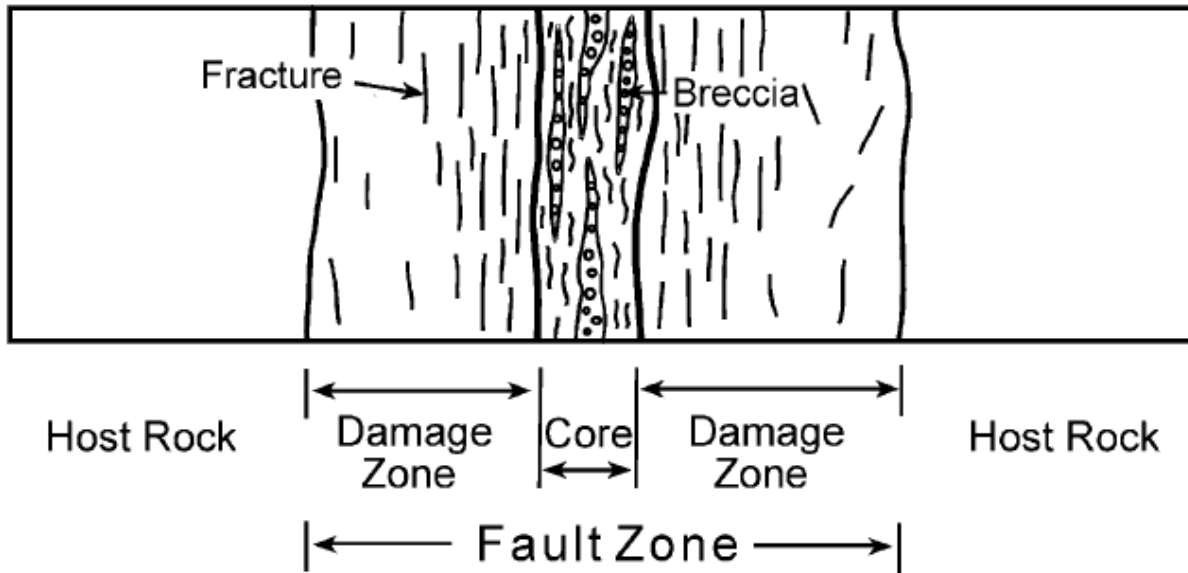


Figure 5.10 Conceptual model of the Meager Creek Fault permeable damage zone and impermeable core, from Gudmundsson (2004)

5.3.1 Model Boundaries and P32 Values for Individual Fracture Sets

The boundaries and sub-regions of the Meager Creek Fault model are the same as the Uniform Rock Mass model (see section 5.2.1). The Meager Creek Fault model includes a 100 m-wide damage zone that straddles the projected plane of the Meager Creek Fault. The Meager Creek Fault plane dips towards the north at 50° below horizontal, and strikes east-west. The projected location of the Meager Creek Fault and the associated 100 m-wide damage zone are shown in Figure 5.11.

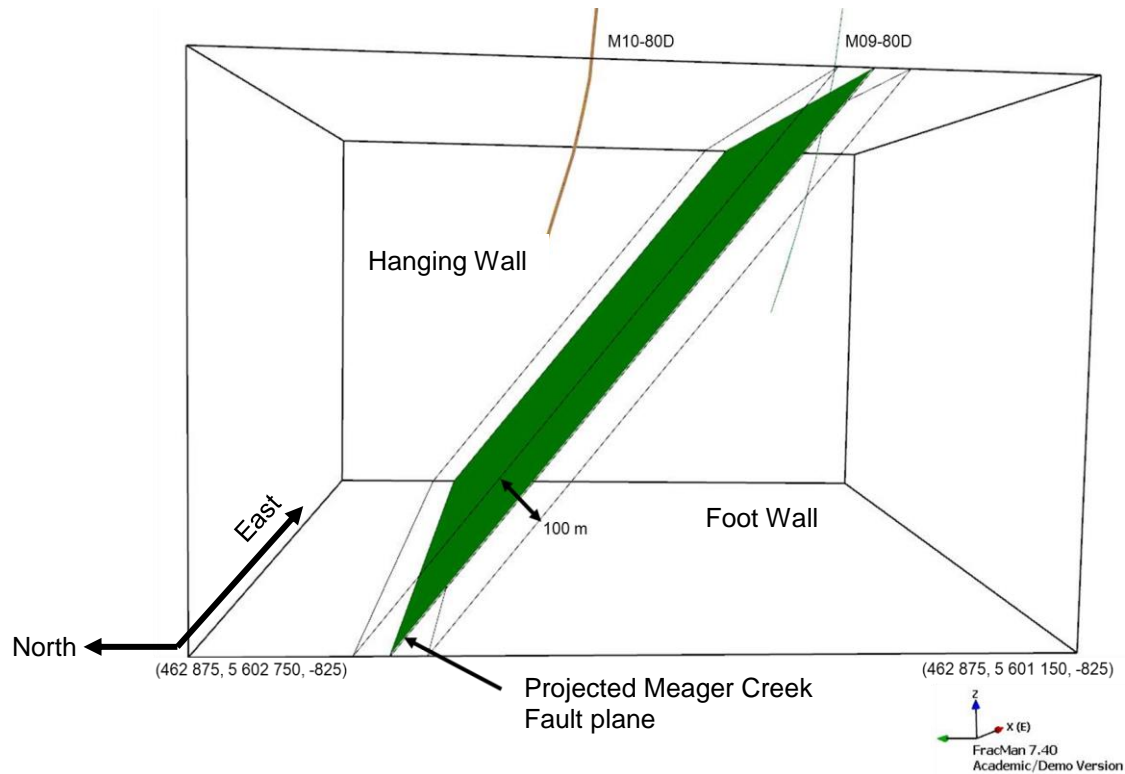


Figure 5.11 Model space for the bottom region of the Meager Creek Fault model. The green plane is the projected location of the Meager Creek Fault. Simulated fractures are limited to the hanging wall and fault damage zone regions of the model.

Similar to the Uniform Rock Mass model, a range of global P32 fracture intensity values between $0.05 - 0.5 \text{ m}^2/\text{m}^3$ were used to generate fractures within the basement rocks that comprise the hanging wall of the Meager Creek Fault. Weighted P32 values were calculated based on the relative occurrence of each fracture set, and are presented in Table 5.7.

Fracture set E, which shares a similar orientation to that of the Meager Creek Fault, is confined entirely to the fault damage zone following the conceptual model presented in Figure 5.10. Fracture set E was assigned a constant P32 of 0.3 m²/m³ for all of the global P32 fracture intensities tested.

Table 5.7 Weighted P32 values for individual fracture sets in the Meager Creek Fault model

SET NAME	RELATIVE OCCURENCE	GLOBAL P32 VALUES - HANGING / FOOT WALLS AND FAULT DAMAGE ZONE (m ² /m ³)				
		0.05	0.1	0.3	0.5	0.7
SET A	24.9%	0.01243	0.02487	0.07460	0.12433	0.17406
SET B	6.0%	0.00302	0.00604	0.01812	0.03021	0.04229
SET C	16.6%	0.00831	0.01661	0.04983	0.08306	0.11628
SET D	13.2%	0.00661	0.01322	0.03965	0.06609	0.09253
SET E	Damage Zone	0.30000	0.30000	0.30000	0.30000	0.30000
SET F	3.5%	0.00174	0.00348	0.01044	0.01740	0.02436
SET G	5.2%	0.00262	0.00524	0.01572	0.02621	0.03669
MISC	30.5%	0.01526	0.03052	0.09156	0.15260	0.21364

5.3.2 Cluster Analysis Results

Similar to the methodology used in the Uniform Rock Mass model, increasingly restrictive TFR filters were applied to DFN simulations in order to determine the percentage of transmissive fractures at which connected fracture networks begin to develop. Table 5.8 provides a comparison of fracture network connectivity statistics for DFN simulations based on the Uniform Rock Mass and Meager Creek Fault models assuming a constant global P32 equal to 0.5 m²/m³.

Table 5.8 Comparison of cluster analysis statistics from DFN simulations of the South Reservoir based on the Meager Creek Fault model

	P32	MIN. FRACTURE AREA (m ²)	TFR FILTER	NUMBER OF ITERATIONS	TOTAL NUMBER OF CLUSTERS	NUMBER OF FRACTURES PER CLUSTER				TOTAL FRACTURE AREA				CONNECTED FRACTURE P32			
						Average	StDev	Max	Min	Average (m ²)	StDev (m ²)	Max (m ²)	Min (m ²)	Average (m ² /m ³)	StDev (m ² /m ³)	Max (m ² /m ³)	Min (m ² /m ³)
Meager Creek Fault Model	0.5	10	100%	30	30	991,389	1,173	994,269	988,947	279,071,662	424,890	280,270,510	278,496,470	0.2272	0.0003	0.2282	0.2268
	0.5	10	30%	30	30	156,930	1,395	159,749	153,998	62,004,377	590,939	63,280,685	60,741,985	0.0506	0.0005	0.0517	0.0495
	0.5	10	25%	30	30	81,723	29,035	95,845	2,031	34,052,744	12,053,495	40,154,744	954,840	0.0306	0.0046	0.0334	0.0145
	0.5	10	20%	30	30	34,394	1,422	37,178	32,087	13,847,165	743,812	15,552,174	12,591,990	0.0185	0.0015	0.0212	0.0157
	0.5	10	15%	30	42	3,166	1,041	7,556	2,066	1,358,537	447,570	3,207,054	878,951	0.0176	0.0029	0.0263	0.0110
	0.5	10	10%	30	0	0	-	-	-	0	-	-	-	-	-	-	-
Uniform Rock Mass Model	0.5	10	100%	30	30	1,860,673	2,388	1,866,187	1,855,377	541,161,714	453,436	542,179,660	540,373,710	0.2113	0.0002	0.2117	0.2110
	0.5	10	30%	29	29	286,903	2,031	290,223	283,291	122,253,021	884,636	123,850,900	120,632,480	0.0478	0.0003	0.0484	0.0472
	0.5	10	25%	30	32	158,204	40,304	176,550	2,209	73,902,248	18,826,609	82,396,025	1,023,200	0.0306	0.0017	0.0323	0.0230
	0.5	10	20%	29	124	3,596	1,802	12,123	2,000	1,906,407	950,170	6,366,908	1,047,927	0.0129	0.0024	0.0188	0.0070
	0.5	10	15%	30	0	0	-	-	-	0	-	-	-	-	-	-	-

1. Clusters statistics are based on DFN simulations confined to the bottom region of the South Reservoir
2. Clusters are comprised of a minimum of 2000 connected fractures.

From the cluster statistics presented in Table 5.8, the following trends can be observed:

- The rate at which the size of the connected clusters decreases as the TFR cut-off limit is approached in the Meager Creek Fault model is more gradual compared to the Uniform Rock Mass model;
- Average connected P32 values of the connected clusters generated using the Meager Creek Fault model are higher than connected clusters generated using the Uniform Rock Mass model at similar TFR filters; and
- For a global $P32=0.5 \text{ m}^2/\text{m}^3$, the TFR cut-off limit falls from 20% to 15% using the Meager Creek Fault model, indicating that connected clusters will develop when fewer transmissive fractures are present.

The total number of fractures and total connected fracture area of individual clusters cannot be directly compared because the model volume over which fractures were generated in the Uniform Rock Mass model is roughly two times larger than that of the Meager Creek Fault model. This is because the Meager Creek Fault model volume consists only of the hanging wall and damage zone of the Meager Creek Fault, whereas the Uniform Rock Mass model generated fractures throughout the entire bottom sub-region.

5.3.2.1 Size and Distribution of Self-Connected Clusters

The relationship between TFR filter criteria and the size of connected clusters is similar to the results found from DFN simulations using the Uniform Rock Mass Model. As the percentage of transmissive to non-transmissive fractures in the model decreases, the

ratio of cluster volume to model volume decreases until a TFR cut-off limit is reached. The two curves in Figure 5.12 show the relationship between connected cluster size and the percentage of transmissive fractures in DFN simulations for the Uniform Rock Mass and Meager Creek Fault models for a global $P_{32} = 0.5 \text{ m}^2/\text{m}^3$.

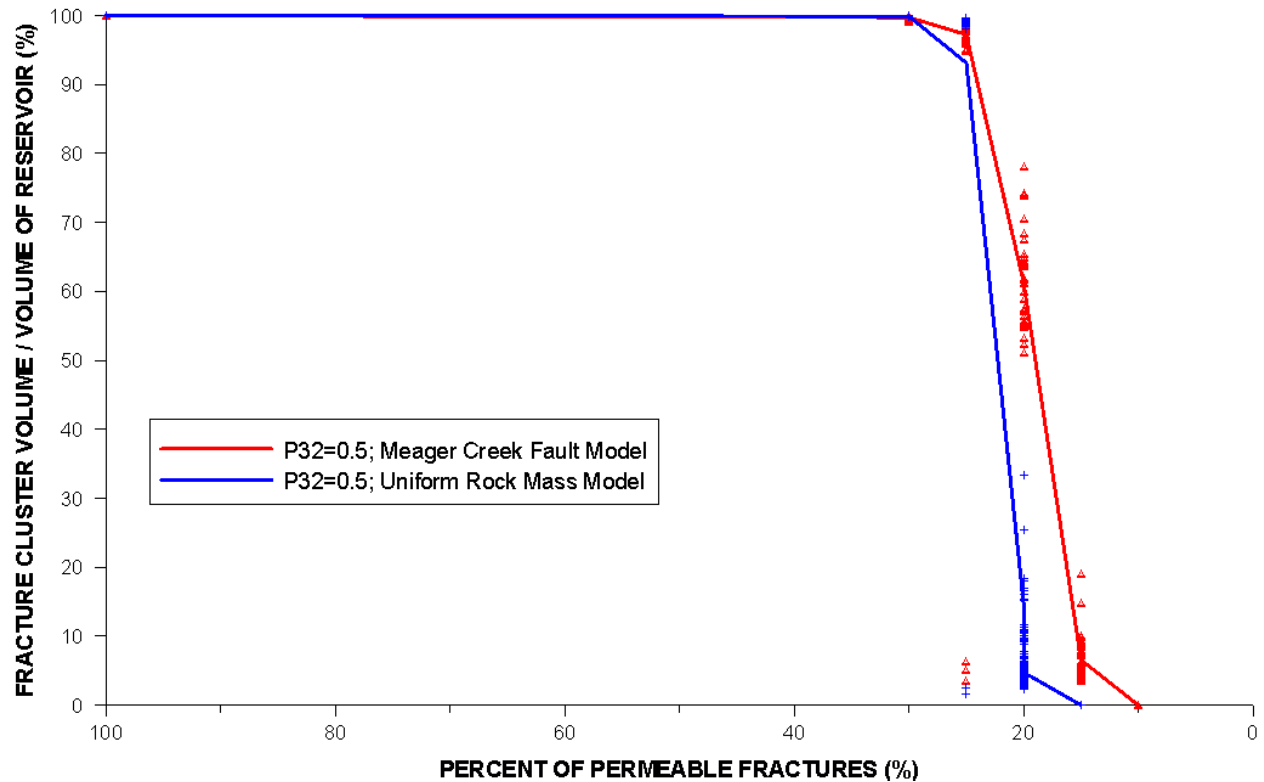


Figure 5.12 Comparison of connected cluster size as a function of TFR filter criteria for DFN simulations following the Meager Creek Fault and Uniform Rock mass models for a global $P_{32} = 0.5 \text{ m}^2/\text{m}^3$

It can be seen from Figure 5.12 that the size of the connected clusters that develop in the Meager Creek Fault model is greater than those that develop in the Uniform Rock Mass model for a constant TFR filter. The ratio of cluster volume to model volume in the Meager Creek Fault model decreases more gradually as the percentage of transmissive

to non-transmissive fractures in the model decreases. This behaviour is attributed to the higher volumetric fracture intensity associated with the fault damage zone, which continues to form connected fracture networks within the damage zone at lower TFR filters. Because the Meager Creek Fault extends across the entire model region, larger connected clusters are able to form at lower percentages of transmissive fractures. This results in a lowering of the TFR cut-off limit, which falls from 20% in the Uniform Rock Mass model to 15% in the Meager Creek Fault model.

The extent of connected fracture networks in the Meager Creek Fault model at the TFR cut-off limit is confined to the fault damage zone, and the areas immediately adjacent to the hanging wall-damage zone contact margin. Figure 5.13 shows the location of three different connected fracture networks that were generated from DFN simulations as the percentage of transmissive fractures approached the TFR cut-off limit. The limited extent of these fractures shows that the fault damage zone has a significant effect on the size and distribution of connected fracture networks that develop in low permeability rocks. For the purpose of geothermal well design, the likelihood of intersecting a network of connected fractures increases if drilling is oriented parallel to the Meager Creek Fault plane. The effect of well orientation on the number of fractures intersected is examined in greater detail in section 5.3.3.

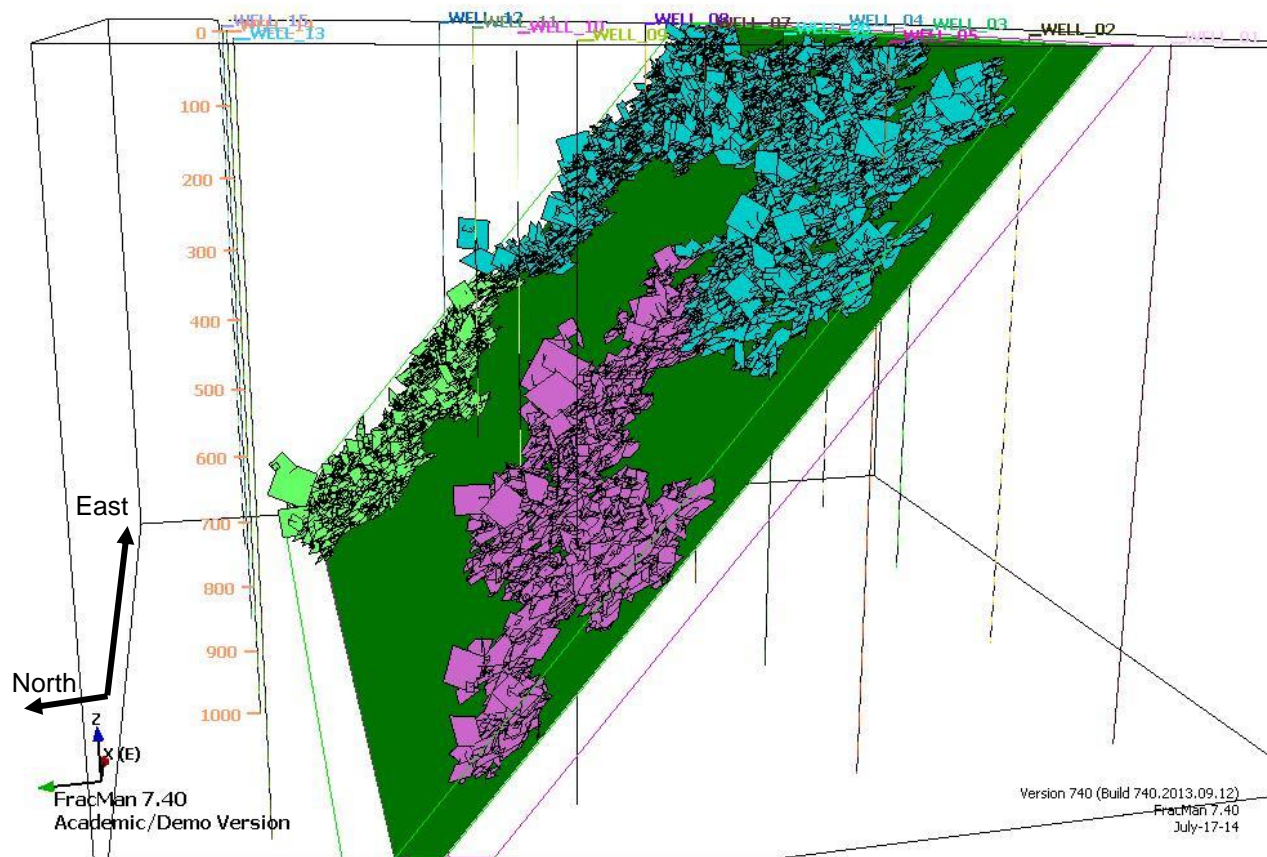


Figure 5.13 Development of three concentrated fracture networks surrounding the fault damage zone as the percentage of transmissive fractures approaches the TFR cut-off limit. The model shown is for a global $P32 = 0.5 \text{ m}^2/\text{m}^3$, and a TFR = 20%.

The Meager Creek Fault model predicts that the connected fracture networks that develop will have a slightly higher fracture density to compared to the connected fracture networks that develop in the Uniform Rock Mass model, as indicated by the connected fracture P32 values summarized in Table 5.8. This is reflective of the higher fracture intensity assigned to the fault damage zone.

The results from the cluster analysis indicate that the presence of regional faults have a significant impact on the size and distribution of the connected fracture networks. Therefore, the identification and characterization of the geomechanical properties of regional faults should be a priority of prefeasibility level site investigations so that their geomechanical properties can be properly characterized in DFN simulations.

5.3.2.2 Lost Circulation Zones and Elevation of Meager Creek Fault

Intervals encountered during drilling where fluid circulation was lost provide evidence that connected clusters may exist in portions of the hanging wall near the projected location of the Meager Creek Fault. Zones of lost circulation are the result of the drill string intersecting permeable fractures, which can be interpreted as the intersection of the drill string with a connected cluster. Figure 5.14 is a north-south cross-section showing the elevation of zones of lost circulation that were encountered during the drilling of slim holes in the South Reservoir. A projection of the Meager Creek Fault onto the cross-section indicates zones of lost circulation were encountered by M10-80D above the projected Meager Creek Fault Zone. M10-80D experienced significant deviation during drilling and did not intersect the Meager Creek Fault.

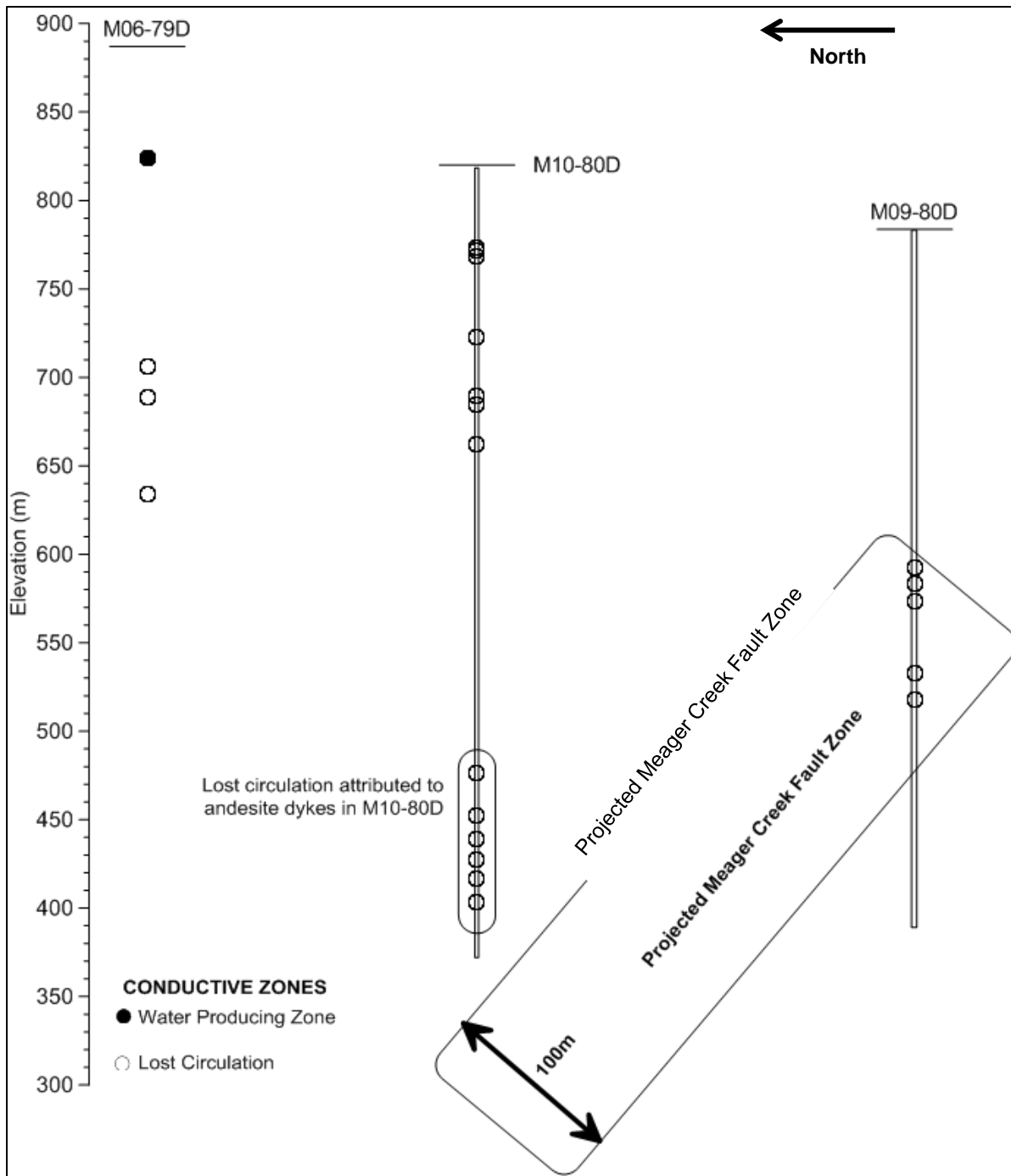


Figure 5.14 Cross-section of the South Reservoir, facing east. The elevation of lost drilling circulation zones encountered in M10-80D relative to the Meager Creek Fault support the Meager Creek Fault conceptual model.

Given the proximity of M10-80D to the projected location of the Meager Creek Fault and the tendency of connected fracture networks to be clustered along the Meager Creek Fault plane, the Meager Creek Fault model can be used to explain why past attempts to develop geothermal wells in the South Reservoir have been unsuccessful despite the presence of hot springs at surface along the Meager Creek Fault. If the percentage of transmissive fractures that exist in the South Reservoir is near the TFR cut-off limit, it is unlikely that slim holes other than M09-80D and M10-80D would have encountered any extensively connected fracture networks. This is because none of the slim holes completed in the South Reservoir penetrated the damage zone of the Meager Creek Fault below 500 m elevation.

5.3.3 Well Connectivity Analysis Results

Results from the well connectivity analysis indicate that the number of fractures intersected by a well is sensitive to the location and orientation of the well, specifically if the trajectory of the well intersects the damage zone of the Meager Creek Fault. An analysis of the number of fractures intersecting vertical wells shows that the likelihood of intersecting a network of connected fractures is dependent on the depth and location of the well. A similar analysis conducted using inclined wells shows that wells drilled parallel to the fault plane are more efficient at intersecting fractures that belong to connected fracture networks, even when the percentage of transmissive fractures is relatively low.

5.3.3.1 P10 of Connected Fractures in Vertical Wells

Twelve vertical sampling wells, Wells 5 – 16, were inserted into each DFN simulation. For each DFN simulation, the number of fractures intersected and the depth at which each fracture was intersected was recorded for each well. Summing the number of fractures intersected over depth intervals of 25 m, it was observed that the number of fractures intersected by a well is depth-dependent, which is not the case for the Uniform Rock Mass model. The collar coordinates of Wells 5 – 16 are summarized in Table 5.1, and the location of each well is shown in Figure 5.2.

Three DFN models generated following the Meager Creek Fault model are shown in Figure 5.15 to illustrate the impact of the fault damage zone on the number of fractures intersected by the vertical sampling wells. The three DFN models were generated assuming a global P32 of $0.5 \text{ m}^2/\text{m}^3$ and show the extent of the self-connected clusters that develop at TFR filters of 20% and 25%, as well as the case where no TFR filter is applied. The number of fractures intersected as a function of elevation for vertical Wells 6, 10, and 14 are shown below each model. Vertical Wells 6, 10, and 14 are aligned in a north-south direction parallel to the dip direction of the Meager Creek Fault. Wells 6 and 10 intersect the fault damage zone between elevations of -50 to -100 m and -500 to -550 m respectively, whereas Well 14 does not intersect the fault damage zone. From these plots, the following observations were made:

- If no TFR filter is applied, the number of fractures intersected in Well 14 is uniformly distributed across the entire length of the well, similar to what was observed in the Uniform Rock Mass model. In Wells 6 and 10, a significantly

higher number of fractures are intersected by the wells at elevations that coincide with the fault damage zone;

- At a TFR filter of 25%, the number of connected fractures intersected by Well 14 is very low, and these fractures are distributed over the entire length of the well. Conversely, connected fractures intersected by Wells 6 and 10 are concentrated near the fault damage zone;
- At a TFR filter of 20%, Well 14 no longer intersects any connected fractures, whereas Wells 6 and 10 continue to intersect fractures within the fault damage zone that belong to a connected cluster; and
- At TFR filters of 25% and 20%, it can be seen that connected fractures are intersected by Wells 6 and 10 in the areas immediately above the hanging wall-fault damage zone contact margin. This simulated distribution of connected fractures supports the observed correlation of deep permeable zones encountered during drilling to the projected location of the Meager Creek Fault presented in section 5.3.2.2.

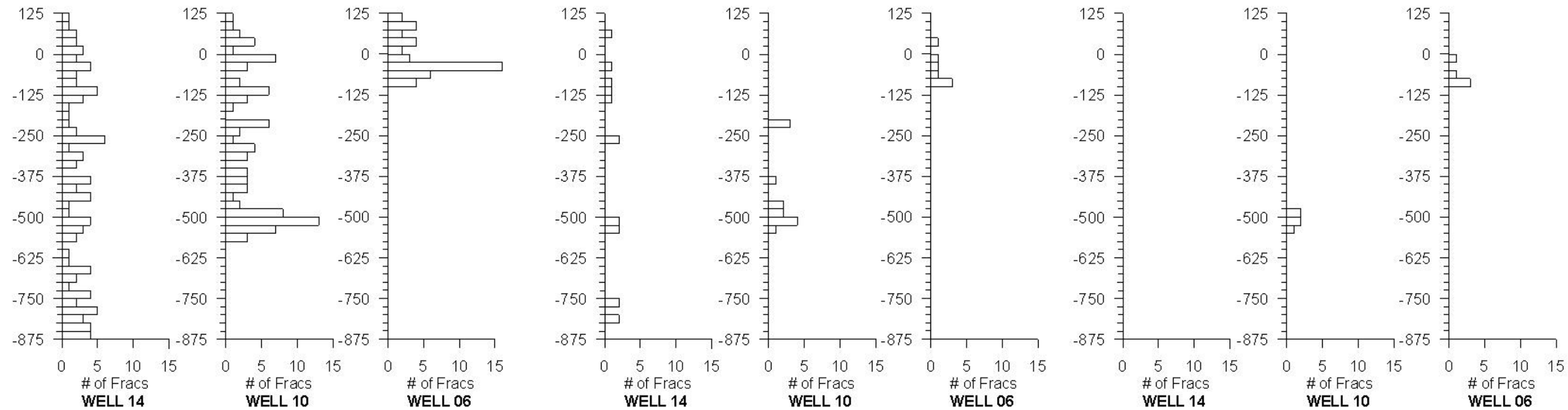
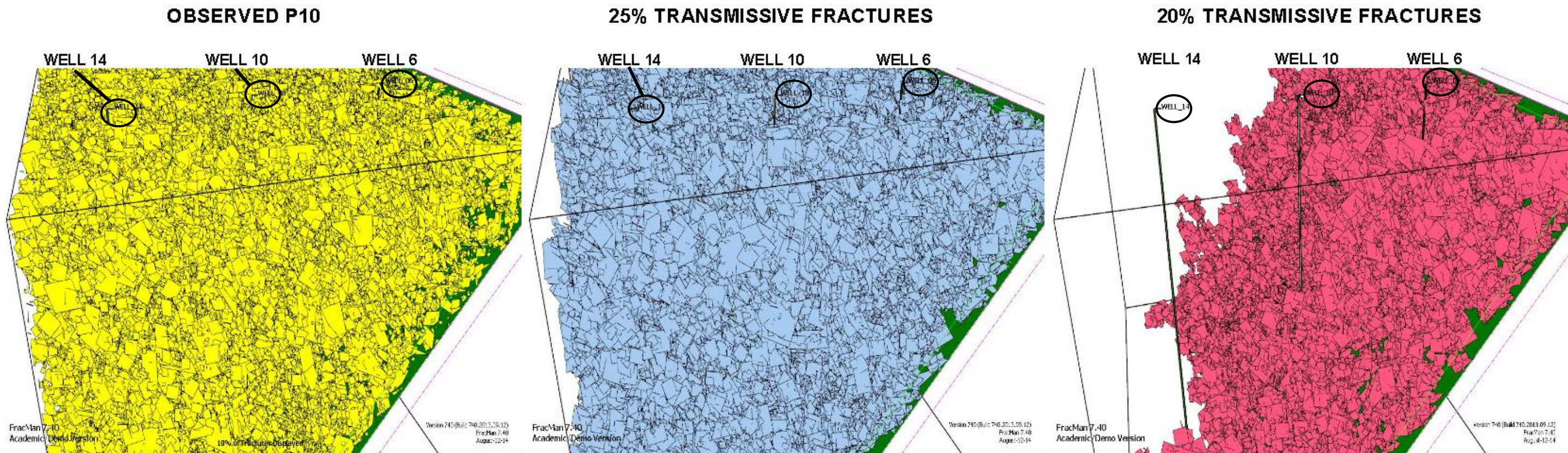


Figure 5.15 Number of observed and connected fractures intersected by vertical sampling wells as a function of depth at various TFR filters

5.3.3.2 P10 of Connected Fractures in Inclined Well

As the TFR cut-off limit is approached, connected fracture networks are confined to the fault damage zone and the portions of the hanging wall immediately adjacent to the fault damage zone. It follows that the likelihood of a geothermal well intersecting a network of connected fractures will decrease as the distance between the trajectory of the well and the fault damage zone increases. Sixteen inclined sampling wells were inserted into each DFN simulation in order to evaluate the effect of increasing the distance between well trajectories relative to the hanging wall-damage zone contact margin and the number of connected fractures intersected by each well. The coordinates of individual wells are summarized in Table 5.9, and the location and relative spacing between inclined wells is shown in Figure 5.16. Inclined wells were labelled Wells 61 – 76.

Table 5.9 Location and orientation of inclined wells used in well connectivity analyses for the Meager Creek Fault model

INCLINED WELLS											
Name	Easting	Northing	Trend (°)	Plunge (°)	Fault Zone Offset (m)	Name	Easting	Northing	Trend (°)	Plunge (°)	Fault Zone Offset (m)
WELL_61	463075	5601638	000	-50	0	WELL_69	463075	5601663	000	-50	25
WELL_62	463475	5601638	000	-50	0	WELL_70	463475	5601663	000	-50	25
WELL_63	463875	5601638	000	-50	0	WELL_71	463875	5601663	000	-50	25
WELL_64	464275	5601638	000	-50	0	WELL_72	464275	5601663	000	-50	25
WELL_65	463075	5601648	000	-50	10	WELL_73	463075	5601688	000	-50	50
WELL_66	463475	5601648	000	-50	10	WELL_74	463475	5601688	000	-50	50
WELL_67	463875	5601648	000	-50	10	WELL_75	463875	5601688	000	-50	50
WELL_68	464275	5601648	000	-50	10	WELL_76	464275	5601688	000	-50	50

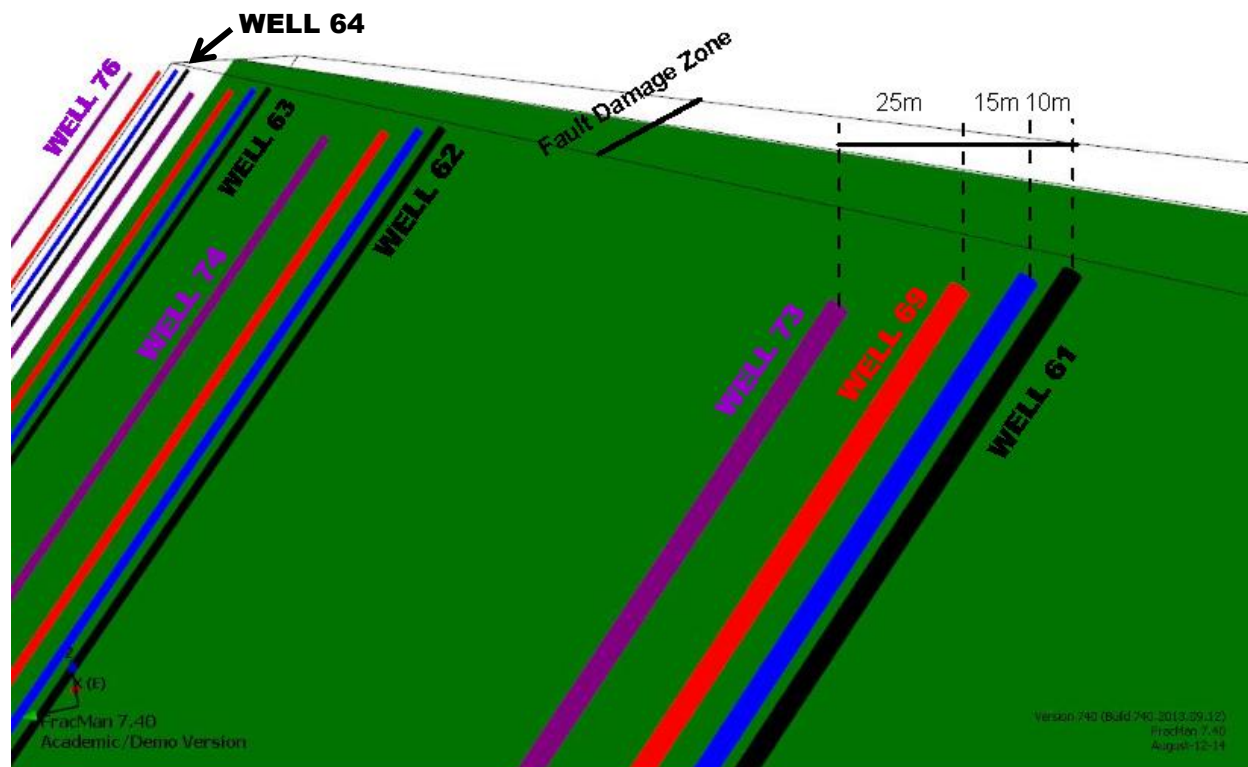


Figure 5.16 Location and relative spacing of inclined wells oriented parallel to the Meager Creek Fault plane

All of the inclined wells were oriented parallel to the Meager Creek Fault plane and have a total length of 500 m. Wells 61 – 64 are located along the hanging wall-fault damage zone contact margin. Wells 65 – 68, 69 – 72, and 73 – 76 are horizontally offset from the hanging wall-damage zone contact margin by 10 m, 25 m, and 50 m respectively. For each DFN simulation run, P10 for individual wells was calculated by dividing the sum of all the fractures intersected by the well length. Figure 5.17 is a plot of the average P10 for all sixteen inclined wells at TFR filters between 15 – 30%. The black, blue, red, and purple lines plotted in Figure 5.17 represent the average P10 values of

wells offset a distance of 0, 15, 25, and 50 m from the hanging wall-damage zone contact margin respectively.

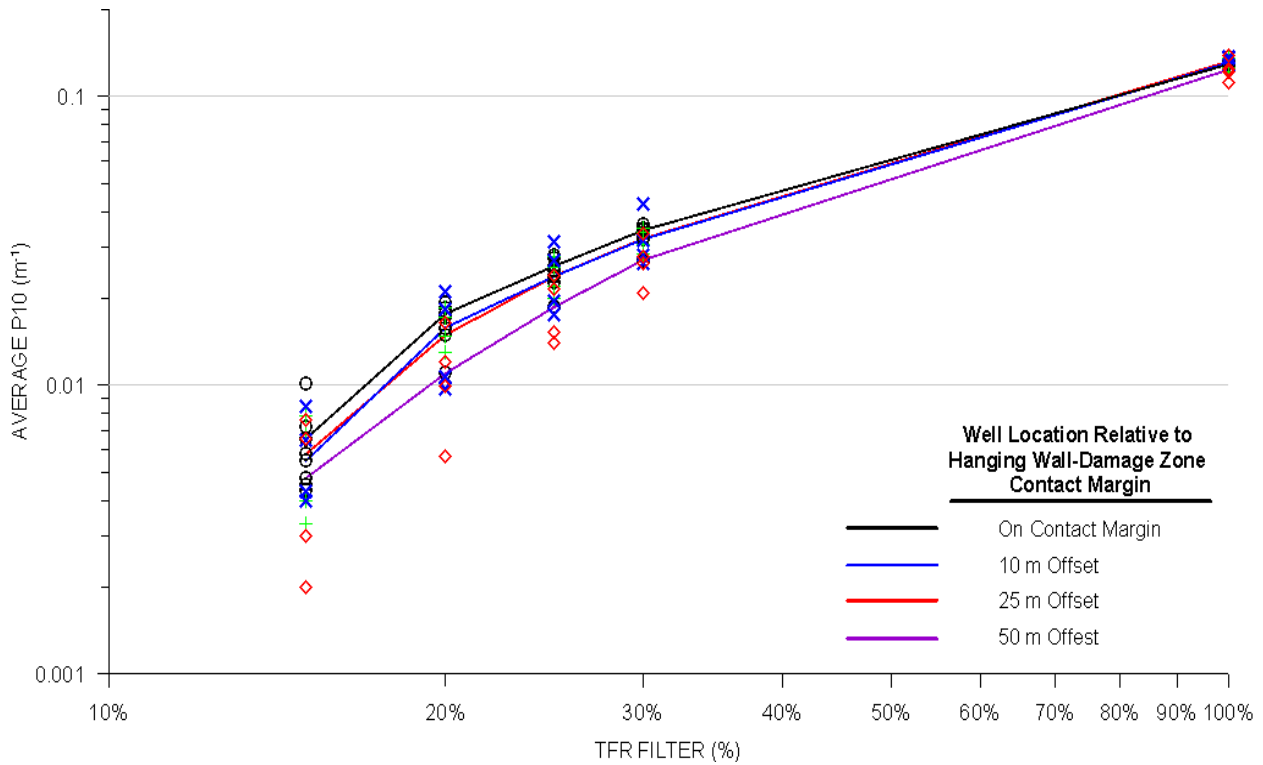


Figure 5.17 Average P10 of inclined wells as a function of distance from the hanging wall-damage zone contact margin and TFR filter

From Figure 5.17, it can be seen that as the percentage of transmissive fractures in the model approaches the TFR cut-off limit, the average P10 is greater for wells located on or close to the hanging wall-damage zone contact margin. As the percentage of transmissive fractures in the model increases, the average P10 values increase and converge until all fractures within the model are assumed to be transmissive. The fact that the average P10 for all of the inclined wells converges to a single value when no TFR filter is applied implies that the number of fractures intersected per meter for a well

oriented parallel to the Meager Creek fault plane and drilled within 50 m of the damage zone will be relatively constant. However, if only a small percentage of existing fractures have sufficient permeability to permit fluid circulation, then the number of transmissive fractures intersected by a well increases as the distance between the well trajectory and fault damage zone decreases.

The probability that either a vertical or inclined well intersects a connected fracture network at various TFR filters is presented in Table 5.10. The probability that a well intersects a connected fracture was determined by dividing the total number of instances that a particular well intersects at least one fracture that is part of a self-connected cluster by the total number of simulated DFN models. At the TFR cut-off limit, it can be seen that the probability of a vertical well that does not intersect the fault damage zone is equal to 0% (Wells 13 – 16), whereas wells that do intersect the fault damage zone (Wells 5 – 12) range between 0 and 64%, with an average probability of intersection of 30%. The sixteen inclined wells had a probability of intersection that ranged between 7 – 68%. Inclined wells located on the hanging wall-damage zone contact margin had an average probability of intersection of 43%. Inclined wells offset from the hanging wall-damage zone contact margin by 10 m, 25 m, and 50 m had an average probability of intersection of 40%, 38%, and 26% respectively.

Table 5.10 Probability of intersecting connected fracture networks and average P10 for both vertical and inclined wells

		TFR = 15%		TFR = 20%		TFR = 25%		TFR = 30%		NO TFR FILTER		
Well Name		Prob. Intersection	Avg. P10									
VERTICAL WELLS	WELL_05	25%	0.0036	83%	0.0043	100%	0.0063	100%	0.0079	100%	0.0388	
	WELL_06	64%	0.0031	93%	0.0056	100%	0.0085	100%	0.0097	100%	0.0408	
	WELL_07	21%	0.0022	93%	0.0058	100%	0.0103	100%	0.0124	100%	0.0439	
	WELL_08	0%	-	87%	0.0049	100%	0.0065	100%	0.0088	100%	0.0374	
	WELL_09	39%	0.0035	93%	0.0069	100%	0.0147	100%	0.0215	100%	0.0877	
	WELL_10	36%	0.0028	93%	0.0052	100%	0.0136	100%	0.0211	100%	0.0823	
	WELL_11	36%	0.0048	93%	0.0058	100%	0.0129	100%	0.0198	100%	0.0856	
	WELL_12	21%	0.0040	93%	0.0079	100%	0.0133	100%	0.0187	100%	0.0870	
	WELL_13	0%	-	37%	0.0022	100%	0.0111	100%	0.0197	100%	0.0884	
	WELL_14	0%	-	43%	0.0045	100%	0.0133	100%	0.0224	100%	0.0945	
	WELL_15	0%	-	30%	0.0027	100%	0.0104	100%	0.0183	100%	0.0910	
	WELL_16	0%	-	33%	0.0020	97%	0.0132	100%	0.0224	100%	0.0958	
	INCLINED WELLS	WELL_61	39%	0.0045	93%	0.0158	100%	0.0228	100%	0.0339	100%	0.1277
		WELL_62	68%	0.0101	93%	0.0173	100%	0.0251	100%	0.0326	100%	0.1274
		WELL_63	43%	0.0072	93%	0.0194	100%	0.0283	100%	0.0362	100%	0.1297
		WELL_64	21%	0.0043	93%	0.0185	100%	0.0275	100%	0.0351	100%	0.1328
WELL_65		29%	0.0040	93%	0.0130	100%	0.0201	100%	0.0287	100%	0.1218	
WELL_66		68%	0.0067	93%	0.0149	100%	0.0219	100%	0.0307	100%	0.1261	
WELL_67		43%	0.0078	93%	0.0185	100%	0.0279	100%	0.0351	100%	0.1340	
WELL_68		21%	0.0033	93%	0.0171	100%	0.0257	100%	0.0337	100%	0.1357	
WELL_69		25%	0.0043	93%	0.0107	100%	0.0176	100%	0.0264	100%	0.1282	
WELL_70		68%	0.0084	93%	0.0211	100%	0.0313	100%	0.0423	100%	0.1374	
WELL_71		50%	0.0064	93%	0.0183	100%	0.0270	100%	0.0319	100%	0.1280	
WELL_72		11%	0.0040	93%	0.0097	100%	0.0197	100%	0.0283	100%	0.1359	
WELL_73		14%	0.0030	80%	0.0099	97%	0.0153	100%	0.0208	100%	0.1217	
WELL_74		54%	0.0076	93%	0.0164	100%	0.0240	100%	0.0337	100%	0.1240	
WELL_75		29%	0.0065	90%	0.0121	100%	0.0215	100%	0.0278	100%	0.1119	
WELL_76		7%	0.0020	80%	0.0057	100%	0.0140	100%	0.0264	100%	0.1384	

Note: The total length of vertical and inclined wells is equal to 1000 m and 500 m respectively

If the percentage of fractures have sufficient permeability to allow for fluid circulation is increased from 15 to 25%, the likelihood of intersecting a connected fracture network is extremely likely for all well orientations tested. Given that the majority of slim holes drilled in the South Reservoir did not intersect highly permeable zones at depth, it is expected that the percentage of transmissive fractures at the site is near or below the TFR cut-off limit.

The correlation of deep permeable zones encountered during drilling to the projected location of the Meager Creek Fault presented in section 5.3.2.2 implies that the Meager Creek Fault model is a more appropriate conceptual model for the South Reservoir compared to the Uniform Rock Mass model. Given that the results from both the cluster and well connectivity analyses are strongly influenced by the damage zone associated with the Meager Creek Fault, it follows that future field investigations of the site should focus on the characterization of the location at depth, thickness, and fracture intensity within the damage zone of the Meager Creek Fault.

5.4 Estimation of Recovery Factors

The amount of recoverable thermal energy from the South Reservoir can be approximated using the total connected fracture area of the existing fracture networks that were determined from the cluster analyses completed in sections 5.2.2 and 5.3.2. Using equation 2.3, average recovery factors were calculated for the range of global P32 values and TFR filters used in DFN simulations based on the Uniform Rock Mass

and Meager Creek Fault models. The assumed values used in the recovery factor calculations are summarized in Table 5.11.

The assumed density and heat capacity of the basement granodiorites were taken from similar studies that evaluate the energy potential of geothermal resources (Grasby et al. 2011; Tester et al. 2006). The mean initial temperature of the reservoir rocks is conservatively assumed to be 150°C, which is 50°C cooler than interpreted temperatures of the shallow reservoir rocks (see section 3.5). Assuming a binary-cycle plant is used to convert the recoverable thermal energy to electricity, an abandonment temperature of 80°C was used in the recovery factor calculations. This abandonment temperature is representative of the lower-bound operating temperature of these systems (Grasby et al. 2011). The mean ambient surface temperature was calculated by averaging the historical monthly average temperatures over the past 30 years.

Table 5.11 Assumed values for recovery factor calculations

PARAMETER	VALUE	UNITS
Density of rock ^{1,2}	2550	kg/m ³
Heat capacity of rock ^{1,2}	1000	J/Kg °C
Mean initial reservoir rock temperature ³	150	°C
Mean rock temperature at abandonment ¹	80	°C
Mean ambient surface temperature ⁴	8.3	°C
Reservoir volume, Uniform Rock Mass model	2.560E+09	m ³
Reservoir volume, Meager Creek Fault model	1.228E+09	m ³

1. Tester et al. (2006)

2. Grasby et al. (2011)

3. NSBG (1980)

4. The Weather Network (2014)

The total fractured volume was calculated by multiplying the average total connected surface area by a factor of 2 metres. This method conservatively assumes that the recoverable heat can only come from a portion of the reservoir rocks that fall within a distance of 1-metre measured perpendicular to either side of the fracture planes that constitute the connected fracture network. Table 5.12 summarizes the total recoverable heat and the recovery factor, calculated using equation 2.3 for the range of connected surface areas for a range of global P32 values between 0.1 – 0.5 m²/m³.

A comparison of calculated recovery factors show that the connected fracture networks that develop in the Meager Creek Fault model stimulate a larger percentage of the reservoir volume compared to the Uniform Rock Mass model. However, even at recovery factors less than 1%, a significant amount of heat is still recoverable from the reservoir rocks. Although the amount of recoverable heat at low recovery factors is encouraging to prospective developers, it is important to recall that near the TFR cut-off limit, the probability that a well will intersect fractures belonging to connected fracture networks is low, and measures to enhance the connectivity and permeability of the fracture network may be required.

Table 5.12 Recovery factors based on calculated fractured rock volumes

	P32 (m²/m³)	TFR (%)	CONNECTED SURFACE AREA (m²)	FRACTURED VOLUME (m³)	RECOVERABLE HEAT¹ (J)	IN-PLACE HEAT (J)	RECOVERY FACTOR %
Uniform Rock Mass model	0.1	100%	4.27E+07	8.54E+07	1.53E+16	4.57E+17	3.3%
	0.1	95%	1.33E+06	2.65E+06	4.73E+14	4.57E+17	0.1%
	0.1	90%	0	0	0	4.57E+17	0%
	0.3	100%	4.10E+08	8.20E+08	1.46E+17	4.57E+17	32.0%
	0.3	75%	2.22E+08	4.44E+08	7.93E+16	4.57E+17	17.4%
	0.3	50%	1.23E+08	2.45E+08	4.37E+16	4.57E+17	9.6%
	0.3	45%	9.81E+07	1.96E+08	3.50E+16	4.57E+17	7.7%
	0.3	40%	6.24E+07	1.25E+08	2.23E+16	4.57E+17	4.9%
	0.3	35%	3.72E+06	7.44E+06	1.33E+15	4.57E+17	0.3%
	0.3	30%	1.40E+06	2.81E+06	5.01E+14	4.57E+17	0.1%
	0.3	25%	0	0	0	4.57E+17	0%
	0.5	100%	5.41E+08	1.08E+09	1.93E+17	4.57E+17	42.3%
	0.5	30%	1.22E+08	2.45E+08	4.36E+16	4.57E+17	9.6%
	0.5	25%	7.39E+07	1.48E+08	2.64E+16	4.57E+17	5.8%
	0.5	20%	1.91E+06	3.81E+06	6.81E+14	4.57E+17	0.1%
0.5	15%	0	0	0	4.57E+17	0%	
Meager Creek Fault Model	0.5	100%	2.791E+08	5.581E+08	9.963E+16	2.192E+17	45.4%
	0.5	30%	6.200E+07	1.240E+08	2.214E+16	2.192E+17	10.1%
	0.5	25%	3.405E+07	6.811E+07	1.216E+16	2.192E+17	5.5%
	0.5	20%	1.385E+07	2.769E+07	4.943E+15	2.192E+17	2.3%
	0.5	15%	1.359E+06	2.717E+06	4.850E+14	2.192E+17	0.2%
	0.5	10%	0	0	0	2.192E+17	0%

1. The amount of recoverable heat is compared to electricity production derived from geothermal energy for the top 10 geothermal producing countries. Values highlighted in green exceed the annual electricity production in the U.S.A, the top producer of electricity from geothermal energy in the world. Values highlighted in blue are less than the annual electricity production in the U.S.A., but greater than that of El Salvador, the tenth leading geothermal producer. Figures are based on 2010 electricity production figures (Grasby et al. 2011).

CHAPTER 6: CONCLUSION

The compilation of geological data at the Meager Creek site and subsequent DFN simulations fulfilled two of the three research objectives. The first research objective was to collect and interpret the available geomechanical and hydrogeological data that was collected from the Meager Creek site since the early 1970's. A comprehensive review of historical field investigations of the Meager Creek site is provided in section 3.6, and the geomechanical logs and stereonet plots contained in appendix B and appendix C respectively are the product of the data compilation process. Structural mapping completed by the author in 2013 was also added to the existing fracture database.

The second research objective was to identify the geometric fracture properties that have the greatest influence on fracture network connectivity predictions based on DFN simulations. The analyses completed in chapter 4 reveal that the field investigations conducted between 1974 and 1982 failed to collect several key fracture parameters. These key fracture parameters and their effect on fracture network connectivity predictions are summarized in section 6.1.

The third research objective was to develop a prefeasibility-level assessment of the overall extent and connectivity of the existing fracture network for the Meager Creek site. Although numerous DFN simulations were completed, a reasonably confident assessment of the overall connectivity of the existing fracture network could not be provided due to the limited availability of detailed fracture information. The conclusions

drawn from the results of cluster and well connectivity analyses conducted on DFN simulations of the South Reservoir are summarized in sections 6.2 and 6.3. Recommendations on how to reduce the uncertainty of fracture connectivity assessments through improved fracture sampling procedures are discussed in section 6.5.

6.1 Interpretation of Fracture Data

Analysis of the geological information collected from field investigations between 1974 and 1982 at the Meager Creek site revealed that the absence of certain fracture parameters result in a high degree of uncertainty associated with the fracture connectivity assessments. This section reviews the main findings from the interpretation of the available fracture data and summarizes the key fracture parameters that were not collected during the field investigations.

6.1.1 Key Findings from the Interpretation of Available Fracture Data

- The calculation of RQD for individual drill runs included fractures that were the product of stress-relief or stresses due to drilling (i.e. core discing). This leads to an under-estimation of rock competency and an over-estimation of the number of existing natural fractures at depth.
- It was found that P10 cannot be reasonably estimated from RQD measurements in highly competent rock. Consequently, the true fracture intensity within the basement rocks of the South Reservoir is highly uncertain.

- Andesite dykes may act as conduits for fluid flow. The inclusion of these features in future DFN simulations will have a significant effect on fracture network connectivity assessments. Characterization of these features (locations, dip, dip direction, permeability) should be prioritized.
- Uncorrected sampling biases led to a high degree of uncertainty regarding the fracture size distribution at the Meager Creek site. Sampling biases can be corrected if the type of mapping (line vs. window), the area of the mapping surface, orientation of the mapping surface, the number of ends visible for each fracture, and the minimum trace length are recorded at each mapping station.
- The most frequently observed fracture set within the South Reservoir is fracture set A, which dips towards the southwest at approximately 60°. Sub-vertical fractures belonging to fracture sets C and D are also prevalent in the South Reservoir. Fracture Sets C and D dip towards the east and south respectively.

6.1.2 Limitation of the Data Collection Program

- No fracture orientation measurements were collected from any of the slim holes completed in the South Reservoir. Without these measurements, the orientation of fractures at depth cannot be confirmed, and are assumed to be the same as the orientations observed in surface outcrops.
- The depth at which natural fractures were intersected by slim holes was not recorded. Consequently, fracture intensities at depth could not be estimated and limits the ability to make reasonable predictions of overall fracture network connectivity.

- The amount of structural mapping completed within the boundaries of the South Reservoir was reasonable, however the type of fracture information collected was limited. Ideally, a sufficient number of spacing, trace length, and aperture measurements should be collected so that statistically representative populations can be derived for individual fracture sets.
- Individual mapping stations were not surveyed. Consequently, structural information collected from surface mapping could not be corrected for biases that arise due to the orientation of fractures relative to the orientation of the mapping surface.

6.2 DFN Simulation Results - Uniform Rock Mass Model

Results from the DFN simulations based on the Uniform Rock Mass model provide insight into the fracture network connectivity of the massive crystalline granodiorites that constitute the majority of the reservoir rocks within the South Reservoir. The results from the cluster and well connectivity analyses are summarized, and the implications of these results on overall fracture network connectivity are discussed in this section.

6.2.1 Cluster Analysis

- The percentage of transmissive fractures observed at which connected fracture clusters no longer form is referred to as the TFR cut-off limit. The TFR cut-off limit is a function of global fracture intensity and fracture size distribution.
- As the TFR cut-off limit is approached, the size and density of connected clusters rapidly decreases to zero.

- Below a global P32 value of $0.1 \text{ m}^2/\text{m}^3$, no connected fractures will develop. A global P32 of $0.1 \text{ m}^2/\text{m}^3$ equates to simulated P10 values of 0.031 m^{-1} and 0.024 m^{-1} for drillholes M09-80D and M10-80D respectively. This is equal to approximately one fracture intersected every 35 m along the well trajectory.
- The size and density of a connected fracture network is highly sensitive to the fracture size distribution of individual fracture sets. Sensitivity analyses showed that the connected clusters that develop at the TFR cut-off limit have a greater average number of fractures and connected surface area per cluster when the mean effective radius is doubled. Also, the TFR cut-off limit fell from 35% to 20%, indicating that fracture networks will develop at lower global fracture intensities.

6.2.2 Well Connectivity Analysis

- The number of fractures intersected by a well does not depend on the location of individual well locations, but does depend on well orientation. The insensitivity of the number of fractures intersected to well location in the Uniform Rock Mass model is due to the fact that fracture properties are equally distributed over the entire South Reservoir.
- At the TFR cut-off limit, on average 1% of all fractures intersected by a vertical well will belong to an extensive connected fracture network.
- The probability of intersecting a connected fracture network is substantially higher for simulated wells oriented perpendicular to the strike of fracture set A. The difference in the number of connected fractures intersected by oriented wells compared to vertical wells is more pronounced at the TFR cut-off limit. For a

global P32 of $0.5 \text{ m}^2/\text{m}^3$, a well oriented perpendicular to fracture set A is expected to intersect a fracture that is part of a connected fracture network every 38 m compared to 2,400 m for a vertical sampling well at the TFR cut-off limit.

- There is a poor correlation between simulated and calculated P10 for the range global P32 values tested. The poor correlation is due to the improper calculation of RQD during drilling and the inability to estimate P10 from RQD measurements in highly competent rock.

6.3 DFN Simulation Results - Meager Creek Fault Model

The presence of hot springs along the surface trace of the Meager Creek Fault infers that the fault likely contains zones of higher permeability relative to the basement rocks which permits upwelling of deep geothermal fluids from depth to the surface. The Meager Creek Fault model incorporated a 100 m-wide fault damage zone, located parallel to the projected fault plane. The results from the cluster and well connectivity analyses completed on DFN simulations based on the Meager Creek Fault model are compared to the results from the Uniform Rock Mass model, and the implications of these results on overall fracture network connectivity are discussed in this section.

6.3.1 Cluster Analysis

- The average P32 of the connected fracture networks generated using the Meager Creek Fault model are higher than those generated using the Uniform Rock Mass model at similar TFRs.

- The TFR cut-off limit falls from 20% to 15% at a global $P32=0.5 \text{ m}^2/\text{m}^3$ indicating that the presence of a fault zone allows for the formation of extensive connected fracture networks when fewer transmissive fractures are present.
- A review of drilling logs indicates that recorded intervals at which drilling fluid circulation was lost in slim holes M09-80D and M10-80D are likely related to the Meager Creek Fault. This data supports the Meager Creek Fault conceptual model, and implies that a permeable fracture network that extends parallel to the Meager Creek Fault may exist.
- The presence of a highly fractured damage zone associated with the Meager Creek Fault has a large effect on the size and location of connected fracture clusters generated from DFN simulations. Low-permeability rock masses such as the basement granodiorites of the South Reservoir are more likely to develop localized connected fracture clusters at the contact margin between the host rock and the fault damage zone.

6.3.2 Well Connectivity Analysis

- The number of fractures intersected by a well is dependent on the trajectory of the individual wells, specifically the total length of the well that is in close proximity to the fault damage zone.
- When the percentage of permeable fractures in the DFN simulations approach the TFR cut-off limit, it was shown that the connected fracture networks are only intersected by vertical wells that penetrate the areas immediately above the hanging wall-fault damage zone contact margin. This simulated distribution of

connected fractures is similar to the observed correlation of deep permeable zones encountered during drilling to the projected location of the Meager Creek Fault.

- On average, inclined wells drilled within 50 m of the hanging wall-damage zone contact margin will intersect the same number of fractures per metre. However, as the ratio of transmissive to non-transmissive fractures approaches the TFR cut-off limit, the number of connected fractures intersected by wells near the hanging wall-damage zone contact margin is significantly higher than wells located 50 m from the contact margin.
- The probability a connected fracture network would be intersected by vertical and inclined wells was determined using DFN simulations with a global $P_{32} = 0.5 \text{ m}^2/\text{m}^3$ and a TFR filter = 15%.
 - Vertical wells that did not intersect the fault damage zone had a 0% change of intersecting a connected fracture network.
 - Vertical wells that intersected the fault damage zone had a probability of intersection that ranged between 0 – 64%, with an average probability of intersection of 30%.
 - The sixteen inclined wells had a probability of intersection that ranged between 7 – 68%. Inclined wells located on the hanging wall-damage zone contact margin had an average probability of intersection of 43%. Inclined wells offset from the hanging wall-damage zone contact margin by 10 m, 25 m, and 50 m had an average probability of intersection of 40%, 38%, and 26% respectively.

- Given that the majority of slim holes drilled in the South Reservoir did not intersect highly permeable zones at depth, it is expected that the percentage of transmissive fractures in the South Reservoir is near or below the TFR cut-off limit.

6.4 Assumptions and Limitations of the DFN Simulation Results

- Connected clusters required a minimum of 2000 fractures to be counted. The reported average cluster sizes will change if the minimum connected fracture count is changed.
- The fracture size distribution was derived from trace length measurements taken from mapping stations located in the North Reservoir structural domain. This was required due to the absence of trace length measurements in the South Reservoir.
- TFR ratings were distributed uniformly over all fractures in the model space. The size and extent of connected clusters will differ significantly if fractures are assigned TFRs based on different distributions.

6.5 Recommendations for Improving Fracture Network Connectivity Estimates

The amount of geological information available for prefeasibility-level geothermal projects is often limited. This limitation leads to greater uncertainty in regards to the future productivity of a prospective geothermal site and lower confidence in connectivity estimates derived from DFN models. It is recommended that the collection of the following hydrogeological and structural data be prioritized during prefeasibility-level

field investigations to facilitate fracture network connectivity assessments using DFN modelling.

6.5.1 Hydrogeological Field Data

There are many sources of hydrogeological data that provide insight into the structural controls that affect fluid flow in fractured media. Hydrogeological characterization studies of fractured rock (Cohen 1995) have found that the volume and direction of fluid flow is controlled by a small percentage of fractures that intersect a well. It follows that well-designed hydrogeological data collection programs can be more efficient in identifying and characterizing highly conductive fractures and reduce the overall exploration costs.

Drilling condition reports recorded by the drill operator may contain information that can be used to infer the location of highly conductive fractures. Depending on the drilling method used, the sudden loss of mud circulation or increased fluid return to surface may indicate that a highly conductive zone has been encountered. Monitoring the volume of fluid used, produced, or returned to surface during drilling is more efficient and effective at inferring highly conductive fractures/zones compared to a detailed structural analysis of intact core or down-hole geophysical surveys (Cohen 1995).

It was found that the percentage of transmissive to non-transmissive fractures is an important parameter when estimating overall fracture network connectivity. Borehole flow profiling is an effective method for identifying conductive fractures and estimating

fracture transmissivities. The use of heat-pulse or impeller flow meters can be used to identify conductive fractures and determine the direction of flow within a borehole under natural and hydraulically stressed conditions. Fluid conductivity profiling is another borehole profiling method which can be used to identify transmissive fractures. Deionized water is pumped into a borehole to displace the formation water. Once the formation water has been displaced, a logging tool that is equipped with an electrical conductivity, pH, and temperature probe is run down the borehole. Plots of pH and electrical conductivity versus depth can be used to identify highly conductive zones.

Once the locations of highly conductive fractures/zones have been identified, they can be targeted for packer testing. Packer testing can be used to estimate transmissivities of single fractures or fracture zones using a straddled packer assembly, or bulk formation properties using an open-ended packer configuration. In the case of geothermal reservoirs, specialized packers are required due to the high temperatures at depth (Armstead and Tester 1987). Due to the relatively high cost and time required, targeted packer testing may not be possible at the prefeasibility level.

6.5.2 Structural Mapping

Structural mapping of exposed rock outcrops is an important source of fracture information which can be used to assess the spatial characteristics of existing fracture networks. A description of mapping methods and a summary of basic fracture information required for rock mass characterization is provided by Call et al. (1976).

The structural mapping program completed at the Meager Creek site contained deficiencies which limited the ability to constrain fracture network connectivity estimates derived from DFN simulations of the basement granodiorites within the South Reservoir. Carefully designed structural mapping programs can easily eliminate these deficiencies and greatly improve confidence in fracture network connectivity estimates.

A low-degree of confidence is attributed to the fracture size distributions derived from populations of measured trace lengths. Populations of measured trace lengths must be corrected for several types of sampling biases (see section 2.2.1.2). The importance of correcting for sampling biases was demonstrated by showing the sensitivity of fracture network connectivity estimates to fracture size distributions (see Figure 5.6). A higher degree of confidence could have been assigned to fracture network connectivity estimates of the South Reservoir if the following information was collected at each mapping station in addition to trace length measurements:

- Orientation of the mapping station (dip/dip direction of the mapped surface);
- The type of sampling method used (line vs. window mapping). In the case of line mapping, the orientation and length of the sampling line should be recorded. For window mapping, the total area and shape of the window (rectangle, square or circular) should be recorded;
- The minimum trace length that was measured;
- The number of fractures that extend beyond the boundaries of the mapping station; and
- The number of observable fracture termination points, if any, for each fracture.

The accuracy of fracture measurements collected from conventional mapping surveys have practical limitations related to the physical ability of an individual to measure large or inaccessible fractures. Digital fracture surveys using LiDAR or photogrammetry have the advantage of improving the accuracy of large trace length and spacing measurements, and allow for the characterization of fractures of remote or inaccessible surface outcrops. Digital fracture surveys have been shown to be effective in close-range applications, and can overcome some of the practical limitations of conventional mapping (Sturzenegger and Stead 2009). The use of these technologies can greatly improve the confidence in fracture network connectivity assessments by reducing sampling biases and measurement errors associated with conventional mapping techniques.

6.5.3 Geotechnical Drilling

Assessment of the geometric properties of fractures at depth is achieved through the analysis of core samples or surveys of open borehole walls. The analysis of fracture properties at depth is essential for estimating fracture network connectivity of geothermal reservoirs, as fracture properties observed in surface outcrops may not be representative of the characteristics of the fracture network at depth. The slim hole drilling program failed to record the depth of intersection of natural fractures encountered in each slim hole and did not collect any fracture orientation information (dip/dip direction). The absence of these two fracture parameters limited the ability to constrain the range of fracture network connectivity estimates.

An understanding of the relationship between fracture intensity and depth is essential for estimating fracture network connectivity of geothermal reservoirs. If linear fracture intensity (P10) can be estimated over several boreholes, the volumetric intensity (P32) can be inferred. Verification that simulated DFN models produce fracture distributions that match observed P10 values is also required before any reliable estimate of fracture network connectivity can be made.

All of the slim holes drilled in the South Reservoir were completed using skid-mounted diamond drill rigs. Core samples were collected after each drill run and were logged for several geological properties including RQD. It was found that an insufficient number of reliable linear fracture intensity measurements were recorded, and that they could not be derived from RQD measurements (section 4.1.4). P10 values can be easily calculated if the depth at which individual fractures were intersected by each slim hole is recorded. Given that RQD was calculated on all of the retrieved core samples, it is clear that the depths of individual fractures could have been easily recorded.

The fracture orientation measurements at depth can be achieved through the orientation of core samples using specialized core orientation tools or acoustic/optical televiewer surveys of the open borehole wall. These methods introduce additional costs to the drilling program, however they represent the only option for direct measurement of the fractures in a geothermal reservoir (Huenges 2010). The collection of fracture orientation measurements are further complicated by the high temperatures encountered during geothermal drilling, as down-hole instrumentation often have a

maximum operation temperature of approximately 70°C. Some success has been achieved by running specialized acoustic televiewers that have an operational temperature up to 125°C at the Newcrest Lihir gold mine, where subsurface temperatures up to 230°C have been recorded (Szymakowski 2011). Fracture orientations were collected at depths where the steady-state subsurface temperature was greater than 125°C by circulating cold surface water through the borehole immediately prior to deploying the acoustic televiewer.

6.6 Recommendations for Future Work

Recommendations for future work include revised detailed structural mapping of exposed outcrops in the South Reservoir and East of Camp Fault structural domains, retrieval of core photos/core samples collected during exploratory slim hole drilling prior to 1982, and the retrieval of geomechanical and hydrogeological information collected from test wells drilled after 1982.

Improved characterization of fracture sets can be achieved by revisiting the outcrops mapped in 1980 and 1981 and applying the more rigorous structural mapping methodology described in section 6.5.2. This will result in more refined DFN simulations and improved confidence in fracture network connectivity assessments.

Engineering reports have stated that core was retrieved and retained from the initial slim hole drilling program that ran from 1974 to 1982. This core should be relocated, and fracture frequency and RQD should be measured, ensuring that mechanical or drilling-

induced fractures are not included in the determination of these measures of rock competency. Fracture frequency and RQD can be estimated from core photos if the actual core samples cannot be retrieved. The author's attempts to locate core samples/photos were unsuccessful.

Feasibility-level production drilling was completed between 1982 and 2004. The information collected from these holes is proprietary, and was not available for this analysis. The geomechanical and hydrogeological information collected from these wells may provide significant insight into the connectivity of the existing fracture network at the Meager Creek site, and may be useful for calibrating DFN model predictions.

These recommendations for future work do not require the deployment of costly drilling or geophysical equipment, and would provide a significant amount of geomechanical and hydrogeological data which can be used to revise the existing DFN models of the Meager Creek site. Connectivity assessments of these revised DFN models could then be used to determine if further production well drilling is likely to intersect a connected fracture network, or if fracture network enhancement measures would be required to successfully develop the site.

REFERENCES

- Allen, D., M. Ghomshei, T. Sadlier-Brown, A. Dakin, and D. Holtz. 2000. "The Current Status of Geothermal Exploration and Development in Canada." In *Proceedings World Geothermal Congress 2000*, 55–58. Kyushu-Tohoku, Japan.
- Armstead, H., and J. Tester. 1987. *Heat Mining*. New York: E. & F.N. Spon Ltd.
- B.C. Hydro. 1982. "Meager Creek Mapping Program - 1981". Vancouver, BC.
- B.C. Hydro. 1985. "Meager Creek Project - Report on Activities 1983/84 and 1984/85 Volume 1". Vancouver, BC.
- Baecher, G., and N. Lanney. 1978. "Trace Length Biases in Joint Surveys." In *The 19th U.S. Symposium on Rock Mechanics (USRMS)*, 56–65. Reno, Nevada.
- Baecher, G., N. Lanney, and H. Einstein. 1977. "Statistical Description of Rock Properties and Sampling." In *The 18th U.S. Symposium on Rock Mechanics (USRMS)*. Golden, CO.
- Baecher, Gregory B. 1983. "Statistical Analysis of Rock Mass Fracturing." *Journal of the International Association for Mathematical Geology* 15 (2) (April): 329–348. doi:10.1007/BF01036074.
- Barbier, E. 2002. "Geothermal Energy Technology and Current Status : An Overview." *Renewable and Sustainable Energy Reviews* 6 (1-2): 3–65. doi:10.1016/S1364-0321(02)00002-3.
- Barton, C. 1977. "Geotechnical Analysis of Rock Structure and Fabric in CSA Mine NSW". 24. Applied Geomechanics Technical Paper. Australia.
- Barton, C. 1978. "Analysis of Joint Traces." In *The 19th US Symposium on Rock Mechanics (USRMS)*, 38–41. Reno, Nevada.
- Beardsmore, G., and J. Cull. 2001. *Crustal Heat Flow: A Guide to Measurement and Modelling*. Cambridge University Press. Cambridge: Cambridge University Press. doi:10.1017/S0016756803218021.
- Billaux, D., J.P. Chiles, K. Hestir, and J. Long. 1989. "Three-Dimensional Statistical Modelling of a Fractured Rock Mass—An Example from the Fanay-Augères Mine." *International Journal of Rock Mechanics and Mining Sciences & Geomechanics Abstracts* 26: 281–299. doi:10.1016/0148-9062(89)91977-3.

- Brady, B., and E. Brown. 2004. *Rock Mechanics: For Underground Mining*. 3rd ed. Kluwer, Dordrecht: Springer.
- Bridges, M. 1975. "Presentation of Fracture Data for Rock Mechanics." In *The 2nd Australian-New Zealand Conference on Geomechanics*, 144–148. Brisbane, Australia.
- Call, R., J. Savely, D. Nicholas, and Allen and Holt Inc. Pincock. 1976. "Estimation of Joint Set Characteristics from Surface Mapping Data." In *The 17th U.S. Symposium on Rock Mechanics (USRMS)*. Snow Bird, UT.
- Cohen, A. 1995. "Hydrogeologic Characterization of Fractured Rock Formations: A Guide for Groundwater Remediators Report LBL-38142." *University of California, Berkeley, USA*. Berkeley, California.
- Decker, J., and M. Mauldon. 2006. "Determining Size and Shape of Fractures from Trace Data Using A Differential Evolution Algorithm." In *The 41st U.S. Symposium on Rock Mechanics (USRMS)*. Golden, Colorado.
- Deere, D. 1964. "Technical Description of Rock Cores for Engineering Purposes." *Rock Mechanics Rock Engineering* 1 (1): 17–22.
- Dershowitz, W. 1984. "Rock Joint Systems". Cambridge, Massachusetts: M.I.T.
- Dershowitz, W., and H. Einstein. 1988. "Characterizing Rock Joint Geometry with Joint System Models." *Rock Mechanics and Rock Engineering* 21 (1): 21–51. doi:10.1007/BF01019674.
- Dienes, J. 1979. "On the Inference of Crack Statistics from Observations On An Outcropping." In *The 20th US Symposium on Rock Mechanics (USRMS)*, 259–263. Austin, Texas.
- Doe, T. 2010. "Fractured Bedrock Field Methods and Analytical Tools". Vol. I. Burnaby, BC.
- Ghomshei, M. 2010. "Canadian Geothermal Power Prospects." In *Proceedings of the World Geothermal Congress 2010*, 5. Bali, Indonesia.
- Ghomshei, M., K. MacLeod, S. Sanyal, and A. Ryder. 2006. "Overview of the First Canadian Geothermal Power Project: South Meager Creek, British Columbia." In *Proceedings of the Power-Gen International Conference*, 10. Las Vegas, NV.
- Ghomshei, M., S. Sanuyal, K. MacLeod, R. Henneberger, A. Ryder, J. Meech, and B. Fairbank. 2004. "Status of the South Meager Geothermal Project BC, Canada:

- Resource Evaluation and Plans for Development.” *Geothermal Resources Council Transactions* 28: 339–344.
- Ghomshei, M., and J. Stauder. 1989. “Brief Review of the Meager Creek Geothermal Project: A Second Look at the Data.” *Geothermal Resources Council Bulletin* 18 (7): 3–7.
- Golder Associates Inc. 2011. “FracMan User’s Manual Release 7.4”. Golder Associates Inc.
- Grasby, S. E., D. M. Allen, S. Bell, Z. Chen, G. Ferguson, A. Jessop, M. Ko, et al. 2011. “Geothermal Energy Resource Potential of Canada.” doi:10.4095/288745.
- Gudmundsson, A. 2004. “Effects of Young’s Modulus on Fault Displacement.” *Comptes Rendus Geoscience* 336 (1) (January): 85–92. doi:10.1016/j.crte.2003.09.018.
- Gudmundsson, A 2011. *Rock Fractures in Geological Processes*. Cambridge, UK: Cambridge University Press.
- Huenges, E. 2010. *Geothermal Energy Systems*. Edited by E. Huenges. Wiley-VCH.
- International Society for Rock Mechanics, Commission on Standardization of Laboratory and Field Tests. 1978. “Suggested Methods for the Quantitative Description of Discontinuities in Rock Masses.” *International Journal of Rock Mechanics and Mining Sciences & Geomechanics Abstracts* 15 (6): 319–368.
- Jamieson, G. 1981. “A Preliminary Study of the Regional Groundwater Flow in the Meager Mountain Geothermal Area, British Columbia”. University of British Columbia.
- Jamieson, G., and R. Freeze. 1982. “Determining Hydraulic Conductivity Distributions in a Mountainous Area Using Mathematical Modeling.” *Ground Water* 20 (2): 168–177.
- Jessop, A., M. Ghomshei, and M. Drury. 1991. “Geothermal Energy in Canada.” *Geothermics* 20 (5/6): 369–385.
- Jing, L., and J. Hudson. 2002. “Numerical Methods in Rock Mechanics.” *International Journal of Rock Mechanics and Mining Sciences* 39 (4): 409–427.
- Kulatilake, P. 1993. “Application of Probability and Statistics in Joint Network Modelling in Three Dimensions.” In *Proceedings of the Conference on Probabilistic Methods in Geotechnical Engineering*, 63–87. Canberra, Australia.

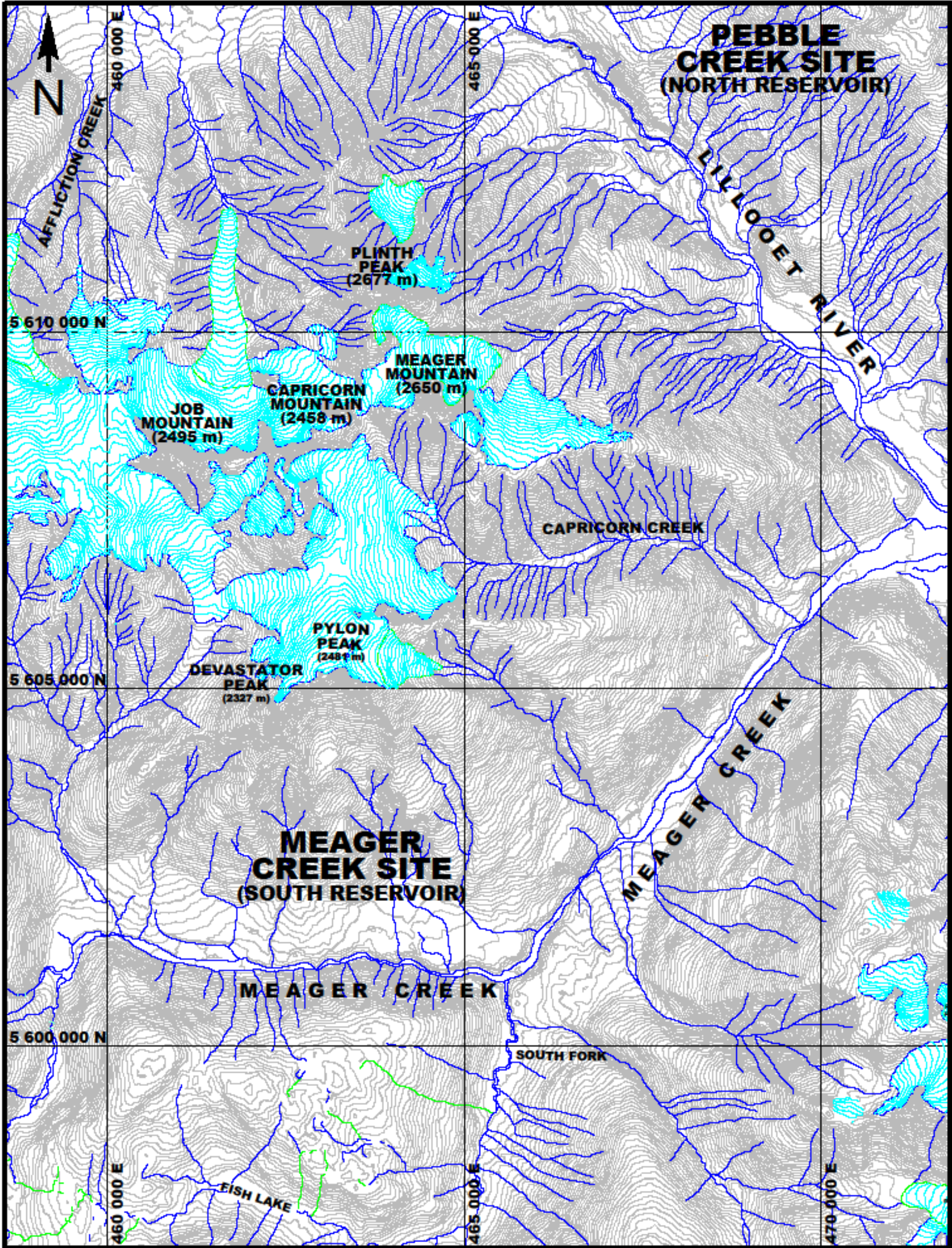
- Kulatilake, P., D. Wathugala, and O. Stephansson. 1993. "Joint Network Modelling with a Validation Exercise in Stripa Mine, Sweden." *International Journal of Rock Mechanics and Mining Sciences & Geomechanical Abstracts* 30 (5): 503–526.
- Kulatilake, P., and T. Wu. 1986. "Relation Between Discontinuity Size and Trace Length." In *The 27th U.S. Symposium on Rock Mechanics (USRMS)*, 130–133. Tuscaloosa, AL.
- Lefranc, M., S. Farag, and B. Li. 2011. "Reservoir Characterization for Fracture Distribution Prediction and New Well Target Identification." In *Proceedings of SPE Asia Pacific Oil and Gas Conference and Exhibition*, 13. Jakarta, Indonesia: Society of Petroleum Engineers. doi:10.2118/145873-MS.
- Lewis, T.J., and J.G. Souther. 1978. "Meager Mountain, BC: A Possible Geothermal Energy Resource." *Energy, Mines and Resources Canada Earth Physics Branch Geothermal Series* 9 (null): 17.
- Long, J., K. Karasaki, A. Davey, J. Peterson, M. Landsfeld, J. Kemeny, and S. Martel. 1991. "An Inverse Approach to the Construction of Fracture Hydrology Models Conditioned by Geophysical Data." *International Journal of Rock Mechanics and Mining Sciences & Geomechanics Abstracts* 28 (2-3) (May): 121–142. doi:10.1016/0148-9062(91)92162-R.
- Long, J., and P. Witherspoon. 1985. "The Relationship of the Degree of Interconnection to Permeability in Fracture Networks." *Journal of Geophysical Research* 90 (B4): 3087–3098. doi:10.1029/JB090iB04p03087.
- Nevin, A. 1992. "Lessons from Frontier Exploration at Meager Creek and Pebble Creek, British Columbia, 1971-1992." *Geothermal Resources Council Transactions* 16: 105–110.
- Nevin, Sadlier-Brown, Goodbrand Ltd. 1974. "Report on Investigation of Geothermal Resources in Southwestern British Columbia". Vancouver, BC.
- Nevin, Sadlier-Brown, Goodbrand Ltd. 1978. "Progress Report for 1977 Meager Creek Geothermal Project, Investigations for 1977-1978". Vancouver, BC.
- Nevin, Sadlier-Brown, Goodbrand Ltd. 1979. "Report on 1978 Field Work Meager Creek Geothermal Area, Upper Lillooet River, British Columbia". Vancouver, BC.
- Nevin, Sadlier-Brown, Goodbrand Ltd. 1980. "Report on 1979 Drilling and Exploration Program Meager Creek Geothermal Area Upper Lillooet River, British Columbia". Vancouver, BC.

- Nevin, Sadlier-Brown, Goodbrand Ltd. 1981. "Report on 1980 Drilling and Exploration Program Meager Creek Geothermal Area Upper Lillooet River, British Columbia". Vancouver, BC.
- Nevin, Sadlier-Brown, Goodbrand Ltd. 1982. "Meager Creek Geothermal Area Slim Hole Drilling Summary, Volume 1: South Reservoir Area". Vancouver, BC.
- Priest, S. 1993. *Discontinuity Analysis for Rock Engineering*. Dordrecht: Springer Netherlands. doi:10.1007/978-94-011-1498-1.
- Priest, S, and J Hudson. 1976. "Discontinuity Spacings in Rock." *International Journal of Rock Mechanics and Mining Sciences & Geomechanics Abstracts* 13 (5) (May): 135–148. doi:10.1016/0148-9062(76)90818-4.
- Priest, S. 2004. "Determination of Discontinuity Size Distributions from Scanline Data." *Rock Mechanics and Rock Engineering* 37 (5) (July 27): 347–368. doi:10.1007/s00603-004-0035-2.
- Priest, S., and J. Hudson. 1981. "Estimation of Discontinuity Spacing and Trace Length Using Scanline Surveys." *International Journal of Rock Mechanics and Mining Sciences & Geomechanics Abstracts* 18 (3) (June): 183–197. doi:10.1016/0148-9062(81)90973-6.
- Read, P B. 1979. "Geology of Meager Creek Geothermal Area, British Columbia." doi:10.4095/129507.
- Robertson, A. 1970. "The Interpretation of Geologic Factors for Use in Slope Theory." In *Proceedings of the Symposium on the Theoretical Background to the Planning of Open Pit Mines*, edited by P.W.J. Van Rensburg, 55–71. Johannesburg, South Africa.
- Rogers, S., D. Elmo, R. Dunphy, and D. Bearinger. 2010. "Understanding Hydraulic Fracture Geometry and Interactions in the Horn River Basin through DFN and Numerical Modeling." In *Proceedings of Canadian Unconventional Resources and International Petroleum Conference*, 1–12. Calgary: Society of Petroleum Engineers. doi:10.2118/137488-MS.
- Sanyal, S., and S. Butler. 2005. "An Analysis of Power Generation Prospects from Enhanced Geothermal Systems." *Transactions - Geothermal Resource Council* 29: 131–137.
- Snow, D. 1965. "A Parallel Plate Model of Fractured Permeable Media". Berkeley, CA: University of California, Berkeley.

- Stauder, J., and J.W. Hunt. 1987. "Meager Creek Geothermal Project". Palo Alto, California: Electric Power Research Institute.
- Sturzenegger, M., and D. Stead. 2009. "Close-Range Terrestrial Digital Photogrammetry and Terrestrial Laser Scanning for Discontinuity Characterization on Rock Cuts." *Engineering Geology* 106 (3-4) (June): 163–182. doi:10.1016/j.enggeo.2009.03.004.
- Szymakowski, J. 2011. "Measuring Discontinuity Orientation in High Temperature Boreholes." In *Slope Stability 2011: International Symposium on Rock Slope Stability in Open Pit Mining and Civil Engineering*, 9. Vancouver, BC.
- Tester, JW, B Anderson, and A Batchelor. 2006. "The Future of Geothermal Energy: Impact of Enhanced Geothermal Systems (EGS) on the United States in the 21st Century." *Massachusetts Institute of Idaho*.
- The Weather Network. 2014. "Statistics: Pemberton, British Columbia - Farmzone." <http://www.farmzone.com/statistics/temperature/cl1086082/sb038>.
- Van Der Pluijm, B., and S. Marshak. 1997. *Earth Structure: An Introduction to Structural Geology and Tectonics*. 1st ed. McGraw-Hill College.
- Warburton, P. 1980. "Stereological Interpretation of Joint Trace Data: Influence of Joint Shape and Implications for Geological Surveys." *International Journal of Rock Mechanics and Mining Sciences & Geomechanics Abstracts* 17 (6) (December): 305–316. doi:10.1016/0148-9062(80)90513-6.
- Zhang, L., and H. Einstein. 2009. "The Planar Shape of Rock Joints." *Rock Mechanics and Rock Engineering* 43 (1) (June 3): 55–68. doi:10.1007/s00603-009-0054-0.
- Zhang, L., H. Einstein, and W. Dershowitz. 2002. "Stereological Relationship Between Trace Length and Size Distribution of Elliptical Discontinuities." *Géotechnique* 52 (6) (January 8): 419–433. doi:10.1680/geot.2002.52.6.419.
- Zhang, L., and H.H Einstein. 2000. "Estimating the Intensity of Rock Discontinuities." *International Journal of Rock Mechanics and Mining Sciences* 37 (5) (July): 819–837. doi:10.1016/S1365-1609(00)00022-8.

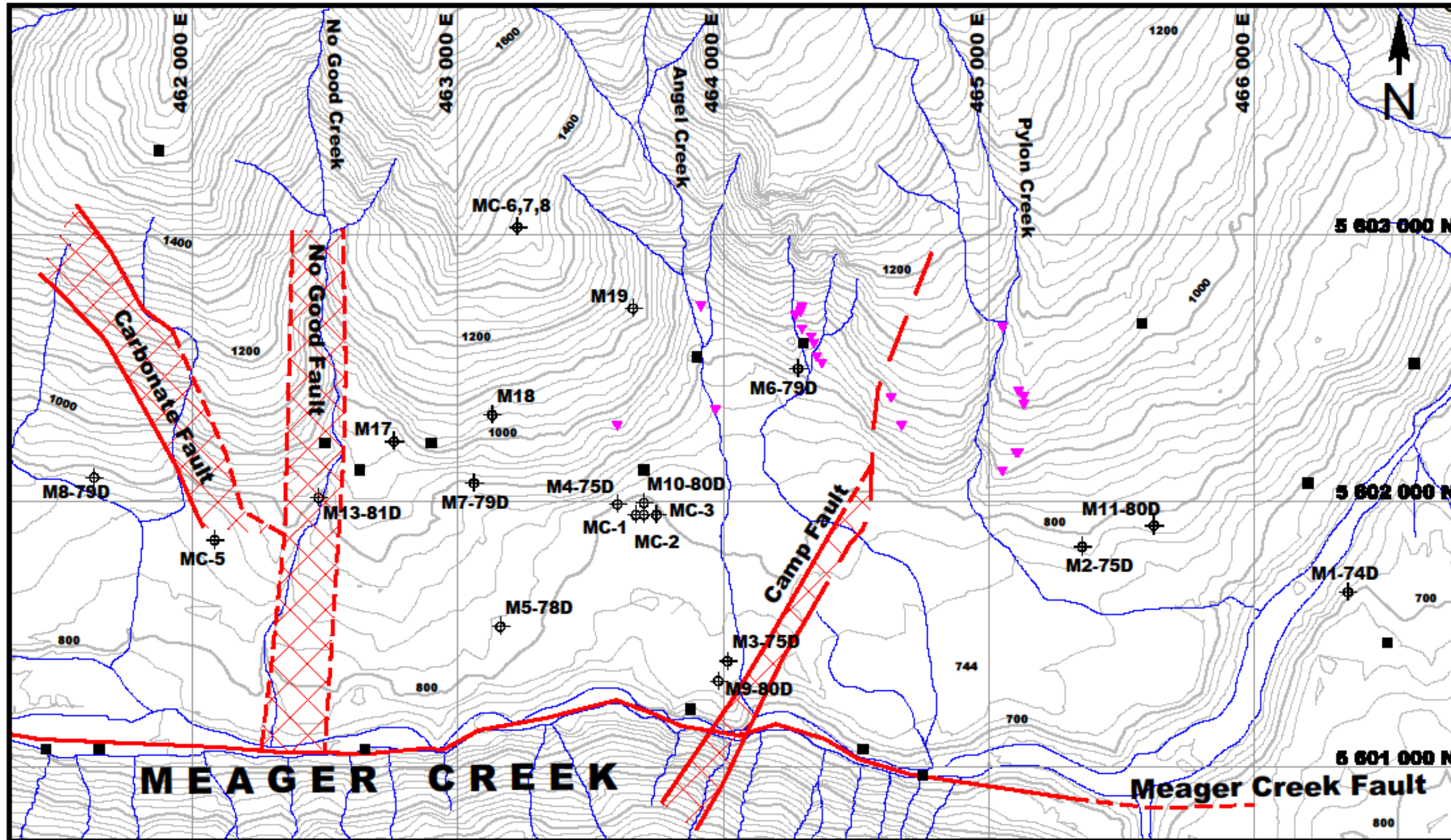
APPENDICES

Appendix A: Maps



MEAGER MOUNTAIN GEOTHERMAL AREA

Contour lines received from Terrain Resource Information Management Program (TRIM) BC August 20, 2013
 Contour lines last updated March 11, 2003



DRILLHOLE COLLAR AND MAPPING STATION LOCATIONS, MEAGER CREEK SITE (SOUTH RESERVOIR)

- 1980 mapping station
- ▼ 1981 mapping station
- ⊕ Slim hole/well collar location

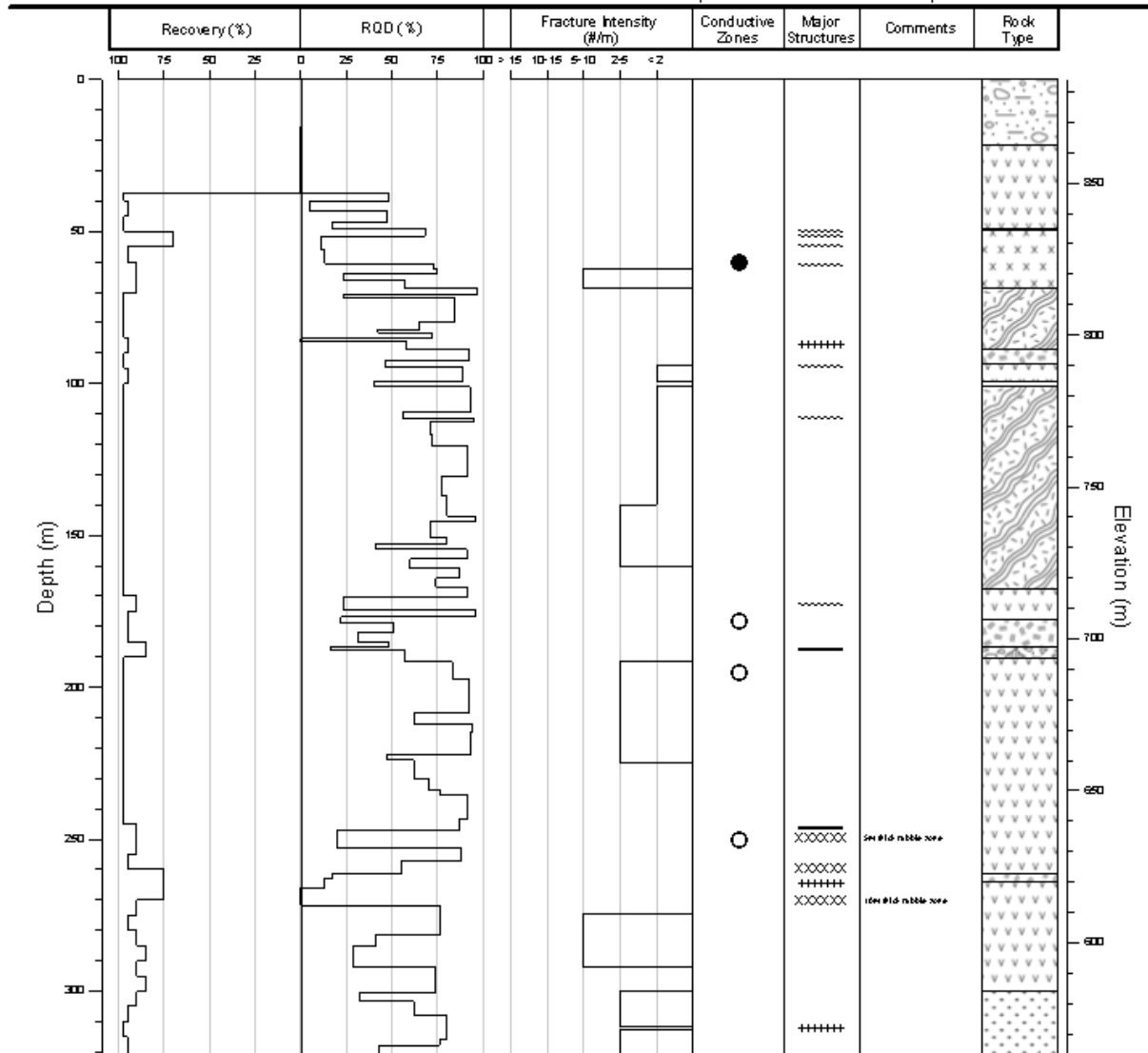
— Fault trace

Contour lines received from Terrain Resource Information Management Program (TRIM) BC August 20, 2013
Contour lines last updated March 11, 2003

Appendix B: Geomechanical Logs

DRILLHOLE LOG : M6-79D

Coordinates: N 5 602 499 E 464 281 Collar Elevation: 884 m Depth: 321 m Azimuth: 0° Dip: -90°



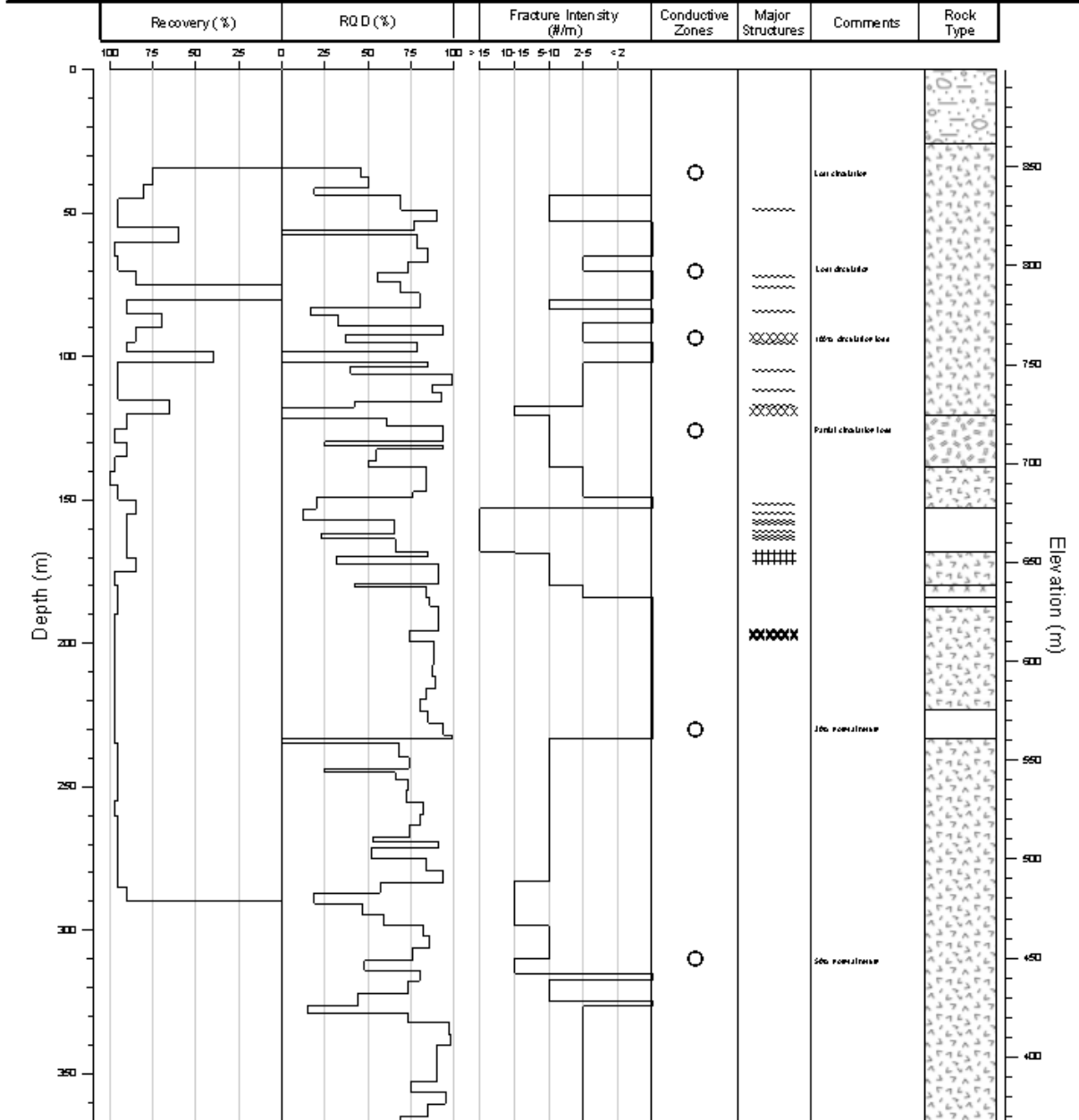
STRUCTURE	LITHOLOGY	CONDUCTIVE ZONES
----- Fault Zone	Overburden (OV)	Water Producing Zone
..... Shear Zone	Amphibolite (AM)	Lost Circulation
----- Dyke	Andesite (AN)	
xxxxxx Rubble Zone	Basalt (BA)	
	Breccia (BR)	
	Dacite (DA)	
	Gneiss (GN)	
	Hornfels (HN)	
	Metavolcanics (MV)	
	Quartz Diorite (QD)	
	Rhyolite (RY)	

GEOMECHANICAL DRILLHOLE LOG: M6-79D MEAGER CREEK, SOUTH RESERVOIR

SCALE
1:2000

DRILLHOLE LOG : M7-79D

Coordinates: N 5 602 069 E 463 061 Collar Elevation: 899 m Depth: 367 m Azimuth: 0° Dip: -90°

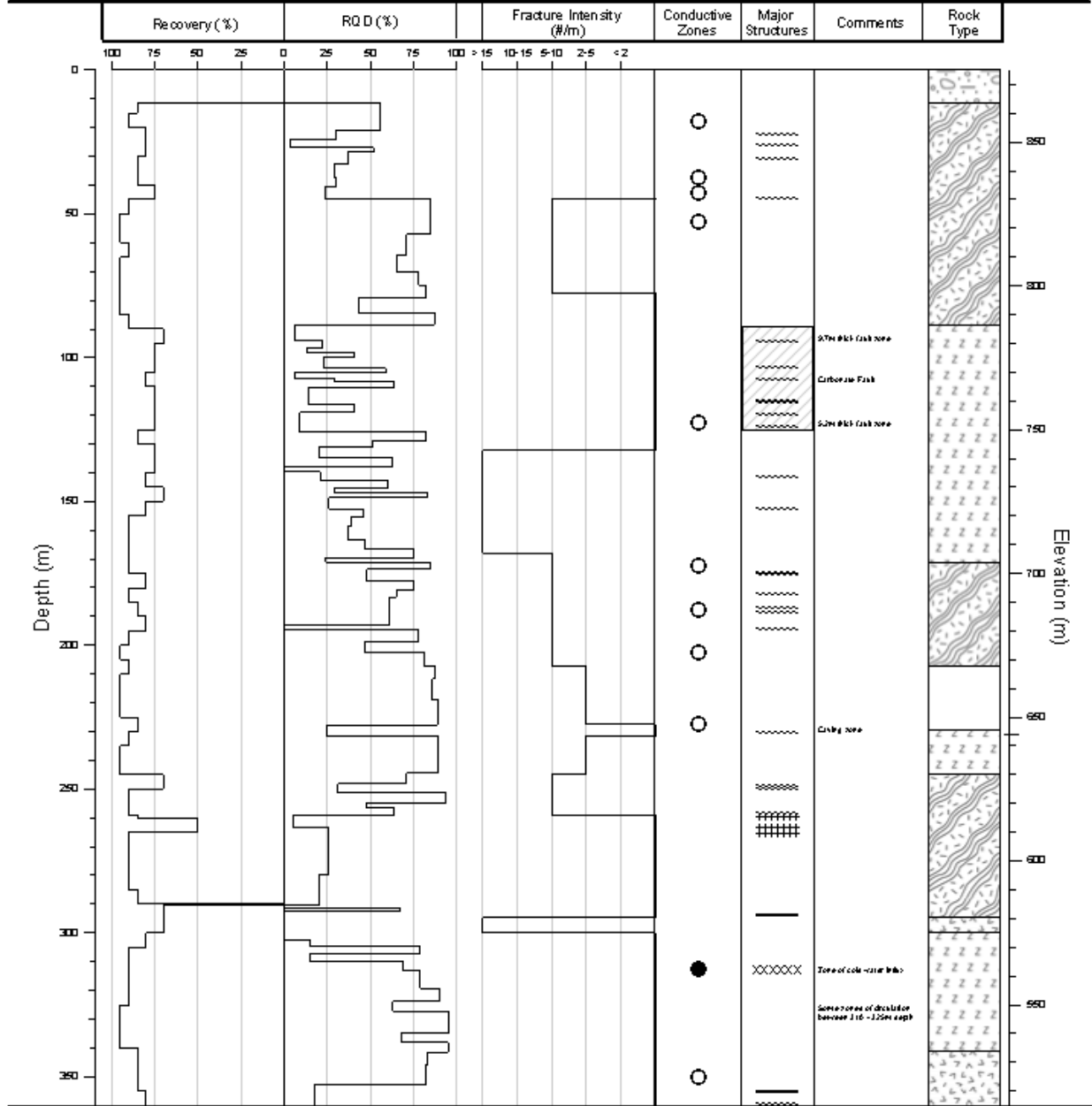


GEOMECHANICAL DRILLHOLE LOG: M7-79D MEAGER CREEK, SOUTH RESERVOIR

SCALE
1:2000

DRILLHOLE LOG : M8-79D

Coordinates: N 5 602 089 E 461 631 Collar Elevation: 875 m Depth: 497 m Azimuth: 000° Dip: -90°



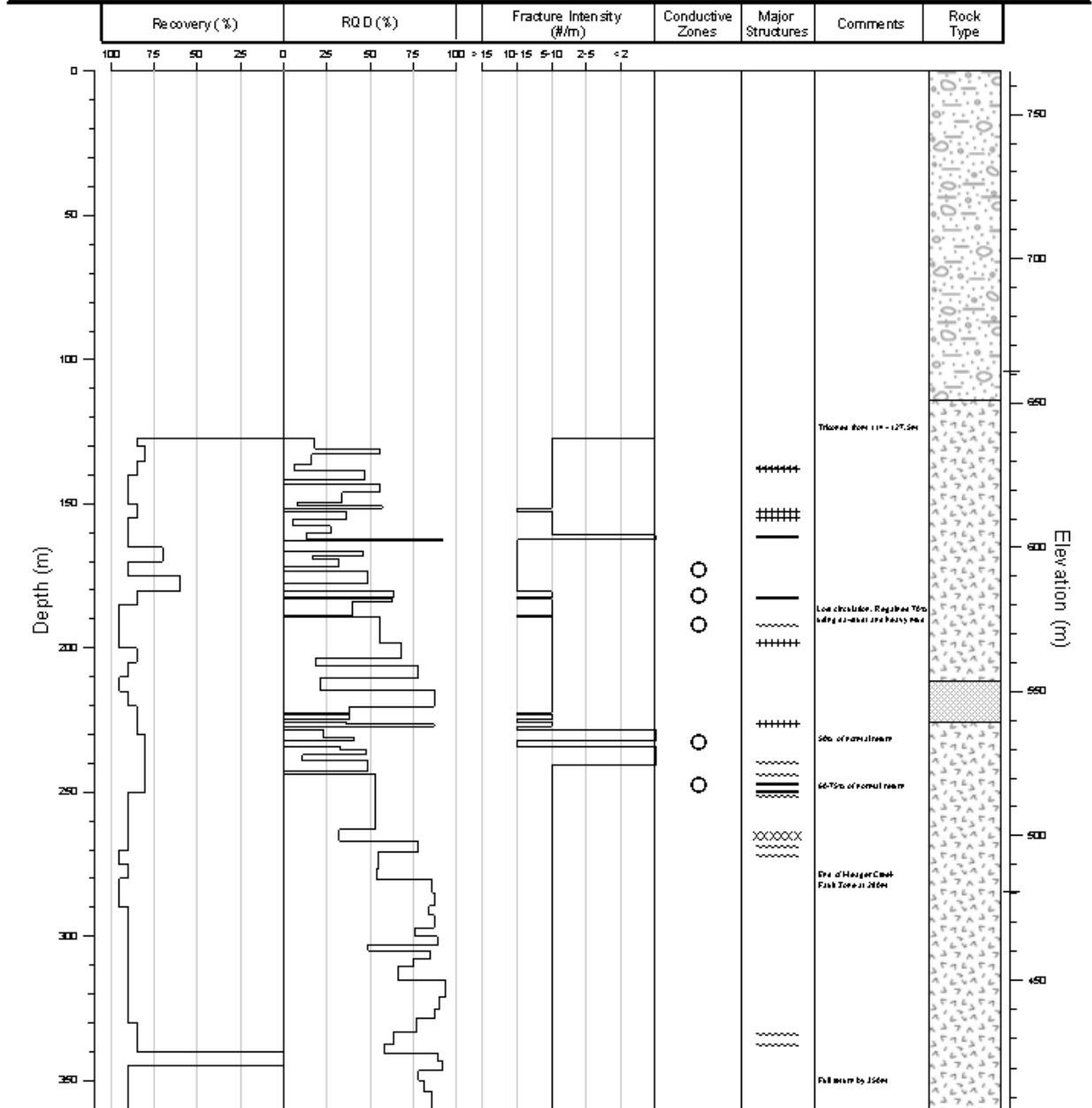
STRUCTURE	LITHOLOGY	CONDUCTIVE ZONES
----- Fault Zone	Overburden (OV)	Water Producing Zone
..... Shear Zone	Amphibolite (AM)	Lost Circulation
----- Dyke	Andesite (AN)	
xxxxxx Rubble Zone	Basalt (BA)	
	Breccia (BR)	
	Dacite (DA)	
	Gneiss (GN)	
	Hornfels (HN)	
	Metavolcanics (MV)	
	Quartz Diorite (QD)	
	Rhyolite (RY)	

GEOMECHANICAL DRILLHOLE LOG: M8-79D, 1 of 2
MEAGER CREEK, SOUTH RESERVOIR

SCALE
1:2000
 164

DRILLHOLE LOG : M9-80D

Coordinates: N 5 601 324 E 463 981 Collar Elevation: 765 m Depth: 1142 m Azimuth: 000° Dip: -90°



Information available up to 27.5 from well log - correct 06/11/2018. Reported elevations have been corrected using whole hole depth measurements

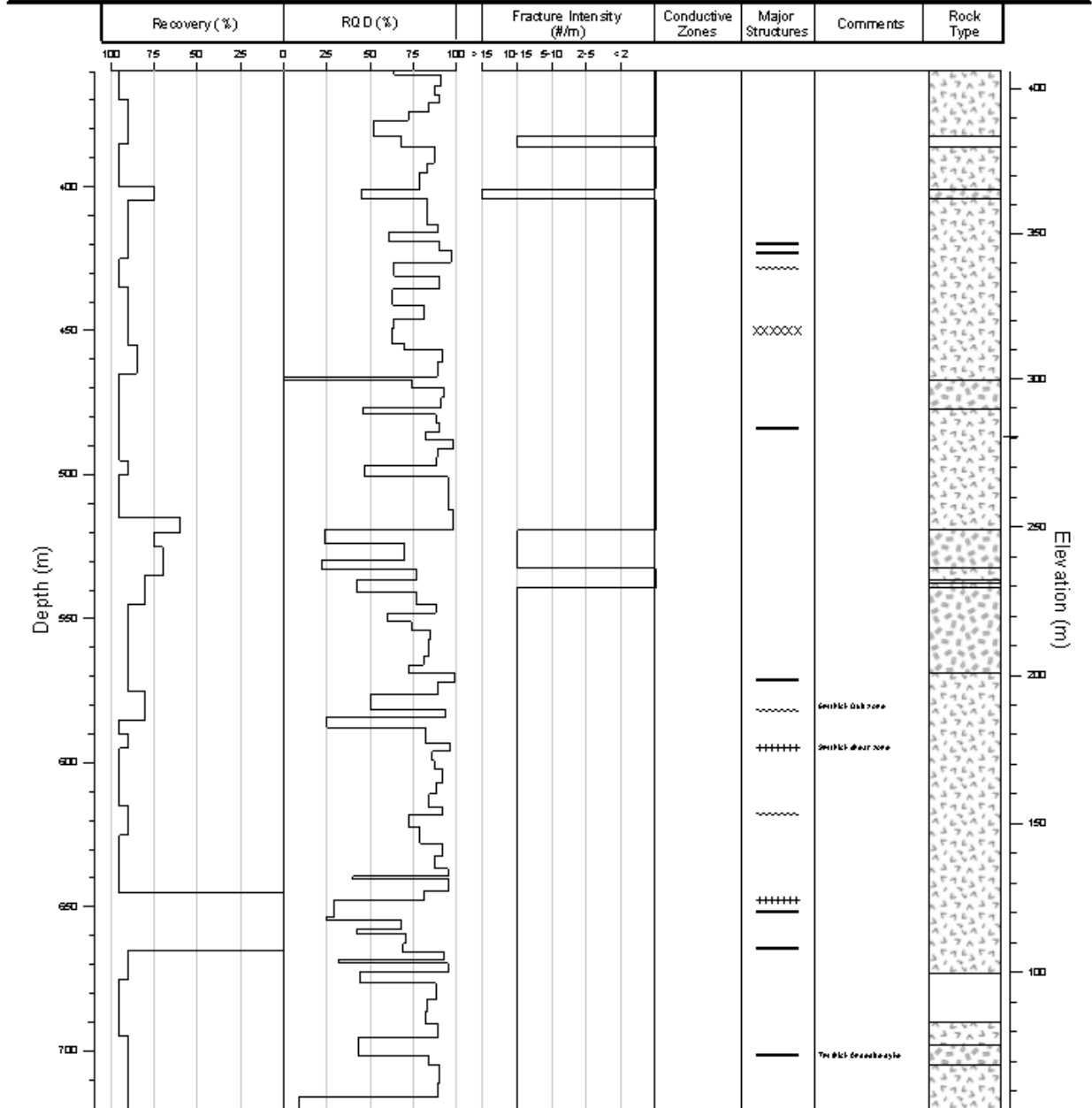
STRUCTURE	LITHOLOGY	CONDUCTIVE ZONES
~~~~~ Fault Zone	Overburden (OV)	Water Producing Zone
+++++ Shear Zone	Amphibolite (AM)	Lost Circulation
----- Dyke	Andesite (AN)	
xxxxx Rubble Zone	Basalt (BA)	
	Breccia (BR)	
	Dacite (DA)	
	Gneiss (GN)	
	Hornfels (HN)	
	Metavolcanics (MV)	
	Quartz Diorite (QD)	
	Rhyolite (RY)	

## GEOMECHANICAL DRILLHOLE LOG: M9-80D, 1 of 4 MEAGER CREEK, SOUTH RESERVOIR

SCALE  
1:2000  
166

# DRILLHOLE LOG : M9-80D

Coordinates: N 5 601 324 E 463 981 Collar Elevation: 765 m Depth: 1142 m Azimuth: 000° Dip: -90°



Information available up to 07.5 from vertical to core 061 271431. Reported elevations have been corrected using a whole hole depth correction.

STRUCTURE	LITHOLOGY	CONDUCTIVE ZONES
----- Fault Zone	Overburden (OV)	Water Producing Zone
+++++ Shear Zone	Amphibolite (AM)	Lost Circulation
----- Dyke	Andesite (AN)	
xxxxxx Rubble Zone	Basalt (BA)	
	Breccia (BR)	
	Dacite (DA)	
	Gneiss (GN)	
	Hornfels (HN)	
	Metavolcanics (MV)	
	Quartz Diorite (QD)	
	Rhyolite (RY)	

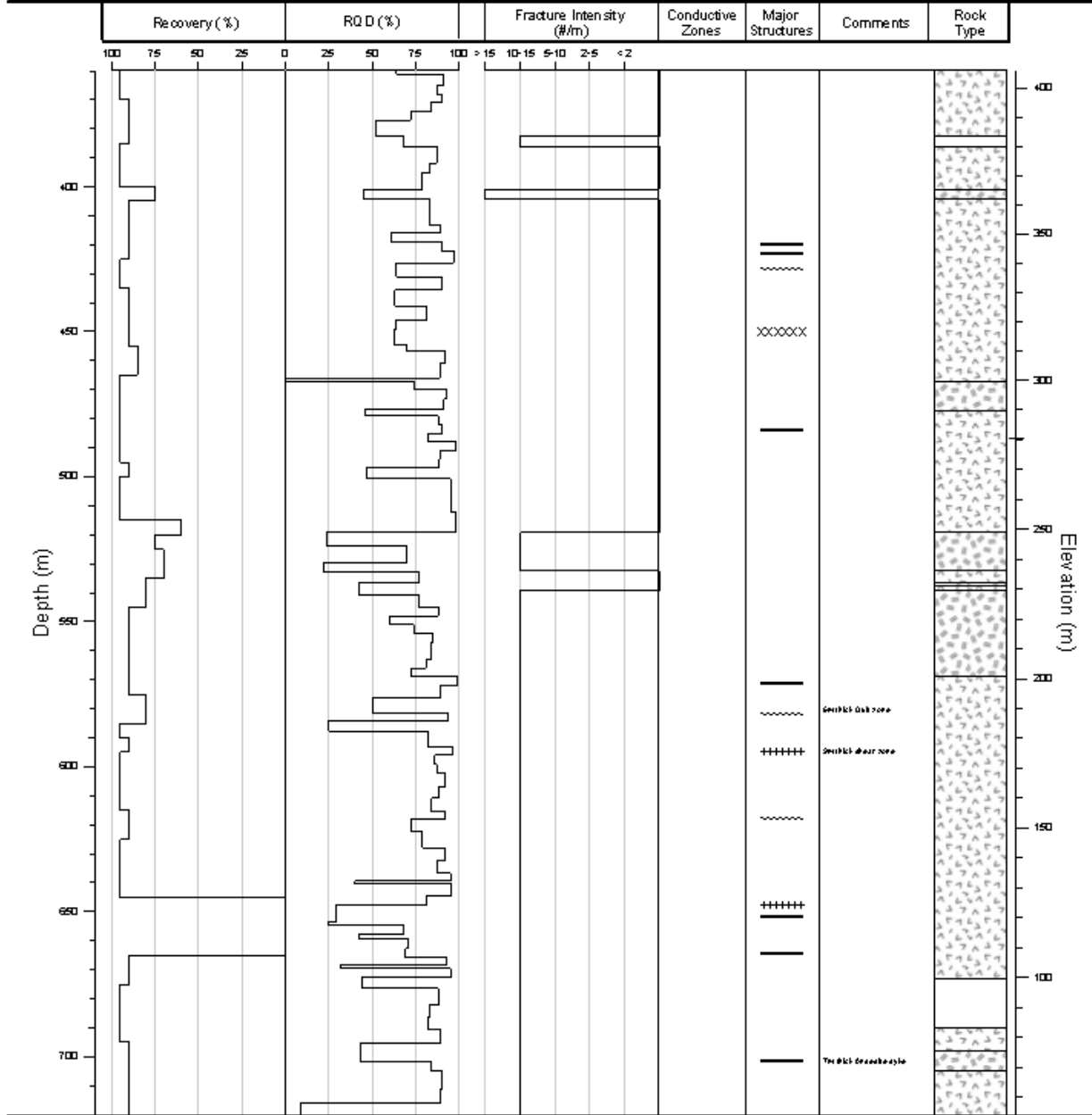
## GEOMECHANICAL DRILLHOLE LOG: M9-80D, 2 of 4 MEAGER CREEK, SOUTH RESERVOIR

SCALE

1:2000

# DRILLHOLE LOG : M9-80D

Coordinates: N 5 601 324 E 463 981 Collar Elevation: 765 m Depth: 1142 m Azimuth: 000° Dip: -90°



Indicaciones anteriores up to 07.5 from well to curve 001 27687. Reported elevations have been corrected using an-ortho to-ortho measurements

STRUCTURE	LITHOLOGY	CONDUCTIVE ZONES
----- Fault Zone	Overburden (OV)	Water Producing Zone
+++++ Shear Zone	Amphibolite (AM)	Lost Circulation
----- Dyke	Andesite (AN)	
xxxxxx Rubble Zone	Basalt (BA)	
	Breccia (BR)	
	Dacite (DA)	
	Gneiss (GN)	
	Hornfels (HN)	
	Metavolcanics (MV)	
	Quartz Diorite (QD)	
	Rhyolite (RY)	

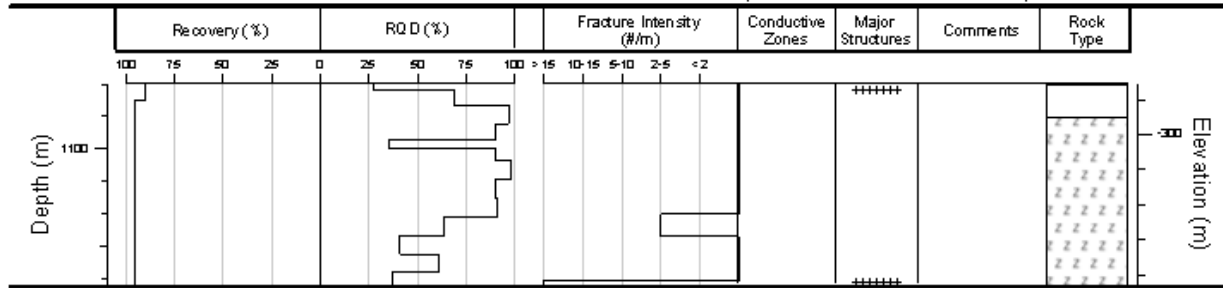
## GEOMECHANICAL DRILLHOLE LOG: M9-80D, 2 of 4 MEAGER CREEK, SOUTH RESERVOIR

SCALE

1:2000

# DRILLHOLE LOG : M9-80D

Coordinates: N 5 601 324 E 463 981 Collar Elevation: 765 m Depth: 1142 m Azimuth: 000° Dip: -90°



Information on this log is derived from well log M9-80D-1142.0. The data was collected by the well log M9-80D-1142.0.

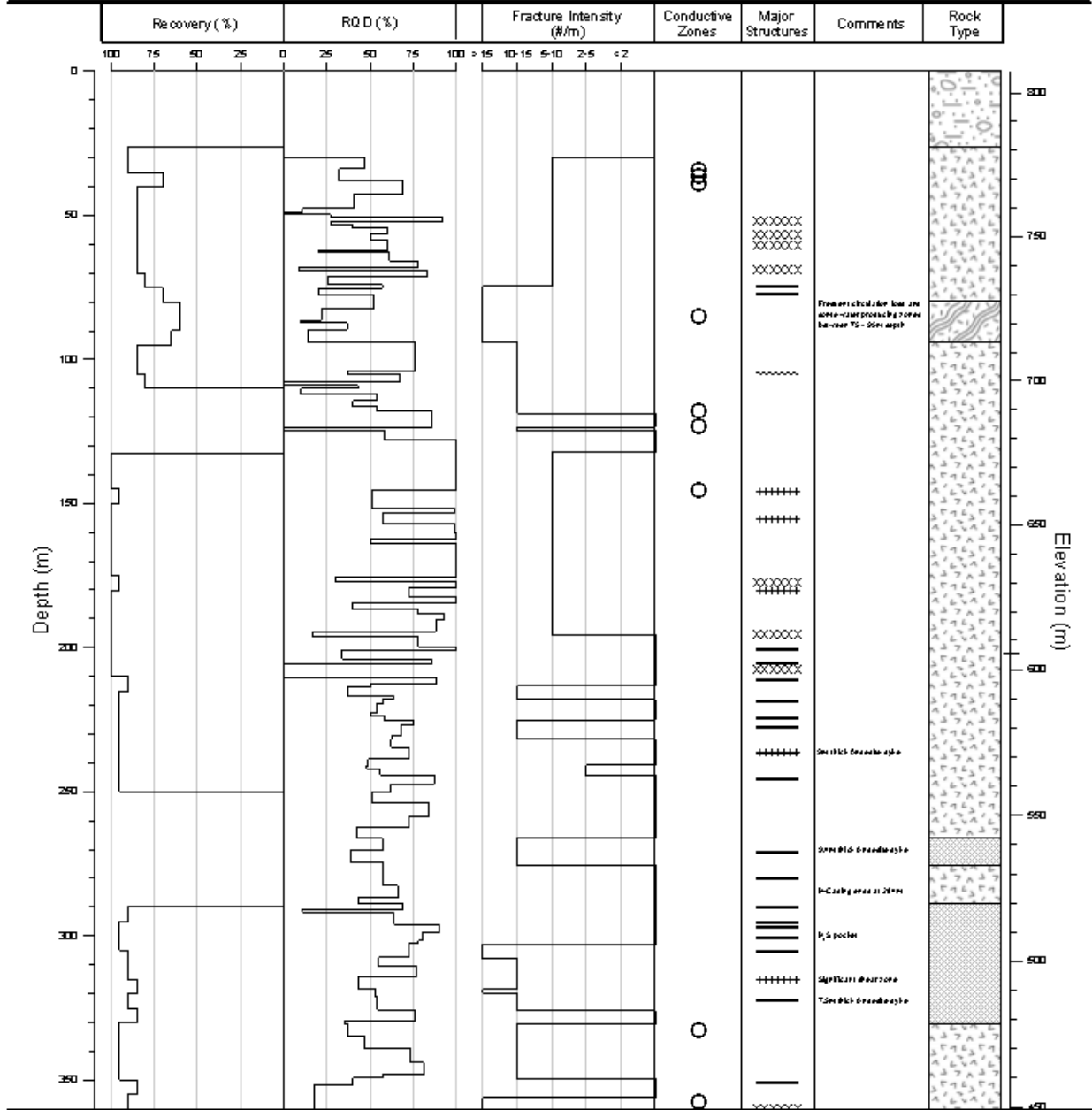
STRUCTURE	LITHOLOGY		CONDUCTIVE ZONES
----- Fault Zone	Overburden (OV)	Breccia (BR)	● Water Producing Zone
----- Shear Zone	Amphibolite (AM)	Dacite (DA)	○ Lost Circulation
----- Dyke	Andesite (AN)	Gneiss (GN)	
××××× Rubble Zone	Basalt (BA)	Hornfels (HN)	
		Metavolcanics (MV)	
		Quartz Diorite (QD)	
		Rhyolite (RY)	

**GEOMECHANICAL DRILLHOLE LOG: M9-80D, 4 of 4**  
**MEAGER CREEK, SOUTH RESERVOIR**

SCALE  
**1:2000**

# DRILLHOLE LOG : M10-80D

Coordinates: N 5 601 994 E 463 701 Collar Elevation: 807.5 m Depth: 1070 m Azimuth: 000° Dip: -90°



Data reported as of 10/10/2010. Recovery data is based on the recovery of the drill pipe. Fracture intensity is based on the number of fractures per meter. Rock type is based on the lithology log.

STRUCTURE	LITHOLOGY	CONDUCTIVE ZONES
~~~~~ Fault Zone	Overburden (OV)	Water Producing Zone
+++++ Shear Zone	Amphibolite (AM)	Lost Circulation
----- Dyke	Andesite (AN)	
xxxxx Rubble Zone	Basalt (BA)	
	Breccia (BR)	
	Dacite (DA)	
	Gneiss (GN)	
	Hornfels (HN)	
	Metavolcanics (MV)	
	Quartz Diorite (QD)	
	Rhyolite (RY)	

GEOMECHANICAL DRILLHOLE LOG: M10-80D, 1 of 3

MEAGER CREEK, SOUTH RESERVOIR

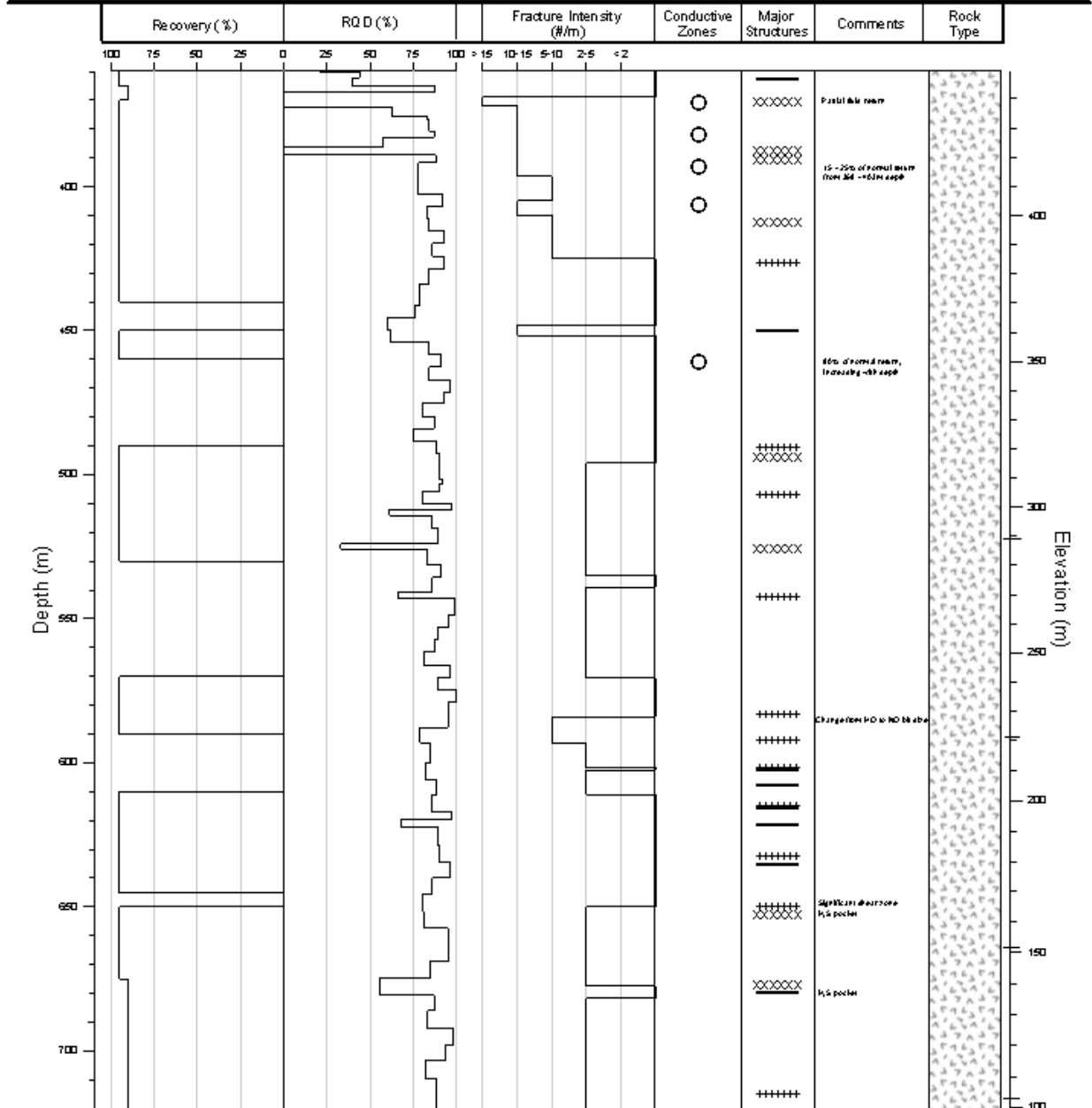
SCALE

1:2000

170

DRILLHOLE LOG : M10-80D

Coordinates: N 5 601 994 E 463 701 Collar Elevation: 807.5 m Depth: 1070 m Azimuth: 000° Dip: -90°



Information available up to 40' from wellbore is from 600' depth. Reported elevations have been corrected using geophysical data measurements. Approximate 10' of the shaft is traversed by H10400. H10400 has a 4" diameter, because the zone

STRUCTURE		LITHOLOGY			CONDUCTIVE ZONES	
~~~~~	Fault Zone	Overburden (OV)	Breccia (BR)	Metavolcanics (MV)	●	Water Producing Zone
+++++	Shear Zone	Amphibolite (AM)	Dacite (DA)	Quartz Diorite (QD)	○	Lost Circulation
-----	Dyke	Andesite (AN)	Gneiss (GN)	Rhyolite (RY)		
xxxxx	Rubble Zone	Basalt (BA)	Hornfels (HN)			

## GEOMECHANICAL DRILLHOLE LOG: M10-80D, 2 of 3

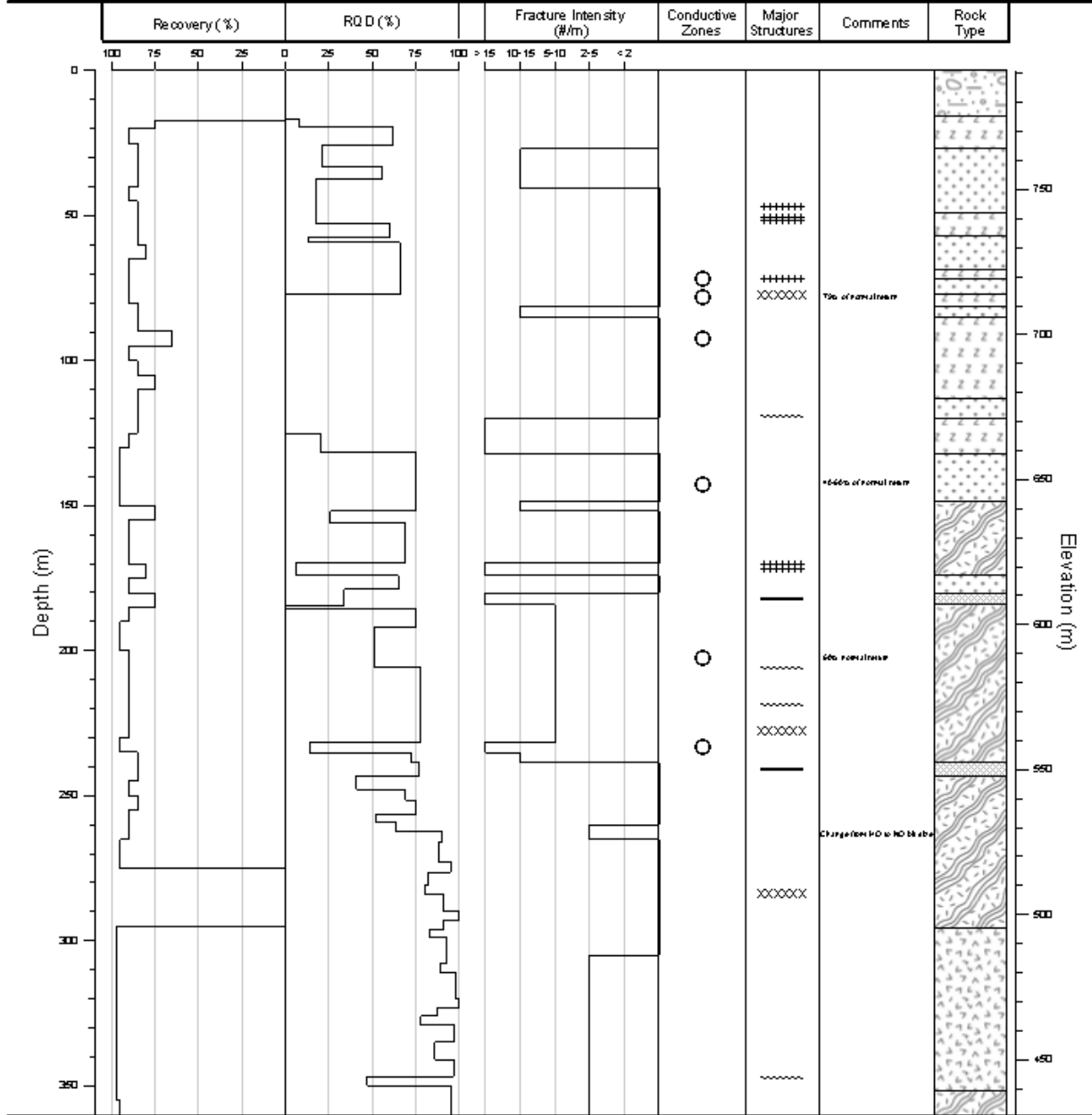
### MEAGER CREEK, SOUTH RESERVOIR

SCALE  
1:2000  
171



# DRILLHOLE LOG : M11-80D

Coordinates: N 5 601 909 E 465 621 Collar Elevation: 791 m Depth: 559.4 m Azimuth: 000° Dip: -90°



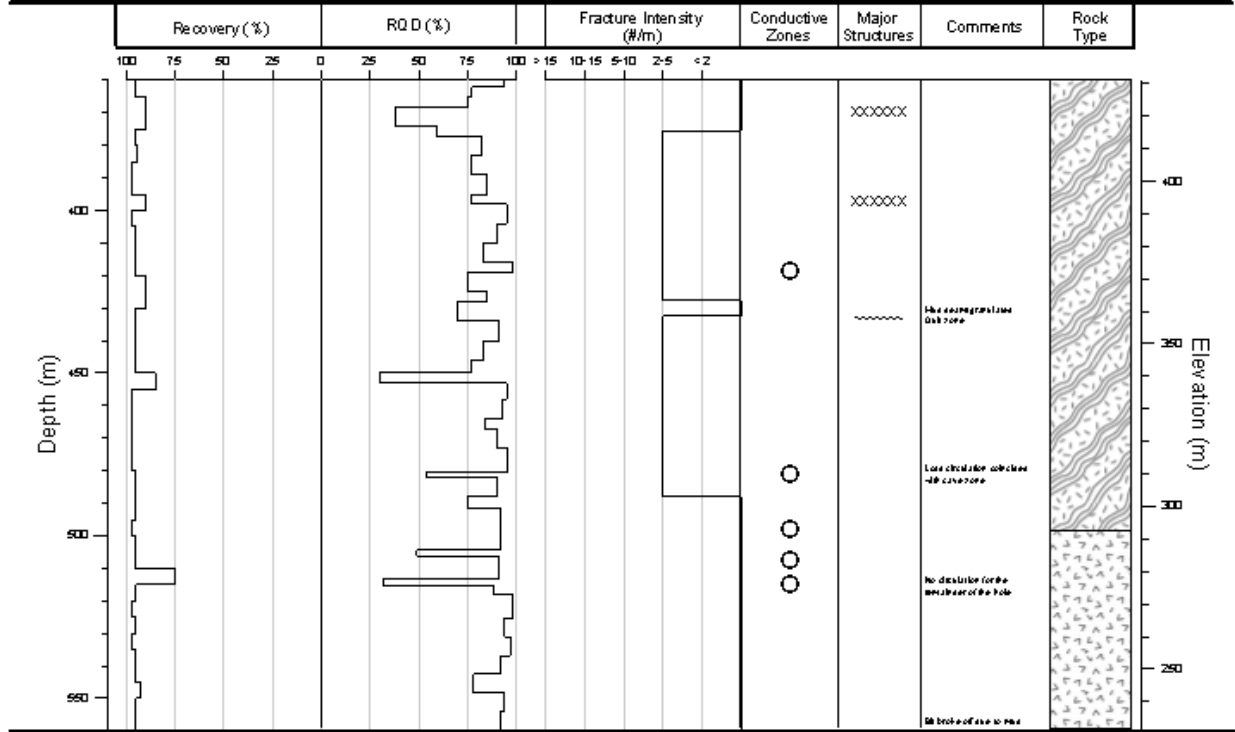
STRUCTURE	LITHOLOGY	CONDUCTIVE ZONES
----- Fault Zone	Overburden (OV)	Water Producing Zone
----- Shear Zone	Amphibolite (AM)	Lost Circulation
----- Dyke	Andesite (AN)	
xxxxxx Rubble Zone	Basalt (BA)	
	Breccia (BR)	
	Dacite (DA)	
	Gneiss (GN)	
	Hornfels (HN)	
	Metavolcanics (MV)	
	Quartz Diorite (QD)	
	Rhyolite (RY)	

GEOMECHANICAL DRILLHOLE LOG: M11-80D, 1 of 2  
MEAGER CREEK, SOUTH RESERVOIR

SCALE  
1:2000

# DRILLHOLE LOG : M11-80D

Coordinates: N 5 601 909 E 465 621 Collar Elevation: 791 m Depth: 559.4 m Azimuth: 000° Dip: -90°



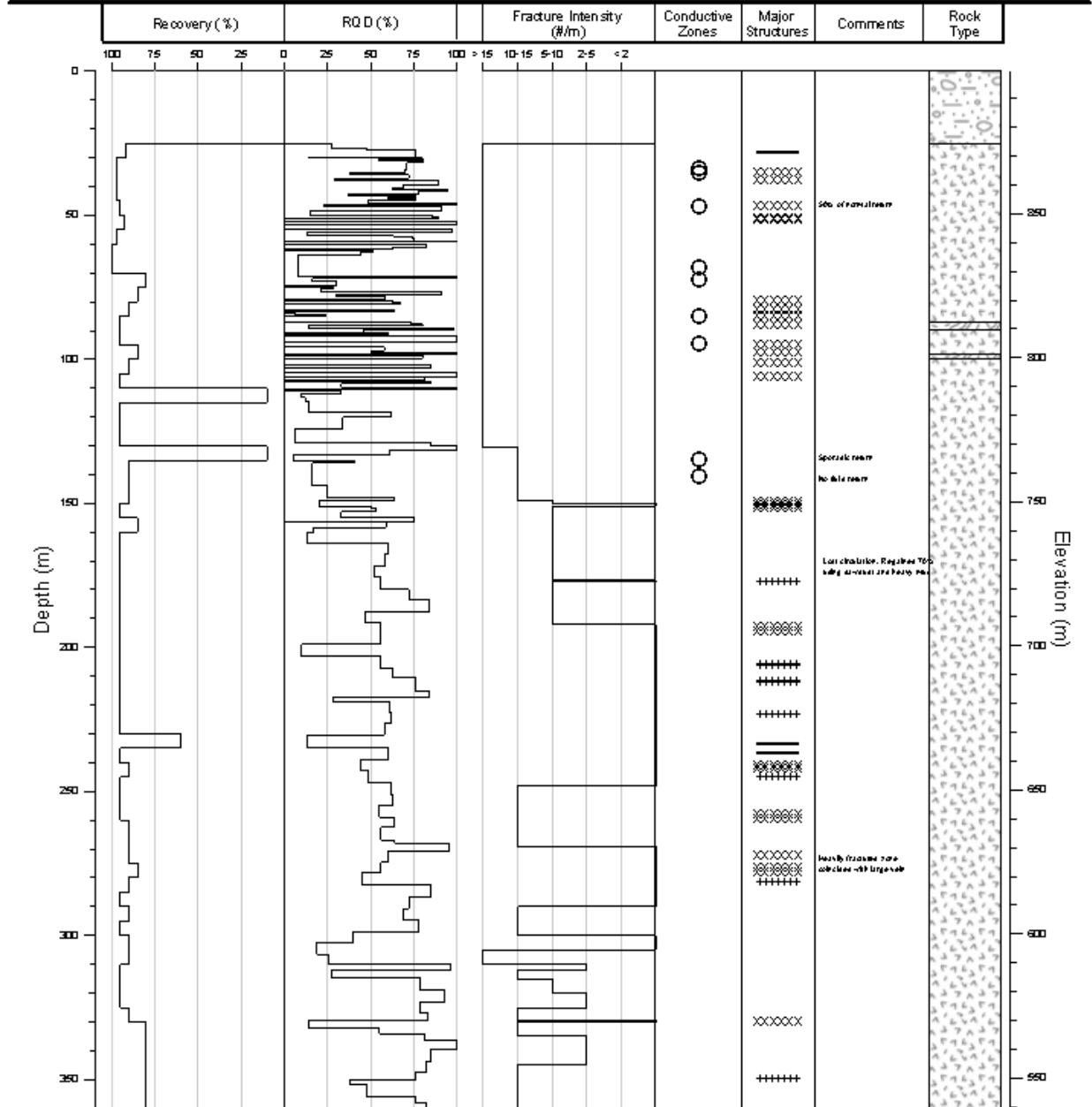
STRUCTURE	LITHOLOGY	CONDUCTIVE ZONES
----- Fault Zone	Overburden (OV)	Water Producing Zone
..... Shear Zone	Amphibolite (AM)	Lost Circulation
----- Dyke	Andesite (AN)	
xxxxxx Rubble Zone	Basalt (BA)	
	Breccia (BR)	
	Dacite (DA)	
	Gneiss (GN)	
	Hornfels (HN)	
	Metavolcanics (MV)	
	Quartz Diorite (QD)	
	Rhyolite (RY)	

GEO MECHANICAL DRILLHOLE LOG: M11-80D, 2 of 2  
MEAGER CREEK, SOUTH RESERVOIR

SCALE  
1:2000  
174

# DRILLHOLE LOG : M13-81D

Coordinates: N 5 602 014 E 462 476 Collar Elevation: 899 m Depth: 599.5 m Azimuth: 000° Dip: -90°



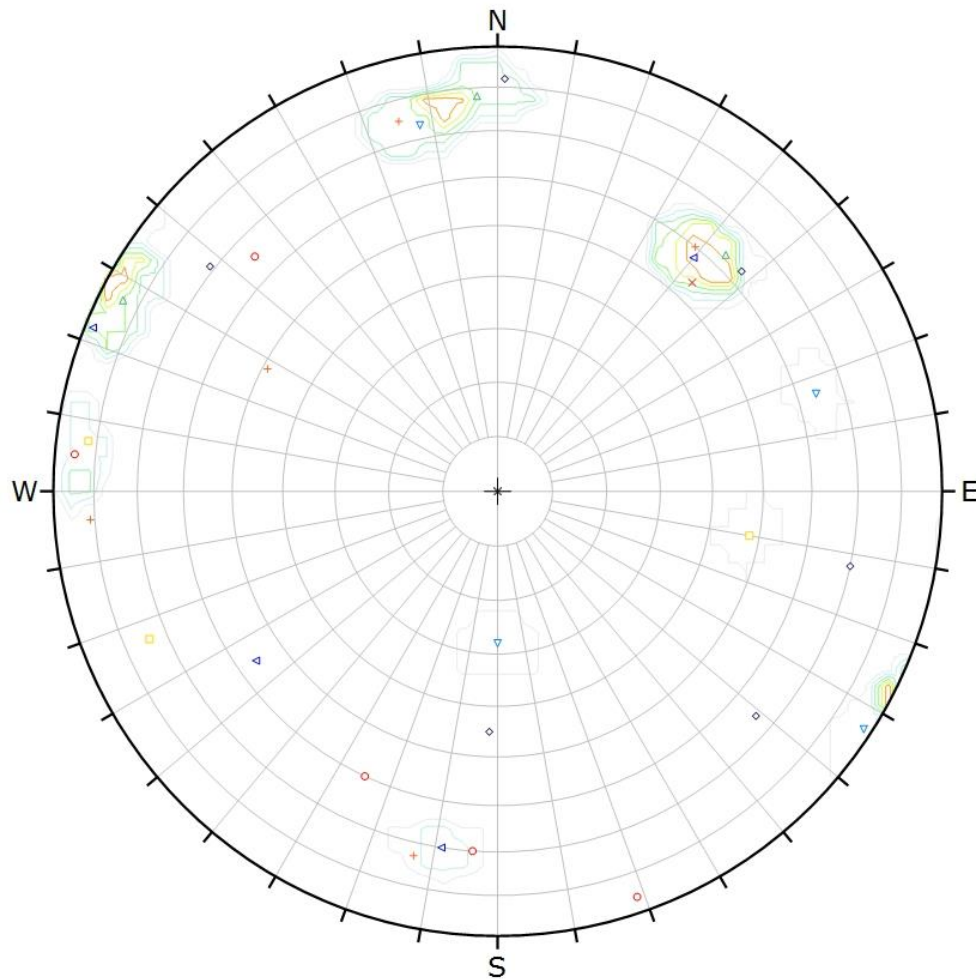
STRUCTURE	LITHOLOGY	CONDUCTIVE ZONES
..... Fault Zone	Overburden (OV)	Water Producing Zone
+++++ Shear Zone	Amphibolite (AM)	Lost Circulation
----- Dyke	Andesite (AN)	
xxxxxx Rubble Zone	Basalt (BA)	
	Breccia (BR)	
	Dacite (DA)	
	Gneiss (GN)	
	Hornfels (HN)	
	Metavolcanics (MV)	
	Quartz Diorite (QD)	
	Rhyolite (RY)	

**GEOMECHANICAL DRILLHOLE LOG: M13-81D, 1 of 2**  
**MEAGER CREEK, SOUTH RESERVOIR**

SCALE  
**1:2000**  
 175



## **Appendix C: Stereographic Plots of Surface Mapping Data**

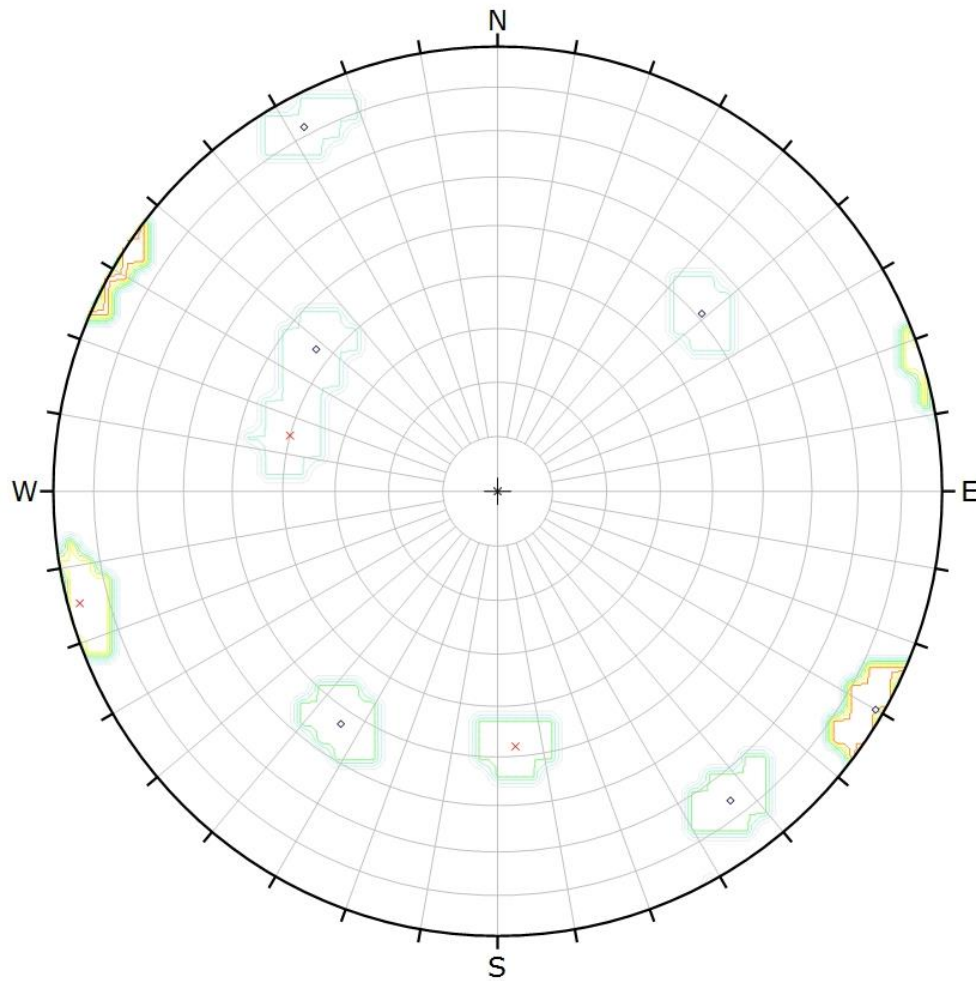


Symbol	STATION	Quantity
◇	MAP1980_004	28
×	MAP1980_005	7
△	MAP1980_006	40
+	MAP1980_007	40
▽	MAP1980_009	52
□	MAP1980_011	24
◁	MAP1980_018	26
○	MAP1980_021	32

Color	Density Concentrations
	0.00 - 2.00
	2.00 - 4.00
	4.00 - 6.00
	6.00 - 8.00
	8.00 - 10.00
	10.00 - 12.00
	12.00 - 14.00
	14.00 <
<b>Maximum Density</b>	16.31%
<b>Contour Data</b>	Pole Vectors
<b>Contour Distribution</b>	Schmidt
<b>Counting Circle Size</b>	1.0%

<b>Plot Mode</b>	Pole Vectors
<b>Vector Count</b>	248 (31 Entries)
<b>Hemisphere</b>	Lower
<b>Projection</b>	Equal Area

1980 Surface Mapping - South Reservoir  
 - Poles represent Peak Orientations  
 - Poles are weighted



Symbol	STATION	Quantity
◇	MAP1980_019	32
×	MAP1980_020	16

Color	Density Concentrations
	0.00 - 2.00
	2.00 - 4.00
	4.00 - 6.00
	6.00 - 8.00
	8.00 - 10.00
	10.00 - 12.00
	12.00 - 14.00
	14.00 - 16.00
	16.00 <

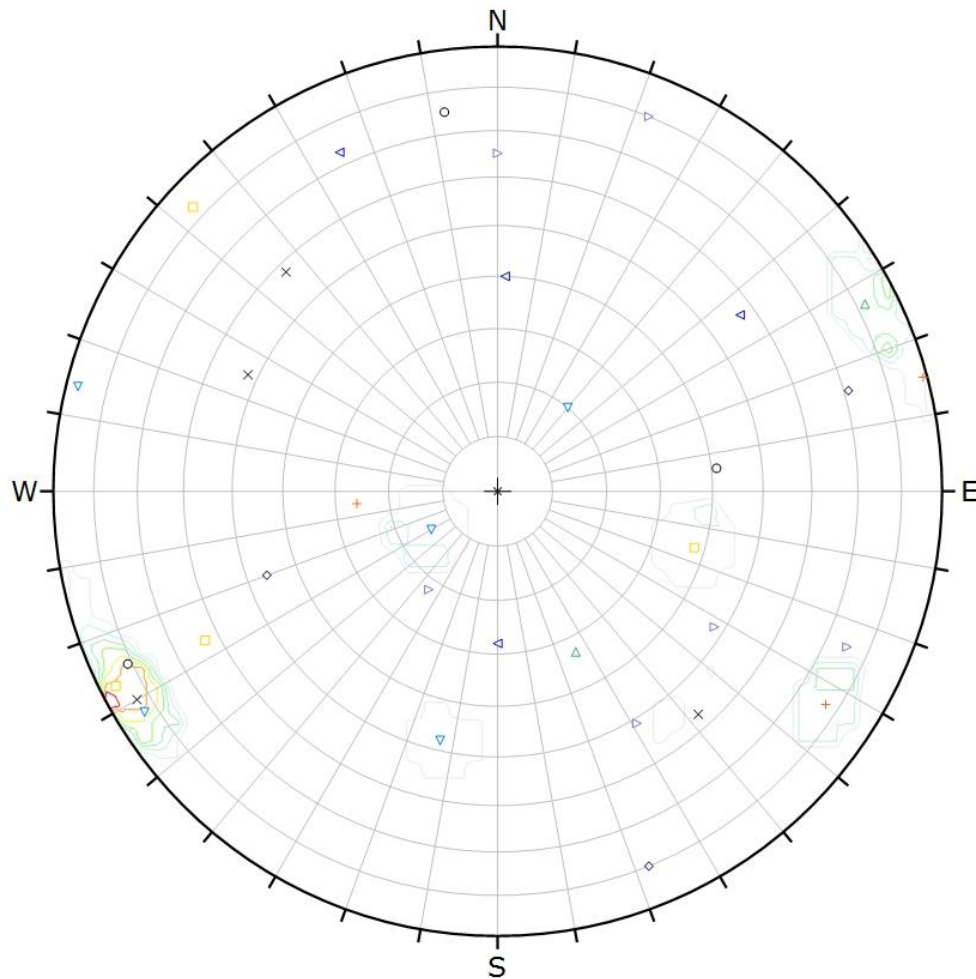
  

<b>Maximum Density</b>	17.68%
<b>Contour Data</b>	Pole Vectors
<b>Contour Distribution</b>	Schmidt
<b>Counting Circle Size</b>	1.0%

<b>Plot Mode</b>	Pole Vectors
<b>Vector Count</b>	48 (9 Entries)
<b>Hemisphere</b>	Lower
<b>Projection</b>	Equal Area

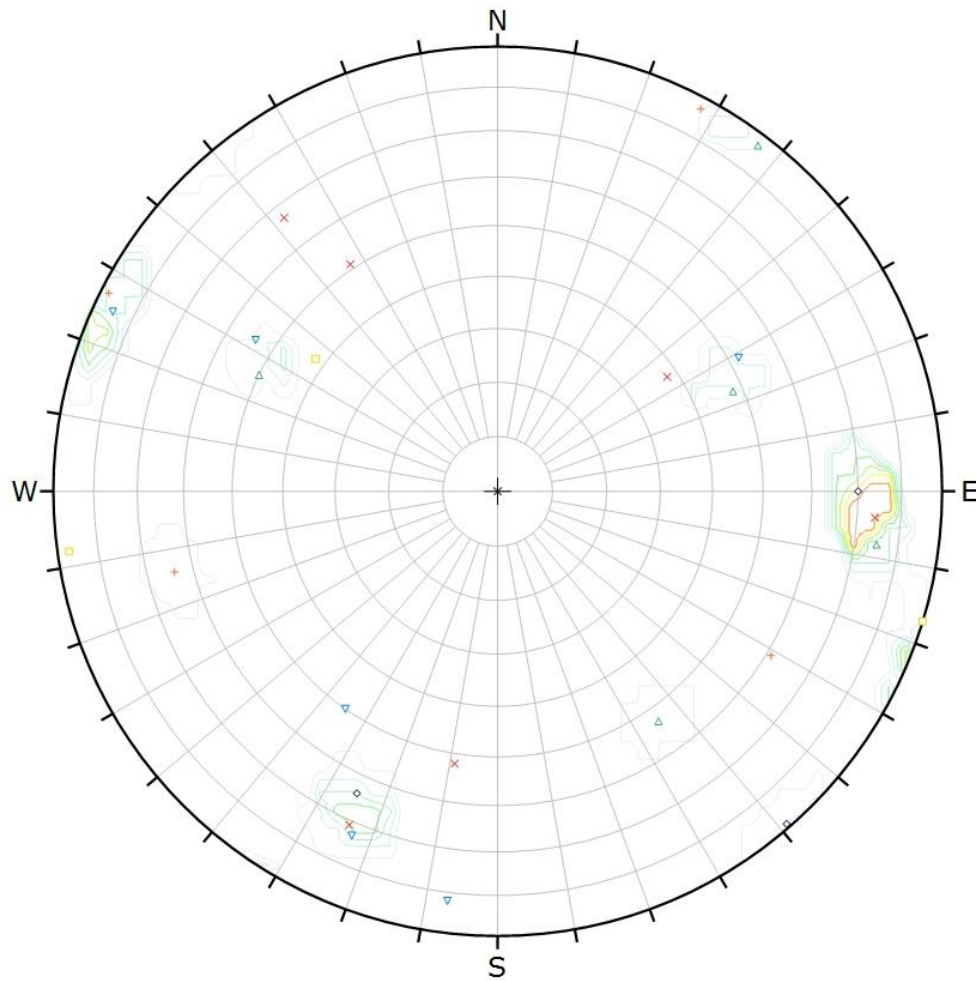
1980 Surface Mapping - East of Camp Fault  
 - Poles represent Peak Orientations  
 - Poles are weighted



Symbol	STATION	Quantity
◇	MAP1980_002	16
×	MAP1980_003	42
△	MAP1980_008	30
+	MAP1980_010	39
▽	MAP1980_012	56
□	MAP1980_022	44
◁	MAP1980_023	27
○	MAP1980_024	21
▷	MAP1980_025	30

Color	Density Concentrations
	0.00 - 2.00
	2.00 - 4.00
	4.00 - 6.00
	6.00 - 8.00
	8.00 - 10.00
	10.00 - 12.00
	12.00 - 14.00
	14.00 <
<b>Maximum Density</b>	19.23%
<b>Contour Data</b>	Pole Vectors
<b>Contour Distribution</b>	Schmidt
<b>Counting Circle Size</b>	1.0%
<b>Plot Mode</b>	Pole Vectors
<b>Vector Count</b>	304 (34 Entries)
<b>Hemisphere</b>	Lower
<b>Projection</b>	Equal Area

1980 Surface Mapping - Meager Creek, East Arm  
 - Poles represent Peak Orientations  
 - Poles are weighted



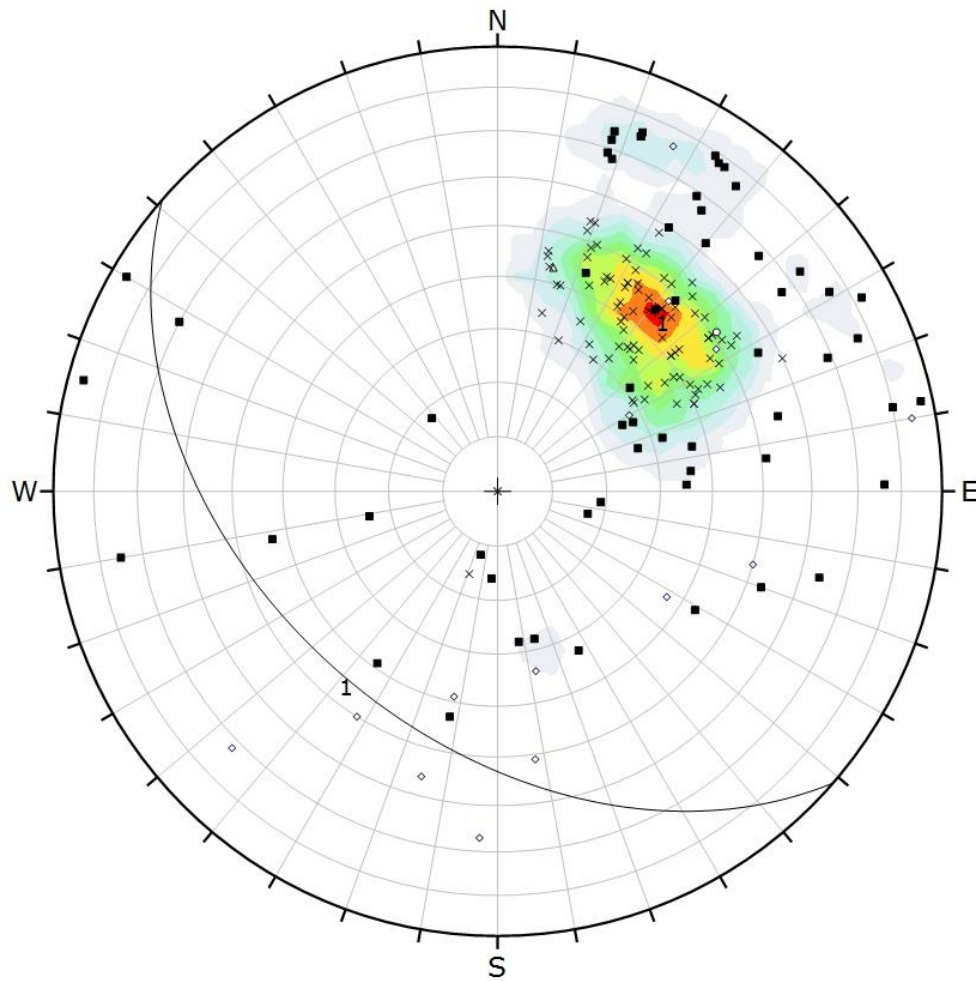
Symbol	STATION	Quantity
◇	MAP1980_001	36
×	MAP1980_013	36
△	MAP1980_014	33
+	MAP1980_015	23
▽	MAP1980_016	31
□	MAP1980_017	17

Color	Density Concentrations
	0.00 - 2.00
	2.00 - 4.00
	4.00 - 6.00
	6.00 - 8.00
	8.00 - 10.00
	10.00 - 12.00
	12.00 - 14.00
	14.00 - 16.00
	16.00 <

<b>Maximum Density</b>	17.86%
<b>Contour Data</b>	Pole Vectors
<b>Contour Distribution</b>	Schmidt
<b>Counting Circle Size</b>	1.0%

<b>Plot Mode</b>	Pole Vectors
<b>Vector Count</b>	175 (27 Entries)
<b>Hemisphere</b>	Lower
<b>Projection</b>	Equal Area

1980 Surface Mapping - West of No Good Creek  
 - Poles represent Peak Orientations  
 - Poles are weighted



Symbol	LITH	Quantity
◇	GN	14
×	GRN	85
△	HNFS	1
■	QZDI	58
○	RYDA	1

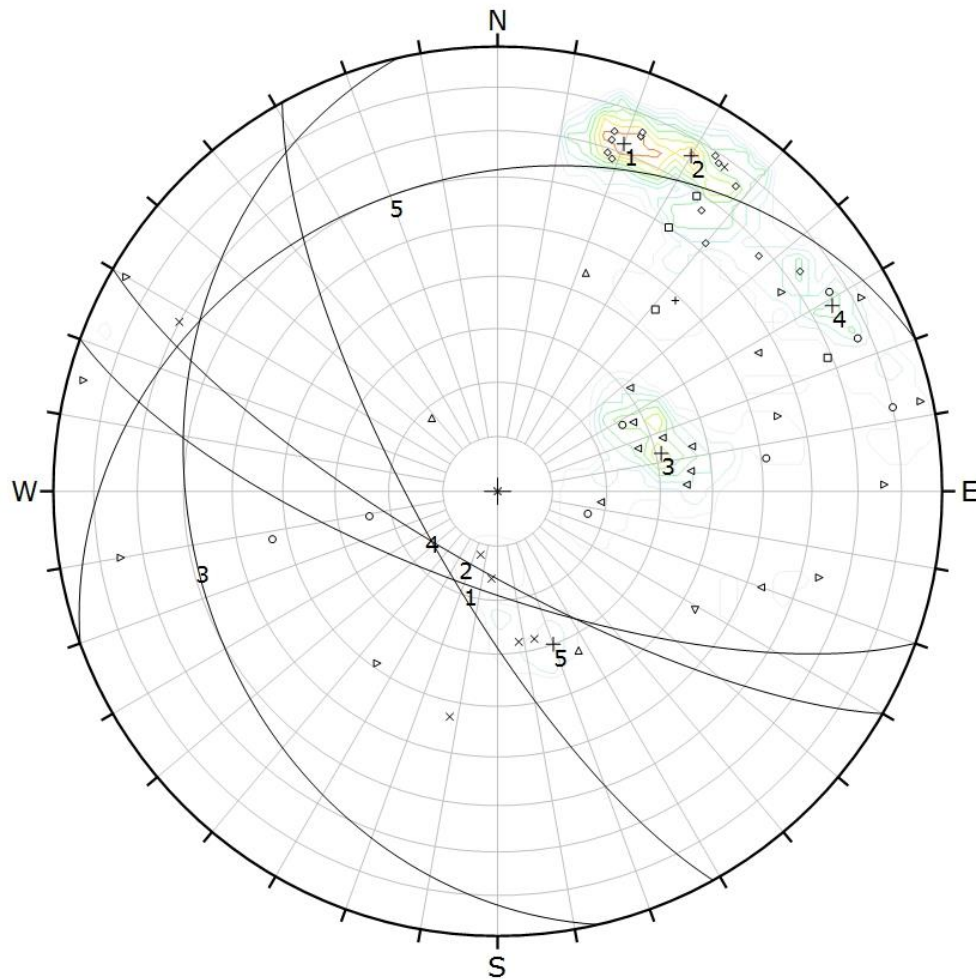
Color	Density Concentrations
	0.00 - 2.00
	2.00 - 4.00
	4.00 - 6.00
	6.00 - 8.00
	8.00 - 10.00
	10.00 - 12.00
	12.00 - 14.00
	14.00 - 16.00
	16.00 - 18.00
	18.00 - 20.00

<b>Maximum Density</b>	19.50%
<b>Contour Data</b>	Pole Vectors
<b>Contour Distribution</b>	Schmidt
<b>Counting Circle Size</b>	1.0%

	Color	Dip	Dip Direction	Label
<b>User Planes</b>				
1	■	45	221	

<b>Plot Mode</b>	Pole Vectors
<b>Vector Count</b>	159 (159 Entries)
<b>Hemisphere</b>	Lower
<b>Projection</b>	Equal Area

1981 Surface Mapping Data - South Reservoir Foliation



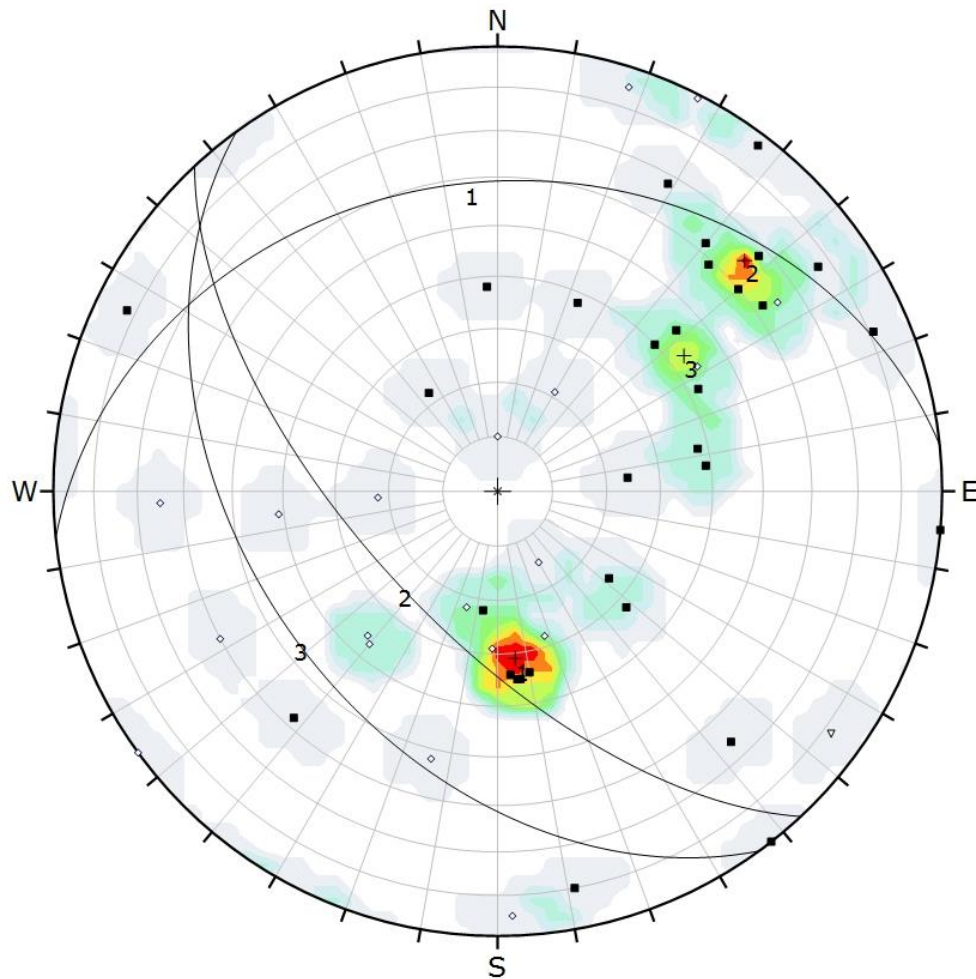
Symbol	STATION	Quantity
◇	MAP1981-043	14
×	MAP1981-044	7
△	MAP1981-045	3
+	MAP1981-046	1
▽	MAP1981-047	1
□	MAP1981-048	4
◁	MAP1981-054	10
○	MAP1981-056	8
▷	MAP1981-057	10

Color	Density Concentrations
	0.00 - 1.30
	1.30 - 2.60
	2.60 - 3.90
	3.90 - 5.20
	5.20 - 6.50
	6.50 - 7.80
	7.80 - 9.10
	9.10 - 10.40
	10.40 - 11.70
	11.70 - 13.00
<b>Maximum Density</b> 12.07%	
<b>Contour Data</b> Pole Vectors	
<b>Contour Distribution</b> Schmidt	
<b>Counting Circle Size</b> 1.0%	

	Color	Dip	Dip Direction	Label
<b>User Planes</b>				
1	█	72	200	
2	█	76	210	
3	█	31	257	
4	█	75	241	
5	█	30	340	

<b>Plot Mode</b>	Pole Vectors
<b>Vector Count</b>	58 (58 Entries)
<b>Hemisphere</b>	Lower
<b>Projection</b>	Equal Area

1981 Surface Mapping Data - South Reservoir  
Quartz Diorite, Foliation



Symbol	LITH	Quantity
◇	GN	19
■	QZDI	31
▽	QZTE	1

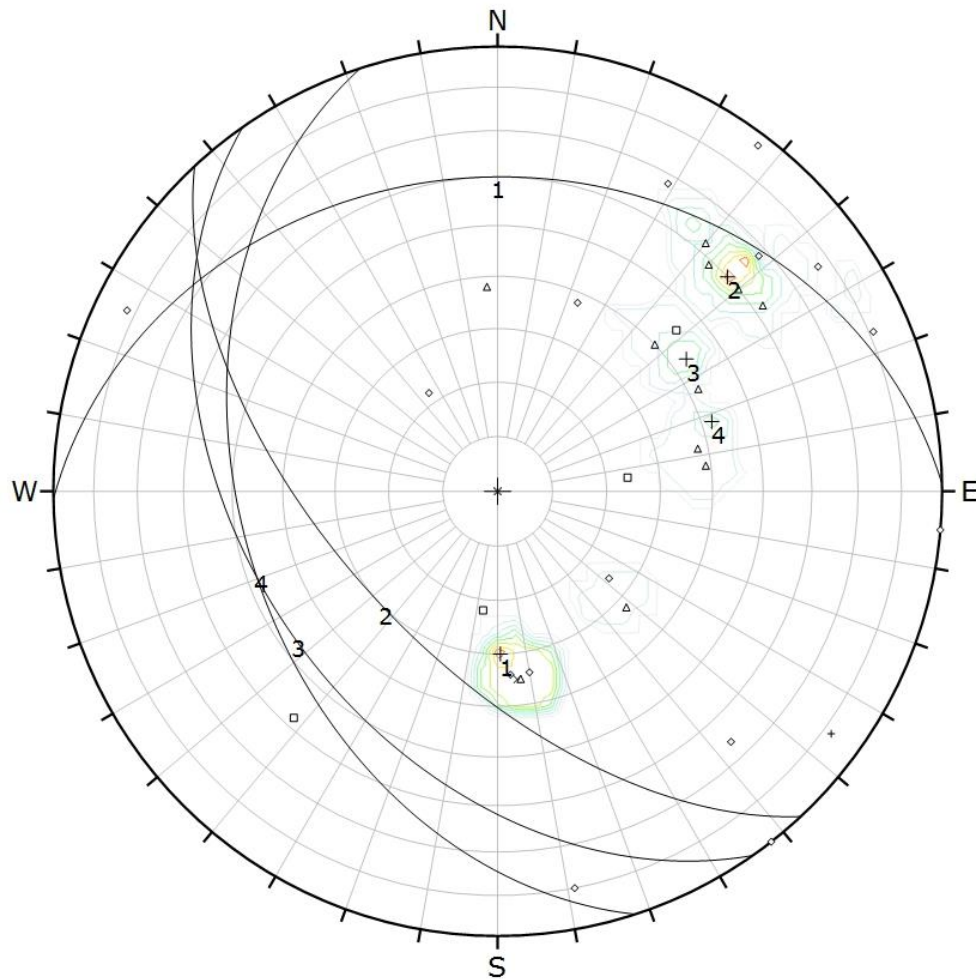
Color	Density Concentrations
	0.00 - 1.20
	1.20 - 2.40
	2.40 - 3.60
	3.60 - 4.80
	4.80 - 6.00
	6.00 - 7.20
	7.20 - 8.40
	8.40 - 9.60
	9.60 - 10.80
	10.80 - 12.00

<b>Maximum Density</b>	11.76%
<b>Contour Data</b>	Pole Vectors
<b>Contour Distribution</b>	Schmidt
<b>Counting Circle Size</b>	1.0%

	Color	Dip	Dip Direction	Label
<b>User Planes</b>				
1	■	31	354	
2	■	65	227	
3	■	43	234	

<b>Plot Mode</b>	Pole Vectors
<b>Vector Count</b>	51 (51 Entries)
<b>Hemisphere</b>	Lower
<b>Projection</b>	Equal Area

1981 Surface Mapping - East of Camp Fault  
All Rock Types, Foliation



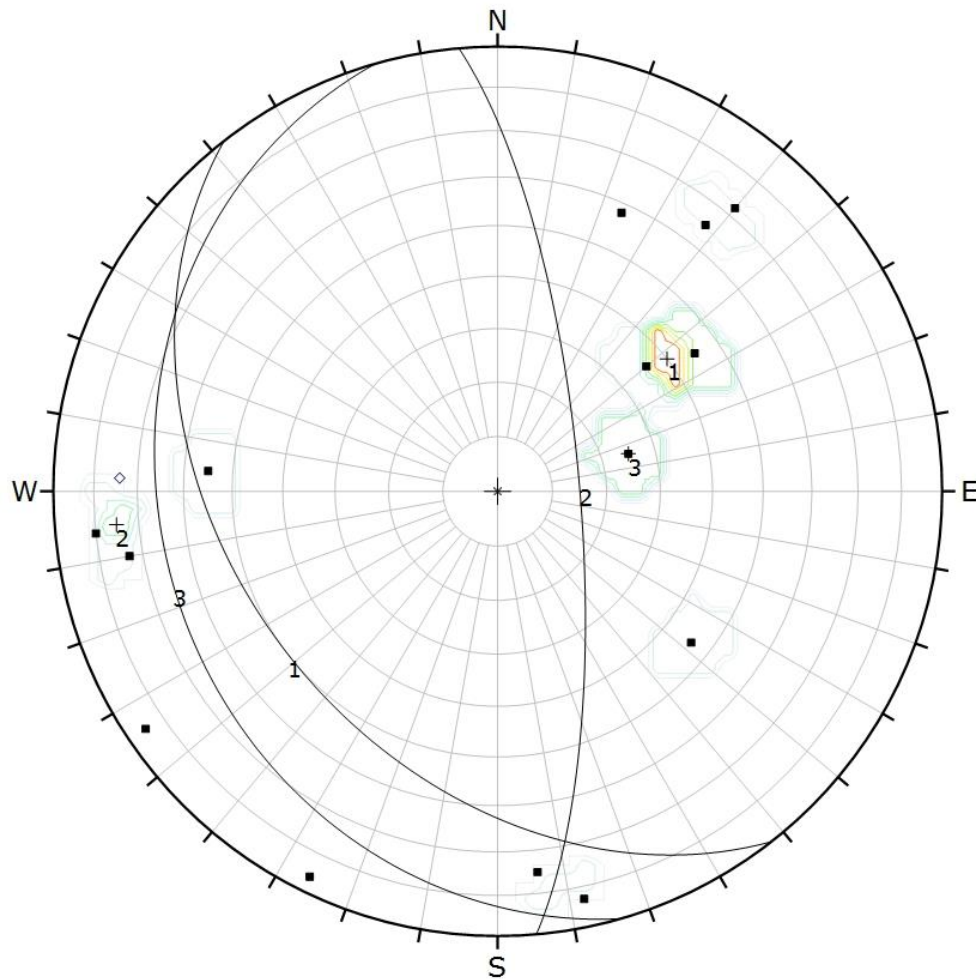
Symbol	STATION	Quantity
◇	MAP1981-058	15
×	MAP1981-060	1
△	MAP1981-061	11
+	MAP1981-062	1
□	MAP1981-063	4

Color	Density Concentrations
	0.00 - 1.60
	1.60 - 3.20
	3.20 - 4.80
	4.80 - 6.40
	6.40 - 8.00
	8.00 - 9.60
	9.60 - 11.20
	11.20 - 12.80
	12.80 - 14.40
	14.40 - 16.00
<b>Maximum Density</b> 15.63%	
<b>Contour Data</b> Pole Vectors	
<b>Contour Distribution</b> Schmidt	
<b>Counting Circle Size</b> 1.0%	

	Color	Dip	Dip Direction	Label
<b>User Planes</b>				
1	█	30	359	
2	█	60	227	
3	█	43	235	
4	█	42	252	

<b>Plot Mode</b>	Pole Vectors
<b>Vector Count</b>	32 (32 Entries)
<b>Hemisphere</b>	Lower
<b>Projection</b>	Equal Area

1981 Surface Mapping - East of Camp Fault  
Quartz Diorite, Foliation



Symbol	STR	Quantity
◇	FL	1
■	JN	21

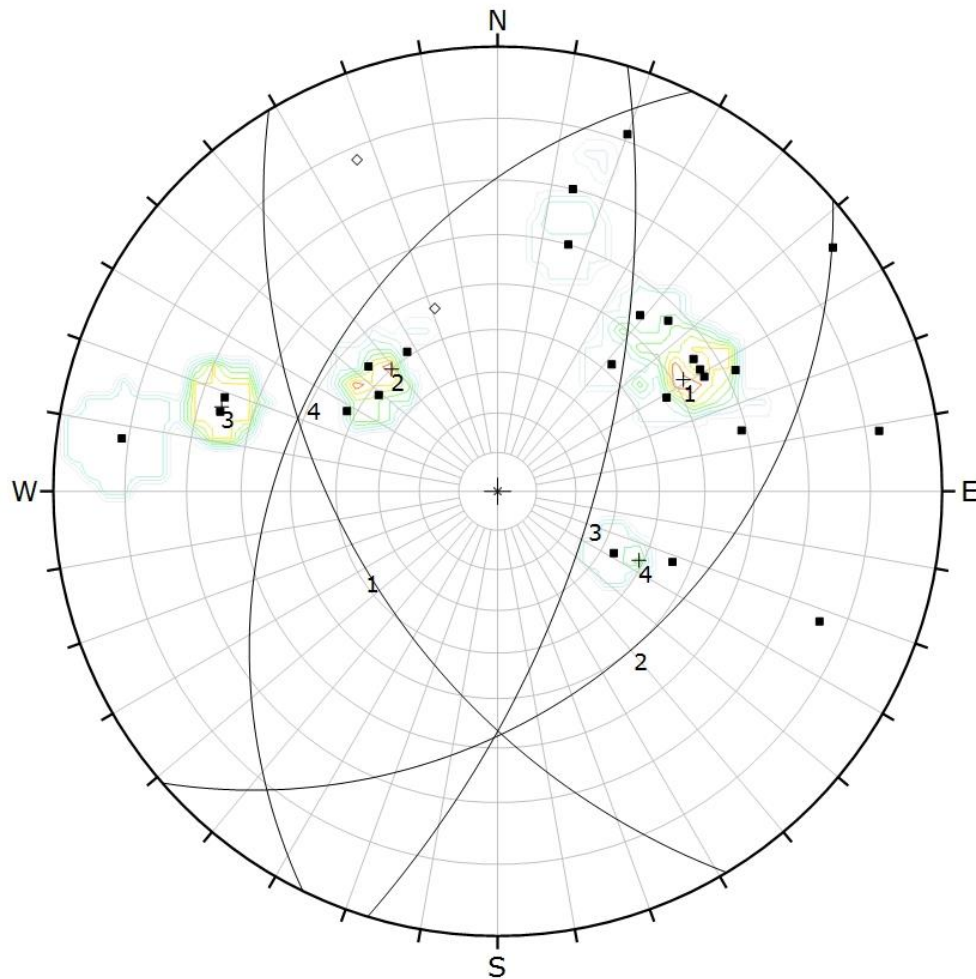
Color	Density Concentrations
	0.00 - 2.30
	2.30 - 4.60
	4.60 - 6.90
	6.90 - 9.20
	9.20 - 11.50
	11.50 - 13.80
	13.80 - 16.10
	16.10 - 18.40
	18.40 - 20.70
	20.70 - 23.00

<b>Maximum Density</b>	22.73%
<b>Contour Data</b>	Pole Vectors
<b>Contour Distribution</b>	Schmidt
<b>Counting Circle Size</b>	1.0%

	Color	Dip	Dip Direction	Label
<b>User Planes</b>				
1	■	40	232	
2	■	75	85	
3	■	25	254	

<b>Plot Mode</b>	Pole Vectors
<b>Vector Count</b>	22 (15 Entries)
<b>Hemisphere</b>	Lower
<b>Projection</b>	Equal Area

2013 Surface Mapping Data, All Structures  
 - North Reservoir, Quartz Diorite  
 - Mapping Station 1  
 - Maximum # structures per pole = 3



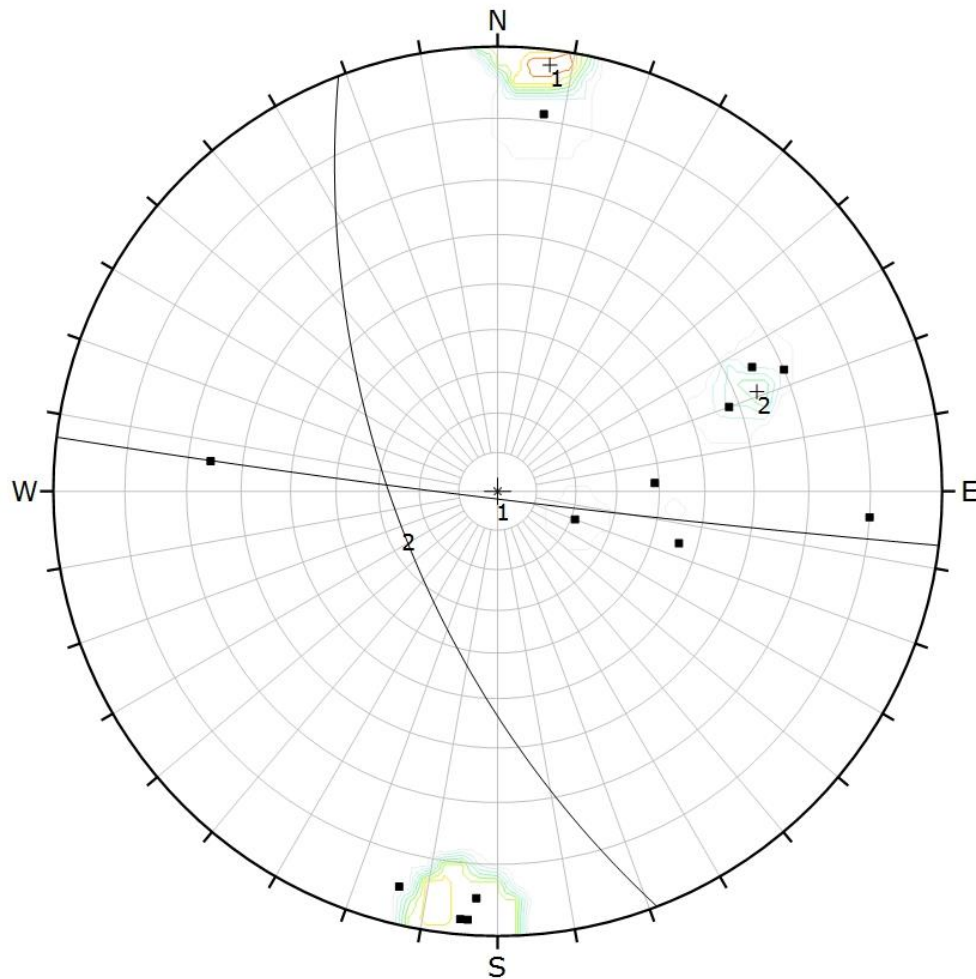
Symbol	STR	Quantity
◇	FL	2
■	JN	39

Color	Density Concentrations
	0.00 - 1.50
	1.50 - 3.00
	3.00 - 4.50
	4.50 - 6.00
	6.00 - 7.50
	7.50 - 9.00
	9.00 - 10.50
	10.50 - 12.00
	12.00 - 13.50
	13.50 - 15.00
<b>Maximum Density</b> 14.63%	
<b>Contour Data</b> Pole Vectors	
<b>Contour Distribution</b> Schmidt	
<b>Counting Circle Size</b> 1.0%	

	Color	Dip	Dip Direction	Label
<b>User Planes</b>				
1	■	52	239	
2	■	40	139	
3	■	66	107	
4	■	39	296	

<b>Plot Mode</b>	Pole Vectors
<b>Vector Count</b>	41 (26 Entries)
<b>Hemisphere</b>	Lower
<b>Projection</b>	Equal Angle

2013 Surface Mapping Data, All Structures  
 - North Reservoir, Quartz Diorite  
 - Mapping Station 3  
 - Maximum # structures per pole = 3



Symbol	STR	Quantity
■	JN	18

Color	Density Concentrations
	0.00 - 3.90
	3.90 - 7.80
	7.80 - 11.70
	11.70 - 15.60
	15.60 - 19.50
	19.50 - 23.40
	23.40 - 27.30
	27.30 - 31.20
	31.20 - 35.10
	35.10 - 39.00

Maximum Density	38.89%
Contour Data	Pole Vectors
Contour Distribution	Schmidt
Counting Circle Size	1.0%

	Color	Dip	Dip Direction	Label
User Planes				
1	■	88	187	
2	■	64	249	

Plot Mode	Pole Vectors
Vector Count	18 (13 Entries)
Hemisphere	Lower
Projection	Equal Angle

2013 Surface Mapping Data, All Structures  
 - North Reservoir, Quartz Diorite  
 - Mapping Station 4  
 - Maximum # structures per pole = 3

## **Appendix D: Coordinates of Mapping Stations**

### D.1 Mapping station coordinates, 1980 surface mapping campaign

STATION	NORTHING (m)	EASTING (m)	ELEVATION (m)	AREA	ROCK TYPE	NUMBER OF FRACTURES
1	5 603 069	461 001	1100	West of No Good Creek	QZDI	190
2	5 602 069	466 201	760	Meager Creek East Arm	QZDI	133
3	5 602 519	466 601	760	Meager Creek East Arm	QZDI	200
4	5 602 119	463 701	850	South Reservoir	QZDI	99
5	5 602 594	464 301	940	South Reservoir	QZDI	100
6	5 602 219	462 901	1000	South Reservoir	QZDI	199
7	5 602 219	462 501	1000	South Reservoir	QZDI	199
8	5 602 419	467 951	740	Meager Creek East Arm	QZDI	250
9	5 601 219	463 876	700	South Reservoir	QZDI	348
10	5 604 819	468 501	700	Meager Creek East Arm	QZDI	216
11	5 602 544	463 901	990	South Reservoir	QZDI	200
12	5 605 319	467 701	1220	Meager Creek East Arm	AND	201
13	5 603 319	461 876	1600	West of No Good Creek	QZDI	170
14	5 603 719	461 251	1300	West of No Good Creek	QZDI	149
15	5 601 069	461 651	780	West of No Good Creek	QZDI	103
16	5 601 069	461 026	760	West of No Good Creek	QZDI	101
17	5 601 069	461 451	750	West of No Good Creek	QZDI	100
18	5 601 069	462 651	740	South Reservoir	QZDI	118
19	5 601 069	464 526	690	East of Camp Fault	QZDI	107
20	5 600 969	464 751	680	East of Camp Fault	QZDI	102
21	5 602 119	462 631	930	South Reservoir	QZDI	151
22	5 601 444	467 751	900	Meager Creek East Arm	QZDI	200
23	5 601 469	466 501	640	Meager Creek East Arm	QZDI	149
24	5 602 669	465 576	1050	Meager Creek East Arm	QZDI	100
25	5 604 894	466 926	1390	Meager Creek East Arm	QZDI	148

Modified from (Jamieson 1981)

## D.2 Mapping station coordinates, 1981 surface mapping campaign

STATION	NORTHING (m)	EASTING (m)	ELEVATION (m)	AREA	ROCK TYPE	NUMBER OF FRACTURES
1	5 599 775	465 249	830	South Fork	QZDI	36
2	5 599 705	465 249	830	South Fork	QZDI	28
3	5 598 786	466 377	975	South Fork	AM/QZDI	11
4	5 598 778	466 426	990	South Fork	QZDI	20
5	5 598 766	466 628	1070	South Fork	QZDI	18
6	5 598 731	466 652	1100	South Fork	QZDI	23
7	5 598 706	466 652	1120	South Fork	QZDI	13
8	5 598 669	466 683	1145	South Fork	AM/QZDI	20
9	5 598 769	466 634	1070	South Fork	AM/QZDI	23
10	5 598 471	466 501	1030	South Fork	QZDI	15
11	5 598 486	466 631	1080	South Fork	QZDI	18
12	5 598 450	466 692	1110	South Fork	QZDI	14
13	5 598 441	466 729	1130	South Fork	QZDI	5
14	5 598 469	467 011	1290	South Fork	AM/QZDI	30
15	5 598 484	466 646	1090	South Fork	QZDI	6
16	5 612 329	465 401	1035	Fall Creek	QM	48
17	5 612 329	465 391	1035	Fall Creek	QM	21
18	5 612 329	465 391	1080	Fall Creek	AND	14
19	5 612 274	465 391	1080	Fall Creek	AND	2
20	5 612 271	465 389	1090	Fall Creek	QM	39
21	5 611 884	464 826	1470	Fall Creek	RYDA	36
22	5 611 659	464 461	1630	Fall Creek	RYDA	2
23	5 611 719	464 401	1525	Fall Creek	RYDA	19
24	5 611 879	464 501	1480	Fall Creek	RYDA	35
25	5 611 899	464 521	1460	Fall Creek	RYDA	4
26	5 611 884	464 501	1470	Fall Creek	RYDA	28
27	5 612 164	464 439	1430	Fall Creek	RYDA	64
28	5 612 019	463 731	1705	Fall Creek	RYDA	58
29	5 612 284	464 251	1480	Fall Creek	RYDA	31
30	5 612 459	464 401	1440	Fall Creek	RYDA	4
31	5 612 479	464 358	1430	Fall Creek	RYDA	12
32	5 612 019	465 251	1205	Fall Creek	QM	41
33	5 612 004	465 241	1215	Fall Creek	RYDA	5
34	5 611 954	465 181	1225	Fall Creek	HNFS	31

## D.2 Mapping station coordinates, 1981 surface mapping campaign continued

STATION	NORTHING (m)	EASTING (m)	ELEVATION (m)	AREA	ROCK TYPE	NUMBER OF FRACTURES
35	5 613 929	464 608	1010	Fall Creek	RYDA	32
36	5 613 419	459 775	930	Affliction Creek	RYDA/AM	35
37	5 613 249	459 726	970	Affliction Creek	HNFS/AM	11
38	5 613 099	459 726	1015	Affliction Creek	QZTE/AND	41
39	5 613 419	459 776	940	Affliction Creek	AM/RYDA	37
40	5 613 234	459 706	995	Affliction Creek	HNFS	2
41	5 602 289	463 601	965	Above M-4	QZDI	14
42	5 602 739	463 916	995	Above M-4	QZDI	7
43	5 602 349	463 971	910	Above M-4	QZDI	3
44	5 602 654	464 296	930	Above M-6	QZDI/HNFS	2
45	5 602 704	464 271	930	Above M-6	QZDI	1
46	5 602 734	464 296	930	Above M-6	QZDI	4
47	5 602 524	464 371	935	Above M-6	GRN	3
48	5 602 549	464 351	960	Above M-6	GRN	9
49	5 602 599	464 341	965	Above M-6	GRN	19
50	5 602 624	464 331	965	Above M-6	GRN	11
51	5 602 654	464 296	970	Above M-6	GRN	12
52	5 602 719	464 291	970	Above M-6	QZDI	11
53	5 602 654	464 296	1000	Above M-6	GRN/RV	32
54	5 602 289	464 671	900	Above M-6	GN	22
55	5 602 394	464 631	910	Above M-6	DI	10
56	5 602 659	465 051	1060	Above M-6	DI/QZDI	15
57	5 602 419	465 111	990	Above M-6	GN/AND	2
58	5 602 399	465 131	990	Above M-6	QZDI	1
59	5 602 369	465 131	990	Above M-6	QZDI	11
60	5 602 189	465 111	970	Above M-6	GN/QZDI	13
61	5 602 119	465 051	840	Above M-6	QZDI	4
62	5 602 189	465 101	950	Above M-6	GN	6
63	5 607 779	471 531	420	SE Side-Above Camp	GN	55
64	5 607 279	471 126	425	SE Side-Above Camp	HNFS	4
65	5 607 259	470 781	525	SE Side-Above Camp	HNFS	47
66	5 607 739	471 021	570	SE Side-Above Camp	GRN	6
67	5 608 344	470 706	535	SE Side-Above Camp	GRN	43
68	5 607 739	470 801	645	SE Side-Above Camp	GRN	8

## D.2 Mapping station coordinates, 1981 surface mapping campaign continued

STATION	NORTHING (m)	EASTING (m)	ELEVATION (m)	AREA	ROCK TYPE	NUMBER OF FRACTURES
69	5 607 669	470 641	690	SE Side-Above Camp	GRN	44
70	5 608 089	470 541	800	SE Side-Above Camp	GRN	3
71	5 607 879	470 451	815	SE Side-Above Camp	GRN	4
72	5 607 719	470 301	840	SE Side-Above Camp	GRN	26
73	5 607 819	470 651	720	SE Side-Above Camp	GRN	11
74	5 607 619	470 231	735	SE Side-Above Camp	GRN	59
75	5 607 509	471 261	505	SE Side-Above Camp	GRN	2
76	5 607 489	471 321	480	SE Side-Above Camp	GRN	1
77	5 607 719	470 471	715	SE Side-Above Camp	GRN	3
78	5 607 894	470 636	715	SE Side-Above Camp	GRN	1
79	5 606 669	469 706	615	SE Side-Above Camp	QZDI	1
80	5 611 919	458 836	1380	Affliction Creek	QM	48
81	5 612 019	459 046	1300	Affliction Creek	QZDI	48
82	5 612 129	459 151	1240	Affliction Creek	QZDI	2
83	5 612 074	459 401	1260	Affliction Creek	QZDI	3
84	5 612 139	459 471	1250	Affliction Creek	QZDI/GN	3
85	5 613 199	459 901	1020	Affliction Creek	SLT	1
86	5 607 734	469 971	950	SE Side-Above Camp	MARB	34
87	5 608 074	469 936	1040	SE Side-Above Camp	GRN	1
88	5 608 009	469 956	1040	SE Side-Above Camp	GRN	1
89	5 607 929	469 971	1035	SE Side-Above Camp	GRN/MARB	7
90	5 607 849	469 976	1030	SE Side-Above Camp	MARB	1
91	5 607 774	469 956	1015	SE Side-Above Camp	MARB	1
92	5 607 704	469 866	1000	SE Side-Above Camp	MARB/DIO	3

### D.3 Mapping station coordinates, 1980 surface mapping campaign

STATION	NORTHING (m)	EASTING (m)	ELEVATION (m)	AREA	ROCK TYPE	NUMBER OF FRACTURES
1	5 610 514	469 210	458	North Reservoir	QZDI	15
2	5 611 673	468 539	508	North Reservoir	BREC	3
3	5 611 094	469 033	478	North Reservoir	QZDI	26
4	5 611 009	469 058	471	North Reservoir	QZDI	13